



**This electronic thesis or dissertation has been  
downloaded from Explore Bristol Research,  
<http://research-information.bristol.ac.uk>**

*Author:*

**Flores, Felipe A**

*Title:*

**Dynamics and Modelling of the 2015 Calbuco eruption Volcanic Debris Flows (Chile).  
From field evidence to a primary lahar model**

**General rights**

Access to the thesis is subject to the Creative Commons Attribution - NonCommercial-No Derivatives 4.0 International Public License. A copy of this may be found at <https://creativecommons.org/licenses/by-nc-nd/4.0/legalcode>. This license sets out your rights and the restrictions that apply to your access to the thesis so it is important you read this before proceeding.

**Take down policy**

Some pages of this thesis may have been removed for copyright restrictions prior to having it been deposited in Explore Bristol Research. However, if you have discovered material within the thesis that you consider to be unlawful e.g. breaches of copyright (either yours or that of a third party) or any other law, including but not limited to those relating to patent, trademark, confidentiality, data protection, obscenity, defamation, libel, then please contact [collections-metadata@bristol.ac.uk](mailto:collections-metadata@bristol.ac.uk) and include the following information in your message:

- Your contact details
- Bibliographic details for the item, including a URL
- An outline nature of the complaint

Your claim will be investigated and, where appropriate, the item in question will be removed from public view as soon as possible.



Faculty of Science  
School of Earth Science

# Dynamics and Modelling of the 2015 Calbuco eruption Volcanic Debris Flows (Chile)

From field evidence to a primary lahar model

By

Felipe A. Flores Lobos

A dissertation submitted to the University of Bristol in accordance with the requirements for award of the degree of Master of Science by Research in the Faculty of Science, School of Earth Sciences.

July, 2022

Word count: 37966

# Abstract

The Calbuco volcanic eruption of 2015, was characterized by two explosive phases with partial and major column collapses that triggered lahars in many of the channels on the flanks of the volcano. Large lahar flows descended the southern flank where highly fractured ice bodies were emplaced on steep slopes.

In this study, we present a detailed chronology of the volcanic flows based on a multi parameter data set that includes social media, reports of authoritative institutions, instrumental monitoring data and published research literature on the eruption. Our review of these data established that lahars in the Amarillo river began during the first phase of the eruption due to the sustained emplacement of pyroclastic flows in its catchment. In contrast, we propose that the lahars in the Blanco – Correntoso river system and the Este river were likely to have been triggered by a sudden mechanical collapse of the glacier that triggered mixed avalanches which transitioned into lahars as they propagated downstream.

We have conducted post eruption field surveys in Blanco – Correntoso and Este – Amarillo river systems to collect data to characterize the dynamics of the lahars produced during the eruption. These observations include inundation cross-sections, estimates of flow speeds, and characterization of the morphology and componentry of flow facies. Our field data are combined with instrumental records from gauge stations along the channels. The observational dataset shows evidence of transitions in flow rheology and composition, as well as the changing erosional and depositional character of the flow.

Our new field measurements are used together with instrumental data as an observational dataset for calibrating a dynamic, physics-based model of lahar dynamics, Laharflow. We model flows in the Blanco – Correntoso river system, using LaharFlow, and explore the influence of the model parameters on flow predictions in an ensemble of simulations. We develop a calibration process that accounts for the substantial epistemic uncertainties in our observations and the model formulation, that seeks to determine plausible ranges for the model parameters, including those representing the lahar source. Our approach highlights the parameters in the model that have a dominant effect on the ability of the model to match observations, indicating where further development and additional observations could most effectively improve model predictions. The simulations in our ensemble that provide plausible matches to the observations are combined to produce flow inundation maps that encompass the combined uncertainties in our calibration.

## Author's declaration

I declare that the work in this dissertation was carried out in accordance with the requirements of the University's *Regulations and Code of Practice for Research Degree Programmes* and that it has not been submitted for any other academic award. Except where indicated by specific reference in the text, the work is the candidate's own work. Work done in collaboration with, or with the assistance of, others, is indicated as such. Any views expressed in the dissertation are those of the author.

A handwritten signature in black ink, appearing to read 'Felipe Flores Lobos', with a large, stylized flourish on the left side.

SIGNED: Felipe Andrés Flores Lobos

DATE: 23.12.2023.



# Acknowledgment

I would like to thank my family, my friends and colleagues at SERNAGEOMIN, and the University of Bristol for their support during my studies, and specifically to Mark Woodhouse for his valuable supervision during this work. I acknowledge the financial support of the Agencia Nacional de Investigación y Desarrollo (ANID) from Chile, through a postgraduate scholarship.

# Table of Content

1	Introduction.....	1
1.1	The 2015 eruption of Calbuco .....	1
1.2	Overview of lahar dynamics .....	1
1.3	Lahar modelling and calibration .....	3
1.4	Aims and approach.....	4
2	Chronology and dynamics of volcanic flows during the 2015 eruption Calbuco, Southern Andes, Chile. ....	6
2.1	Introduction .....	6
2.2	Geological Background .....	7
2.3	Review of the 2015 eruption.....	10
2.4	Methods.....	11
2.4.1	Multi-source data records of the eruption.....	12
2.4.2	Post eruption field studies .....	14
2.5	Results.....	23
2.5.1	Initial and pre-eruptive conditions of the valley and glacier.....	23
2.5.2	Eruption chronology and characteristics of surface volcanic activity .....	26
2.5.3	Volcanic flows and deposits .....	35
2.6	Discussion .....	61
2.6.1	Methods .....	61
2.6.2	Lahar flow transport, triggering mechanisms and dynamics .....	62
2.6.3	Conceptual model of 2015 volcanic flows .....	63
3	Modelling primary lahars from the 2015 eruption of Calbuco .....	65
3.1	Introduction: Modelling lahars .....	65
3.1.1	Models of lahars .....	65
3.2	Overview of the LaharFlow model.....	67
3.2.1	Shallow-layer model of lahars as sediment concentrated flows .....	67
3.2.2	Novel parameterizations in LaharFlow .....	69
3.2.3	Model parameters.....	72

3.2.4	Source parameterization as hydrograph .....	73
3.3	Model calibration .....	75
3.3.1	Calibration as optimization .....	75
3.3.2	Bayesian framework for calibration .....	76
3.4	Objectives.....	78
3.5	Methods.....	78
3.5.1	Observational data .....	78
3.5.2	Preliminary simulations and parameter screening .....	85
3.5.3	Sampling design .....	85
3.5.4	Parameterization of the source .....	86
3.5.5	Identifying active parameters .....	87
3.5.6	Scoring criteria for parameter selection.....	87
3.5.7	Combined inundation map .....	90
3.6	Results.....	91
3.6.1	Example simulation results.....	91
3.6.2	Identification of active model parameters.....	93
3.6.3	Determination of plausible parameter distributions .....	98
3.6.4	Combined inundation map .....	104
3.7	Discussion .....	107
3.7.1	Calibration Data.....	107
3.7.2	Uncertainties.....	109
3.7.3	Results of simulations.....	111
3.7.4	Model limitations and implementation .....	111
3.7.5	Use the model as a tool for hazard assessment. ....	112
4	Conclusion.....	114
5	References .....	116
6	Supplementary material .....	133
6.1	Grain-Size.....	133

# List of Figures

Figure 1. Location map of Calbuco volcano and volcanic flow deposits of the 2015 eruption. ....	7
Figure 2. Geological map of Calbuco volcano. Modified from Sellés and Moreno (2011).....	8
Figure 3. Field survey sites, sample codes and cross sections locations (details of cross sections in Figure 18 26 and Table 4). ....	15
Figure 4. Illustration of reconstruction of channel cross sections. The bottom panel shows an aerial plan view of the distribution of dGPS points taken in the field. The middle panel is a cross-sectional view of the dGPS points along the transect A-A', plotted in a GIS software. Note that the plot takes an arbitrary coordinate system Z (elevation) – X (A-A' direction). The top panel shows the reconstructed channel cross section including dGPS points, tree mark observations (red line), deposit distribution and an inferred topography under deposits. Nomenclature for points is: fl: flood or lateral facies deposits; dep: main flow deposit; cc: central channel; lav: older lava flow. ....	17
Figure 5. Illustration of volume estimation method. A) Division of deposit in portions between successive cross sections. B) Fan morphology of distal deposit and C) reconstruction of bathymetry under Chapo Lake to estimate deposit cross section area. ....	18
Figure 6. a) Flow marks on the walls of a wooden house in Río Blanco Village (UTM 18G 699432/5412772). Notice the different heights reached by the flow on the internal and external (with grass) walls. There is a sediment cap inside the house with a layer of fines in the top that is left by lahar material that has been removed. b) Parameters used in the super elevation technique (equation 3) for flow speed estimation in a bend of the Rio Este. ....	20
Figure 7. Aerial photographs of Calbuco and the southern valleys taken on 09/03/2015, seven weeks before eruption. A) Rio Blanco basin catchment area from south. B) Rio Este-Amarilla basin catchment area from south. For A) and B), white dashed lines represent basin borders, and black arrow indicate the glacier. C) Rio Blanco valley proximal-medial area. D) Chapo lake depositional fan and its coastline. ....	24
Figure 8. Satellite image of the glaciers of Calbuco, taken on 19 <sup>th</sup> March 2012 (GoogleEarth, 2012). Glaciers 2, 3, 4 and part of glaciers 6 and 7 are in the catchment area of Rio Blanco basin. The southern part of glacier 6 drains towards Rio Este. Glacier 5 and the southeastern sector of glacier 6 are emplaced in the high zone of Río Amarillo. Note there is a high density of crevasses and fractures in glaciers 3 and in the south - southeastern zone of glacier 6. Red lines indicate the boundaries of drainage basins. ....	26
Figure 9. Photographs of the eruption column at different times (as shown in the images) of the first eruptive pulse of the 2015 Calbuco Eruption. Upper pictures have similar scale and show the entire column from vent to neutral buoyancy, while the lower pictures focus on surface process on the volcanic edifice. Dashed white lines on the images indicate the Rio Blanco river basin boundaries. Photographs in the left column (A,D) correspond to the initial stage of vent opening and the transient starting plume. Photographs in the centre column (B,E) show the period for	

which there is a quasi-steady buoyancy-driven plume. Photographs in the right column (C, F) show the late stage of the first pulse. Image A is taken from Puerto Montt, southwest of the vent. Images B and E are taken from Puerto Varas, East of the volcano. Images C and F are taken from Puerto Varas. Image D is taken from Chamiza-Correntoso, south-southwest of the volcano). Credits: @N3urOottica (2015) for image A; @Sernageomin for Image B, @zepellin_lh (2015) for Image D. Images C, E and F credits to Natalia Garrido (SERNAGEOMIN). .....	27
Figure 10. Photographs taken from different directions and at different times during first eruptive pulse. Photographs in the upper row are taken from north giving a view of the vent emplacement. The red arrows in panels A, B, G and H indicate the west wall 14ka collapse amphitheatre. The white arrow on panel B indicates the direction of propagation of the pyroclastic density currents descending to northeast valleys. Photographs in the centre row are taken from east. In panel D we note the partial collapse of the eruption column is indicated by the left white arrow), a secondary vent (dashed white line), and a low-altitude atmospheric intrusion of dilute pyroclastic material (right white line). Panel E shows 'streaks' corresponding to ballistic ejecta falling onto the glacier and low-level light coloured clouds lofting from the glacier (the topographic relief is indicated by white dashed lines). On panel F, white arrows indicate lighter colouring of the margins of the low level plume over the glacier area. Photographs in the lower row are taken from southwest and south. The white arrow on panel G gives the propagation direction of flows descending in Rio Amarillo valley. On panel H, the Rio Blanco basin is demarcated with the white dashed line. Credits: Juan Francisco Veintimilla, 2015 (Image A); Paislobo Prensa, 2015 (Image B), Francisco Molina 2018 (Image C); Natalia Garrido (SERNAGEOMIN, Images D, E and F). Guioteca.com (2015) for Image G AFP PHOTO/STR.....	31
Figure 11.A) Image from first pulse of the eruption taken from southeast of the vent. Note the clouds rising above the Río Este valley and a "clean" Río Blanco basin (image from biobiochile.cl, 2015). B) Image of the southern area of the crater. The crater rim is demarcated by the dashed white line and the heads of the Rio Pescado and Rio Blanco basins are indicated (extracted from CHV Noticias 2015).....	32
Figure 12. Discharge at Rio Blanco ante Río Chamiza gauge station. Note the dramatic rise in discharge at 23:00 (22-04-2022) measurement (data from DGA). .....	32
Figure 13..Time series of hydrostatic water level at Chapo lake. Notice the dramatic, 6 cm rise at 05:00-06:00. ....	34
Figure 14. Emplacement map of pyroclastic density currents. ....	35
Figure 15. Photographs taken on 25 <sup>th</sup> April, 2015. A) Crater and tephra deposit view. Red arrows indicate concentric depressions and pipes likely formed by melting of buried glacial ice and degassing of the water vapour. B) Glacier disturbance on the southern flank. There is a complete collapse of an ice block (white arrow). The estimate of ice thickness is 35m and the tephra deposit thickness is 25m. ....	36
Figure 16. A) Proximal pyroclastic density current deposit in Rio Blanco and Rio Sur - Pescado rivers. At the end of the first pulse (Figure 10E and 10F) there was no ash deposited on the upper catchments of the Rio Blanco and Rio Sur - Pescado rivers. Therefore, we propose that the	

majority of this dark tephra is derived from the pyroclastic density current deposit emplaced during the 2nd pulse. B) Proximal deposit in NE flank. C) and D) Unconfined flow from north and northwest. Note the burnt forest (white arrow in D). E) and F) show dense pyroclastic density currents in Rio Blanco Este. ....	40
Figure 17. A partially charred tree found in the Rio Este valley, ~4.5 km downstream from the vent. Notice that the trunk is not completely burnt, with charring only on one side surface. ....	41
Figure 18. Map of facies of the lahar deposit and its source. Point estimates of discharge and speed (white squares and grey square, respectively) derived from field observation are shown. Discharge is estimated by the velocity-area method, using the differential GPS cross section method described in section 2.4.2 and speed is estimated using the Manning equation. ....	42
Figure 19. Summary of main sedimentary characteristics and grain sizes of the deposit along the lahar flow path in the Rio Este-Amarillo valley. ....	43
Figure 20. The Rio Este-Amarillo river system. A) and B) are views of the proximal area of Rio Amarillo taken in 2012 (pre-eruption) and 2016 (post eruption) respectively. In A) it is possible to distinguish two alluvial fans at the outlet of small streams towards the Amarillo river (white dashed lines). in B) the pyroclastic flow deposit (red dashed line) and an escarpment (white dashed line) in the fluvial and alluvial deposits are marked. We propose that the cut in the pre-eruptive alluvial deposits is due to erosion by lahars and the incorporation of non-volcanic sediment into the flow. C) Hydrology of the East River fluvial system, with the foreground corresponding to the upstream catchment, flowing towards Lago Chapo that is out of the image to the upper left. The two tributaries, Rio Amarillo and Rio Este, converge ~5 km from Lago Chapo, but bifurcate ~ 3km from their outlet. The eastern branch, Rio Sin Nombre, was the active flow channel prior to the eruption in 2015. ....	44
Figure 21. Post-eruption photographs of the confluence zone of the two tributaries of the Este-Amarillo fluvial system. A) Aerial image showing the Rio Este (left valley) and Rio Amarillo (right valley). The photograph is taken looking upstream. The red arrow indicates the mega block shown in panel B. Notice the alignment of blocks with the flow direction in the Rio Este. B) Photograph of a mega block found in the confluence zone ~ 4m size. ....	45
Figure 22. Ternary gravel-sand-mud plot of sample from deposit of 2015 lahar in Calbuco volcano. We distinguish the stream channel for each samples (RB – Rio Blanco; RE – Rio Este; REe – Rio Este distal eastern branch; REw – Rio Este distal western branch). Folk & Ward (1957) ....	48
Figure 23. Photographs at outcrop scale. A) A Proximal facie in Rio Este. Note the dark grey deposit and a columnar basalt block transported by the flow. B) A Proximal facie at Rio Amarillo with a gravel lens and imbricated clast. C) A Proximal facie before the transition to Medial facie. There are two main debris flow deposits, suggesting at least two pulses through the Amarillo valley. D) In the medial zone, 500 m downstream of the image in panel C, there is an abrupt change from two distinctive units (panel C) to a more uniform and chaotic deposit (panel D). This suggests that a large pulse propagated down Rio Este and eroded earlier deposits that had formed from flows in Rio Amarillo. E) A Lateral facie deposit that is sandy and with an immersed block. F) A Distal sand-rich deposit. ....	50

Figure 24. Photographs of deposits in the Rio Este flood plain. A) A Medial facie deposit with lots of blocks on the surface and immersed in a sandy matrix. B) A sandy Distal deposit complete flooded a field .Note the buried fence and the decrease in the proportion of mega blocks on the surface of the deposit. ....	51
Figure 25. Photographs of a Distal water rich deposit facie in the Rio Este. A)Photograph looking along the channel from the source. The flow has eroded through section of older volcanoclastic non-consolidated deposits, with a channel width of 40 m. B) A photograph of a road cut by the flow. The erosion depth is approximately 1.5 m. C) Flow marks left by the 2015 lahar on the older terrace wall. At this point the flow mark is 2.5 m above the bed. ....	52
Figure 26. Map of facies of the lahar deposit in Rio Blanco – Correntoso and its source. Locations at which cross-sections are measured are indicated, along with estimates of the peak discharge and flow speeds at some locations. ....	55
Figure 27. Photographs of the pyroclastic density currents and the lahar transition area. A) Contact of Pyroclastic flow deposit (to the right) and the bed of the Rio Blanco. B) Flow mark in a tree (white arrow) and branches oriented in the direction of flow. Flow mark reach 4 m from bed. C) Front of a clast-supported lobe rich in bombs. D) PDC deposit emplaced over a lava flow. E) Section of pyroclastic and volcanoclastic deposit in the PDC-lahar transition area. ....	56
Figure 28. Summary of main sedimentary characteristics and grain sizes of the deposit along the lahar flowpath in rio Este-Amarillo valley .....	59
Figure 29. Photograph of the different areas of Rio Blanco – Correntoso lahar. White arrows on the photographs illustrate the flow direction. A) View of the PDC front and its transition to a lahar. B) and C) Medial facie diverge in two channels, cutting a forest area. D) Medial – Distal area where the flow loses confinement and floods Rio Blanco village. E) Overflow facie, with a large number of trunks in the flow. F) Fisheries facilities destroyed by the overflow facie of the flow. ....	60
Figure 30. A simplified process diagram illustrating the coupling of physical processes in the LaharFlow model. Red arrows link processes internal to the flow. Blue arrows indicate external forcings acting on the flowing layer. ....	68
Figure 31. Idealized hydrographs for the different types of lahar, giving the volumetric discharge $Q$ as a function of time $t$ . The total volume released, $V_t$ , is the integral of the discharge over time (i.e., the area under the hydrograph), The left-hand panel represents a sudden water release flow, with a rapid increase in the flux to peak discharge $Q_p$ at time $t_p$ , before the flux decreases. The middle panel illustrates a sustained water release, with a gradually increasing but fluctuating discharge, with mean value $Q_m$ . The right-hand panel shows a quasi-steady discharge. $Q_b$ denotes the base discharge that occurs before the lahar initiation, $t_p$ denotes the time of peak discharge, and $t_b$ the time of dilution. ....	75
Figure 32. Flow depth measurements in the Rio Blanco catchment at Calbuco volcano. Colours indicate the estimated flow depth. Numbers label the point measurements. The approximate extent of the image is 14 km x 16 km. ....	80

Figure 33. Deposit thickness measurements in the Rio Blanco catchment at Calbuco volcano. Colours indicate the measured deposit thickness. Numbers label the point measurements. The approximate extent of the image is 14 km × 16 km. ....	81
Figure 34. Locations of cross-section surveys at Calbuco. Numbers label the sample locations. The approximate extent of the image is 14 km × 16 km. ....	82
Figure 35. Approximate inundated area of lahars in the Rio Blanco and Rio Correntoso at Calbuco volcano. The approximate extent of the image is 14 km × 16 km. ....	84
Figure 36. An example of a prediction of the maximum flow depth for a lahar in Rio Blanco and Rio Correntoso produced by LaharFlow. ....	92
Figure 37. An example of a prediction of the elevation change produced by a lahar in Rio Blanco and Rio Correntoso simulated by LaharFlow. ....	93
Figure 38. Correlation coefficients for aggregated and summary model outputs for each model and source parameter. Colour saturation denotes the strength of the correlation, with red and blue shades corresponding to positive and negative correlations respectively. ....	95
Figure 39. Correlation coefficients for punctual flow depth outputs at each observation point for each model and source parameter. Colour saturation denotes the strength of the correlation, with red and blue shades corresponding to positive and negative correlations respectively. Flow depth points are labelled as for the observations, as shown on Figure 32. ....	96
Figure 40. Correlation coefficients for punctual flow depth outputs at each observation point for each model and source parameter. Colour saturation denotes the strength of the correlation, with red and blue shades corresponding to positive and negative correlations respectively. Flow depth points are labelled as for the observations, as shown on Figure 33. ....	97
Figure 41. Scatter plot of the implausibility score for the deposit volume in the full domain as a function of the fluid erosion rate. The shaded band between $\pm 1$ indicate the plausible range of the implausibility score. ....	98
Figure 42. Scatter plots of the implausibility scores for flow depth measurement at location 1 for the peak flux and tail flux parameters. The shaded band between $\pm 1$ indicate the plausible range of the implausibility score. ....	99
Figure 43. Scatter plot of the implausibility score for the flow depth as a function of the Chezy coefficient. The shaded band between $\pm 1$ indicate the plausible range of the implausibility score. ....	100
Figure 44. Distributions of the fluid erosion rate determined from the set of plausible matches to each of the observed quantities. The colour indicates the number of runs in the ensemble that produce a plausible match (and outputs with no plausible matches are excluded). The thickness of line indicates percentiles of the distribution, (with 1%, 5%, 10%, 25%, 75%, 90%, 95%, 99% taken, in addition to the minimum and maximum) and the cross indicates the median of the distribution. ....	101
Figure 45. Distributions of the granular erosion rate determined from the set of plausible matches to each of the observed quantities. The colour indicates the number of runs in the ensemble that produce a plausible match (and outputs with no plausible matches are excluded). The thickness	



of line indicates percentiles of the distribution, (with 1%, 5%, 10%, 25%, 75%, 90%, 95%, 99% taken, in addition to the minimum and maximum) and the cross indicates the median of the distribution. ....	102
Figure 46. Distributions of the Chezy coefficient determined from the set of plausible matches to each of the observed quantities. The colour indicates the number of runs in the ensemble that produce a plausible match (and outputs with no plausible matches are excluded). The thickness of line indicates percentiles of the distribution, (with 1%, 5%, 10%, 25%, 75%, 90%, 95%, 99% taken, in addition to the minimum and maximum) and the cross indicates the median of the distribution. ....	103
Figure 47. Distributions of the peak flux determined from the set of plausible matches to each of the observed quantities. The colour indicates the number of runs in the ensemble that produce a plausible match (and outputs with no plausible matches are excluded). The thickness of line indicates percentiles of the distribution, (with 1%, 5%, 10%, 25%, 75%, 90%, 95%, 99% taken, in addition to the minimum and maximum) and the cross indicates the median of the distribution. ....	104
Figure 48. Combined inundation map from the 26 simulations that have the most plausible matches across all observations. The inundation is taken to be flow depths exceeding 10 cm. Colours represent the number of simulations that produce inundation at each location. ....	105
Figure 49. Combined inundation map from the 20 simulations that produce plausible matches to the total deposit volume. The inundation is taken to be flow depths exceeding 10 cm. Colours represent the number of simulations that produce inundation at each location.....	106

# List of Tables

Table 1. Summary of main characteristics of Calbuco historical eruptions (1893—2015). .....	9
Table 2. Hydrological values for glaciers in the southern drainage basins of Calbuco volcano. The areas, mean slopes and median elevations ( $H_{\text{median}}$ ) of the glaciers are estimated from Google Earth aerial imagery and ALOS Palsar DEM. The mean depth of the glacier is obtained from the Chilean National Glacier Inventory (DGA, 2015). The glacier volumes are estimated as the product of the area and mean depth, and the liquid water equivalent volume is calculated assuming an ice density of 900 kg/m <sup>3</sup> (Huss, 2013). See Figure 8 for a map of locations of the glaciers. ....	25
Table 3 Summary of pyroclastic density currents during the Calbuco 2015 eruption. The runout distance is the estimated as the maximum extent of the deposit from the vent. We note whether the flows transitioned into primary lahars, and whether the pyroclastic deposits have a lobate morphology. High: indicating a deposit with abundant lobes, easy to recognise. Medium: refers to a deposit with low lobe concentration, or where the morphology is partially developed. Low: where a subtle lobe development is recognisable. None: where no lobule development is recognisable. ....	38
Table 4. Summary of characteristics of lahars in Rio Este – Amarillo and Rio Blanco-Correntoso systems. ....	46
Table 5. Parameters in the LaharFlow model .....	72
Table 6. Grain size table. Columns are the dry weight for different size fraction.....	133
Table 7. Continuation of Table 6 (to the right).....	134

# 1 Introduction

## 1.1 The 2015 eruption of Calbuco

The 2015 eruption of Calbuco began on 22 April with little precursory activity. This eruption was unusual due to the lack of typical signs of unrest prior to its onset, there were only very subtle changes in volcano seismicity, specifically volcano tectonic earthquakes, usually indicative of subsurface magma rise (Valderrama et al. 2016), and no detected increases in deformation, thermal anomalies, or fumaroles (SERNAGEOMIN 2015a). Precursory seismicity only started at the volcano three hours before the eruption, with a seismic swarm of volcano tectonic earthquakes and lower frequency seismicity. The eruption consisted of two sub-Plinian phases, each lasting about 90 minutes, separated by about six hours of quiescence and seismicity. Both phases produced eruption columns reaching 15 – 17 km above the vent, with ash dispersed up to 150 km to the northeast (Van Eaton et al. 2016; Castruccio et al. 2016). Partial column collapse resulted in several pyroclastic density currents of substantial volumes during the second phase (Van Eaton et al. 2016). The emplacement of these pyroclastic flows over the Calbuco glacier generated lahars to the north, northeast and south of the volcano (Castruccio et al. 2016).

The 2015 Calbuco eruption is notable in the recent geological record for the lack of typical unrest signals, the complex interaction of eruption column collapse, pyroclastic flows and lahar generation, and the emplacement of extensive lahar deposits in the valleys around the volcano. The eruption dynamics were relatively well observed and documented scientifically by the Chilean Geological Survey, SERNAGEOMIN, and informally through extensive coverage on social media. These observations, and the accessibility of the volcano for rapid fieldwork immediately after the eruption make it an ideal case study for the interaction of explosive volcanic flows, in particular the dynamics of lahar generation by glacial melting due to pyroclastic flows, and the subsequent flow and emplacement of the lahars. This, in turn, provides a significant opportunity to use the field observations and inferences of flow conditions from this eruption to calibrate dynamic models of lahars, which are becoming more widely used (e.g., O'Brien, 2007; Christen, Kowalski & Bartelt, 2010; Iverson and George, 2014; Woodhouse et al, 2016). These research areas make up the research presented in this thesis.

## 1.2 Overview of lahar dynamics

Lahars are a significant global hazard; in the last four centuries, the number of fatalities caused by lahars is second only to PDCs when the largest volcanic disasters are removed from the dataset (Auker et al., 2013). They constitute a significant threat to life (Dowling & Santi, 2014; Brown et al., 2017), result in major direct and indirect economic costs (Schuster & Highland, 2001), and attrition from repeated small flows detrimentally affects development particularly of the world's poorest (UNISDR, 2015).

Lahars are defined as a water-saturated mass flow originating on the slopes of volcanoes through mixing of water with volcanoclastic debris and other sediments (Thouret et al., 2020), which propagate downstream. Incorporation or releasing of water and sediment during the motion results in an evolution of the solid/liquid ratio in the flow, which influences the dynamics (Vallance and Iverson, 2015). There are numerous sources of sediment that can be incorporated into the flow, such as volcanic ash or debris, glacial deposits, colluvium, river terraces, soil, and other solid materials in the path of the flow. Water sources can include interstitial or hydrothermal water, rapidly melting snow and ice, trapped subglacial water, crater lakes or other water bodies, or rainfall runoff (Vallance and Iverson, 2015).

In terms of their generation, there are two main groups of lahars: primary (or syn-eruptive) and secondary (post-eruptive) lahars. Primary lahars are those triggered by, and simultaneously with, the eruptive activity, when the incandescent volcanic material interacts thermally and mechanically with snow or glaciers that cover the volcano, or with some other water source such as lakes or rivers, generating a sudden release of a volume of water (Vallance and Iverson, 2015). Secondary lahars, on the other hand, originate during periods of volcanic calm, mainly associated with the remobilization of ash and volcanic sediment or other types of sediment, due to heavy rains or the collapse of a water source for non-eruptive reasons (earthquakes, erosion, etc.) (Vallance and Iverson, 2015).

Based on their rheology, several classifications have been proposed for lahars. Pierson & Costa (1987), suggest that the solid concentration of the flows are the primary determinants of their rheological transitions, and therefore provide a convenient classification. According to Pierson & Costa (1987), a hyperconcentrated lahar is a flow with solids concentrations at values above which the flow acquires yield strength and plastic behaviour; a debris flow lahar, on the other hand, has higher solids concentrations, where the yield strength suddenly increases, and the flow acquires liquefaction behaviour. For higher solids concentrations, at which the flow loses pore pressure and liquefaction capacity, the lahar evolves into a granular flow (Pierson & Costa, 1987). Pierson & Costa (1987) do not propose a fixed limit for the solids concentrations that determine these transitions in flow type but rather point out that these thresholds depend on the grain size distribution, velocity, and sediment type.

The classification between hyperconcentrated flow and debris flow has been widely used in the literature (Pierson & Scott, 1985; Hungr & Jakob, 2005; Vallance & Iverson, 2015). Recently Thouret et al. (2020) have proposed that a proportion of the solid phase of at least 60 vol% (>80 wt.%) in a thoroughly mixed mass with water is required for debris flows. According to Thouret et al. (2020), the solid components include mostly gravel, boulders, and sand, with low proportions of silt and clay, which should be below 3 wt.% in non-cohesive debris flows (Scott, 1988; Scott et al., 1995). Additionally, the density of a debris flow varies between 1800 and 2400 kg m<sup>-3</sup>, which is up to twice the density in aqueous mudflows during floods (Pierson, 1980). Hyperconcentrated flows, on the other hand, are flows that transport between 20 and 60 vol% (40 and 80 wt.%) of sediment (Pierson, 2005), with total densities between 1300 and 1800 kg m<sup>-3</sup>.

While these classifications are useful and sometimes lahars clearly develop the characteristics of a debris flow or a hyperconcentrated flow, it is common for lahars to occur in multiple phases, with notable temporal and spatial transitions in a single event (Vallance, 2000). Thouret et al. (2020) note that an individual lahar pulse can be broken down into three successive segments: (1) the "head" or front, where the density is greatest and the maximum flow velocities and depths occur, with facies that tend to occur as debris flow; (2) the "body", which represents the bulk of the lahar and is characterised by pulses driven by variations in sediment concentration due to dilution and/or deposition, usually with hyperconcentrated-type flows and transitions to debris flow or dilute flows; (3) the "tail", which represents the recessive mass of the mud mixture, exhibiting the lowest solids concentration due to dilution (Pierson, 1986).

Despite decades of scientific study (e.g., Manville et al., 2009; Thouret et al., 2020), lahars remain incompletely understood and pose significant challenges to hazard modellers. The multiphase character of the flow, together with strongly coupled dynamics and diverse flow conditions, pose significant scientific problems. For example, grain sizes within a flow span several orders of magnitude, from micron sized grains held as colloids to metre-sized boulders, and even at high concentrations, the interstitial fluid mediates the intergranular contacts through lubrication and pore pressure support of grains. The grain-scale interactions and coupling to fluid phase motions lead to complex dynamics and abrupt transitions in behaviour. These complex motions lead to a defining characteristic of lahars, their ability to erode significant volumes of channel substrates, leading to increases in volume by up to an order of magnitude for the largest documented events (e.g., Pierson et al, 1990).

### 1.3 Lahar modelling and calibration

Mathematical models of lahars form an important component of their hazard assessment, through the prediction of flow routing and dynamics, informing exposure mapping and development of early warning systems. Despite the significant challenges of approximating the complex multiphase interactions within flowing lahar materials into pragmatic tools for prediction of lahar flow in a reasonable computational time, a number of models have been developed and are starting to become more widely used for practical hazard assessment. Models for computing flows that travel significant distances over topography are typically formulated using the shallow layer approximation (Manville, Major & Fagents, 2013), leading to predictions of depth averaged properties of the flow including velocity and solid concentration. Within the shallow layer approximation, different approaches have been taken to formulating the resistance to motion, including non-Newtonian rheologies linked to particle size distributions (O'Brien, 2007), and granular-fluid interactions (Iverson, 2003). The majority of dynamic models for lahars neglect processes of erosion and deposition, even though they exert a significant control on the flow dynamics (Iverson et al., 2011; Doyle et al., 2011; Vallance and Iverson, 2015). Two approaches have been explored to parameterise bulking of lahars, the addition of substrate by pore pressure

(Iverson et al, 2011; Iverson and George, 2014) and mobilisation of substrate by basal drag (Woodhouse et al, 2016). These mechanisms have been implemented in shallow layer formulations as D-CLAW (Iverson and George, 2014) and LaharFlow (Woodhouse et al, 2016). The LaharFlow model is implemented as a webtool, and used for lahar hazard assessment (e.g., Tierz et al, 2017), and predicts topographic changes associated with substrate erosion and sediment deposition (Langham et al, 2021). The LaharFlow model is used in the research presented in this thesis.

All models of natural processes require some form of calibration, to assign values to parameters used in the approximation of those processes to tractable forms. For complex large-scale flows such as lahars, the relevant force balances cannot be reproduced at smaller scales, so experiments cannot be used to provide parameter values for calibration from a controlled environment (Iverson et al, 2011). Instead, field observations need to be used, which, in turn, requires well-observed lahars and deposit measurements made soon after eruptions before any reworking. Consequently, relatively few locations are available for lahar model calibration. Direct observations of lahars have been made at Colima, Mexico (e.g., Vázquez et al. 2014), and instrumental measurements of lahar dynamics have been made along a section of channel at Semeru, Indonesia (Doyle et al, 2010, 2011). Small, seasonal rainfall-triggered lahars are frequent at these locations, but very often larger lahars from large eruptions e.g., Pinatubo or Mt St Helens do not occur as single events, separated in time, making model calibration more challenging. The aim of detailed fieldwork conducted in this thesis (Chapter 2) is to create observations of lahar erosion and deposition, and inferences into lahar dynamics, that can be used for model calibration in the future. Importantly, this includes understanding of the initiation mechanism and constraints on the volume of material the generates lahars.

Model calibration is challenging, and comprehensive methods may require thousands of simulations to be performed. This can prohibit application of models, and therefore pragmatic approaches to calibration are required. It is important that calibration includes a consideration of uncertainty to avoid overfitting (Hawkins, 2004) and consequent poor prediction when models are used in practice. Furthermore, while a pragmatic calibration should focus on assessing outputs of principle importance for hazard assessment (if this is the intended use of the model), the coupling of nonlinear physical processes controlling lahar dynamics means that multi-parameter data sets are critical for successful calibration.

## 1.4 Aims and approach

The 2015 eruption of Calbuco represents an important case study for the generation and propagation of primary lahars. In this study we investigate the initiation of lahars during the eruption using a variety of observations, including contemporaneous photograph collections and new post-eruption field studies of the volcanic deposits. We examine the propagation and

evolution of lahars from their source to distal areas through field analysis and application of a physical model.

Establishing a detailed chronology of the eruption is an essential first step, to determine the mechanisms by which the lahars were triggered. In this study we compile and analyse observations of the eruption from both primary and secondary sources. The primary sources include social media posts, contemporaneous instrumental records and aerial and satellite images. Secondary sources, including reports from authoritative institutions and published, peer-reviewed scientific literature, containing both observations and interpretations complement the primary sources. We analysis of these observations to determine a chronology of the eruption, including the column dynamics and collapse, producing surface flows, and produce a conceptual model of flow initiation.

Through new post-eruption field studies in the Blanco – Correntoso and Este — Amarillo river systems on the southern flank of Calbuco, we have collected new observational data that we use to characterize the dynamics of lahars produced during the eruption. The direct observations are used to make estimates of the volume, maximum discharges, flow speeds, and proportion of solids in the flow.

We utilize the extensive data set gathered from field observations, together with knowledge of the lahar initiation mechanism, to perform a first-phase calibration of the LaharFlow model. Our approach first identifies the active parameters that have dominant control on model predictions, as these are the parameters most easily calibrated. We adopt implausibility measures (Vernon, Goldstein & Bower, 2010) that incorporate epistemic uncertainty in both observations and model formulation, and use these to evaluate model predictions through an ensemble approach. This allows us to constrain ranges for model parameters and to identify the observational data that is more effective in calibration. We illustrate the use of our calibration approach in creating lahar inundation predictions that combine plausible simulation results.

This manuscript is structured as follows. In Chapter 2 we present our collection of observations and our analysis of these to develop an eruption chronology and interpretation of the variation in the physical characteristics of the volcanic flows. We use these interpretations to construct a conceptual model for the initiation and propagation of volcanic flows during the 2015 eruption at Calbuco. In Chapter 3 we present our application of the LaharFlow numerical model and our calibration process that uses our new field observations and understanding of initiation mechanisms for the 2015 lahars. We also present an illustration of the aggregation of our ensemble numerical results to create combined inundation maps that encapsulate elements of uncertainty in the model application. We present our conclusions in Chapter 4.

The overall aim of our study is to develop an understanding of the primary lahars that occurred during the 2015 eruption to inform hazard assessments of future lahars at Calbuco and other volcanoes.

## **2 Chronology and dynamics of volcanic flows during the 2015 eruption Calbuco, Southern Andes, Chile.**

### **2.1 Introduction**

Chile has several high-risk zones for lahars, located mainly in the southern Andes, near Nevados de Chillán, Llaima, Villarrica, Osorno, Calbuco and Chaitén volcanoes (Lara et al. 2011). Lahars are the deadliest volcanic process in historical eruptions in Chile (Brown et al., 2017) and have caused the partial destruction of two towns in the last century: Coñaripe in 1964 and Chaitén in 2008.

The lahars that occurred during the 2015 eruption of Calbuco volcano are the most recent example in Chile of the destructive capacity of these flows. Five years after this event, it is still possible to find fresh deposits, and the evolution of the catchments following the eruption is likely to continue for decades (Pierson and Major, 2014). The eruption dynamics and the principal characteristics of its products have been presented in several studies (Romero et al. 2016, Van Eaton et al. 2016, Castruccio et al. 2016, Morgado et al. 2019, Arzilli et al. 2019, among others) mainly focused on fall deposits, the petrology and geochemistry of tephra, and the eruption dynamics, including triggering mechanisms and eruption column evolution.

Volcanic flows (pyroclastic density currents and lahars) from the 2015 eruption of Calbuco have been less studied (e.g., Castruccio et al. 2016 studied a PDC on NE flank, and Romero et al., 2023, studied pyroclastic flows on the northern flank) but represent an excellent case study of the physical processes and the impacts of these flows. There is an extensive audiovisual record, including photography and video recordings from social media during the eruption. Additionally, there is relatively easy access to the eruption area, a rigorous monitoring system that was operational during the eruption, and there have been several post-eruption geological surveys made by the Red Nacional de Vigilancia Volcánica (National Volcanic Network Monitoring, RNVV), and the Oficina Técnica de Puerto Varas (Puerto Varas Technical Office, OTPV) that are part of the Servicio Nacional de Geología y Minería (Chilean Geological Survey, SERNAGEOMIN), Chile.

Drawing on these diverse sources of information, as well as new field investigations, this work aims to develop a better understanding of physical processes that control these flows and their interactions, from their initiation area where pyroclastic flows interact with ice cover, to the distal deposition and dilution zones that can be up to 20 km from the source.

In particular, we combine existing literature on the eruption, imagery and descriptions from news articles, social media and authoritative sources, and new field work to develop a comprehensive chronology of the 2015 eruption and the lahars that were produced. We present a conceptual model of the PDC dynamics that explains the triggering of lahars in some drainages, and characterize the lahar flow dynamics that occurred during the 2015 Calbuco eruption on the basis



of (i) a geological and physical characterization of volcanic flows and their deposits in the Río Blanco and Río Este rivers (Figure 1) and (ii) the initial hydrological and geomorphological conditions.

This chapter is organized as follows. In §2.2 we present the geological background to Calbuco volcano. A review of the 2015 eruption is given in §2.3. In §2.4 we give an overview of the methods used to compile and analyze our data, and in §2.5 we present our results. We discuss our approach and results in §2.6 and use them to propose a conceptual model of the volcanic flows.

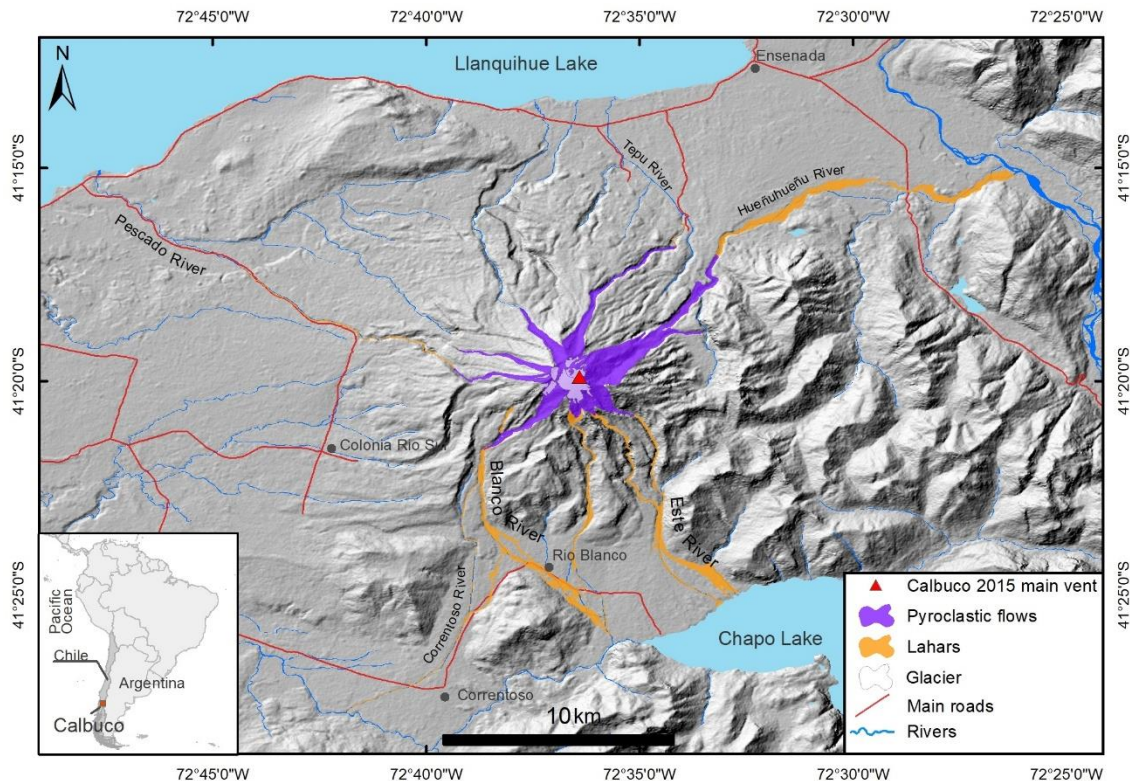


Figure 1. Location map of Calbuco volcano and volcanic flow deposits of the 2015 eruption.

## 2.2 Geological Background

Calbuco volcano is a stratovolcano located in southern Chile ( $-41.3301^{\circ}\text{S}$ ,  $72.609331^{\circ}\text{W}$ ; 2003 m a.s.l.) in the Los Lagos province, 30 km from the city of Puerto Montt (245,902 inhabitants), in the Southern Volcanic Zone of the Andes (López Escobar et al., 1995; Figure 1). Its volcanic edifice is an irregular asymmetric truncated cone with products from basaltic andesitic to dacitic composition (Sellés and Moreno, 2011, Figure 2).

The first ancestral volcano started growth at 300 ka with the emission of andesitic-basaltic lavas and interbedded volcanoclastic breccias (Sellés and Moreno, 2011). The evolution of the volcano includes three glacial – interglacial cycles (Sellés and Moreno, 2011) which have left deep and wide valleys on Calbuco's flanks, with large catchment areas for volcanic flows. The late glacial

cycle ended with a major collapse (ca. 14.5 ka) of a part of the volcanic edifice leaving a broad ~2 km amphitheatre scar to the north (Sellés and Moreno, 2011).

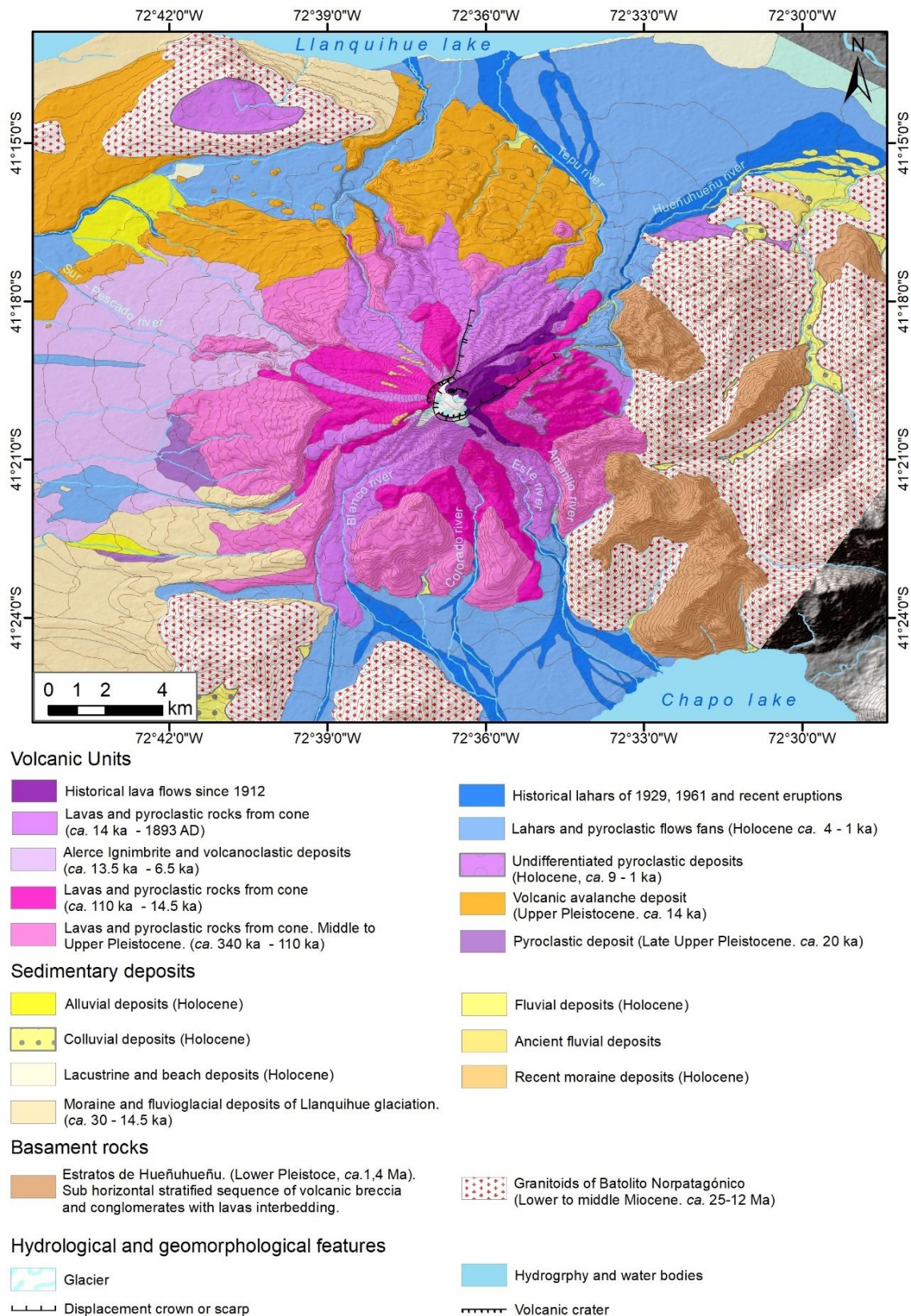


Figure 2. Geological map of Calbuco volcano. Modified from Sellés and Moreno (2011)



During the early Holocene (~12 ka to ~6.5 ka) volcanic activity followed a continuous explosive period that developed an extensive pyroclastic fan to the west and culminated with a notable large explosive event at ca. 6500 y BP known as the Alerce Ignimbrite that covers more than 80 km<sup>2</sup> with basaltic-andesitic products (Sellés and Moreno, 2011, Figure 2).

Eruptive styles in historical times have been dominated by explosive sub-Plinian activity and associated lava effusion and dome building (Sellés and Moreno, 2011), with at least 12 eruptive cycles (Petit Breuili, 1999) during historical times: the major cycle during 1893—1895, two important eruptive events in the 20th century (1929, 1961), and the last one in 2015, after 54 years of inactivity (Table 1). Common hazardous volcanic processes have been pyroclastic density currents, primary and secondary lahars, and regional ash fall.

*Table 1. Summary of main characteristics of Calbuco historical eruptions (1893—2015).*

Year	Main Eruptive style	PDC	Syn-eruptive Lahar	Lava or effusive activity	Column height	Volume [km <sup>3</sup> ]	VEI	Composition % SiO <sub>2</sub>	References
<b>1893-95</b>	Effusive - explosive	Yes	Blanco Norte, Hueñuhueñu and Blanco Sur rivers	Dome	>10 km above vent	0.5	4	58.6%	1, 2, 5, 8, 12
<b>1912</b>	Effusive	Not reported	Not reported	Dome	<i>Data not found</i>	2		<i>No data</i>	5, 12
<b>1917</b>	Explosive - effusive	Not reported	Blanco river (Ensenada)	Andesitic lava flows and dome at Caliente river	<i>Data not found</i>	3		59.3%	5, 8, 12
<b>1929</b>	Explosive-effusive	Yes, North valleys	Blanco Caliente, Sur-Pescado, Este - Amarillo, Blanco Hueñuhueñu rivers	Lava flow to the north	<i>Data not found</i>	4		55.5%	5, 8, 12
<b>1961</b>	Effusive-Explosive	Block and ash associated to lava front in Tepu, Blanco-Hueñuhueñu and Este-Amarillo Rivers	Lahars to Llanquihue and Chapo lakes; Tepu, Blanco-Hueñuhueñu and Este-Amarillo rivers	Andesitic blocky lava flows in Tepu and Amarillo rivers	12 km above vent	0.1	3	54.8-56%	3, 4, 5, 6, 7, 8, 12
<b>2015</b>	Explosive	Column collapses triggered PDCs over all flank of Volcano. Confined PDC on Tepu, Frío, Blanco Hueñuhueñu, Sur, Blanco Sur and Amarillo Valleys	Blanco Caliente, Tepu, Sur-Pescado, Río Este - Amarillo, Chamiza rivers	No effusive activity	> 15 km	0.3	4	54-55%	9, 10, 11, 12

References: 1: Martin (1895); 2: Espinoza (1897); 3: Casertano (1963); 4: Klohn (1963); 5: Petit-Breuilh (1999); 6: Moreno et al. (2006); 7: Castruccio et al. (2010); 8: Sellés and Moreno (2011); 9: Castruccio et al. (2016); 10: Romero et al. (2016); 11: Van Eaton et al. (2016); 12: Romero et al. (2021).

Calbuco has a glacier that covers an area of approximately 1.5 km<sup>2</sup> according to the Dirección General de Aguas (DGA, 2015). The glacier has been disturbed in repeated eruptions, generating lahars of substantial volume such as those which occurred in the 1961 eruption when lahars descended the North, South, and North East flanks of the volcano with estimated velocities of 5–6 m s<sup>-1</sup>, discharge of 3000 m<sup>3</sup> s<sup>-1</sup> and depths up to 12 m in the Rio Colorado Valley (Klohn, 1963), and a subaerial volume of 5 x 10<sup>6</sup> m<sup>3</sup> in Tepu river (Castruccio et al., 2010). The eruption styles and existence of the glacier at Calbuco suggest that lahars will remain an important hazard in future eruptions.

## 2.3 Review of the 2015 eruption

The 2015 eruption of Calbuco began on 22 April with little precursory activity. Despite a subtle change in volcano tectonic earthquakes at Calbuco since February 2015 (Valderrama et al. 2016), the weeks prior to the eruption exhibited a lack of evident signs of unrest such as a dramatic increase in seismicity, deformation, thermal anomalies, or fumaroles (SERNAGEOMIN 2015a; Valderrama et al. 2016). It was not until the same day of the eruption, only ~3 hours before its onset, on 22nd April at 18:11 (all times in UTC) that precursory seismicity started at the volcano with a seismic swarm of more than 140 volcano tectonic (VT) earthquakes in 2 hours (SERNAGEOMIN 2015b), followed by low frequency seismicity (19:15-19:45) and a large hybrid event (Valderrama et al. 2016).

There have been two proposed triggering mechanisms of the eruption, based on interpretation of geophysical and petrological data. Arzilli et al. (2019) suggest volatile overpressure due a crystallization and a second boiling process in a magmatic closed system led to eruption, while Castruccio (2016) and Morgado et al. (2019) suggest an input of small, fresh, and overheated magma at the bottom of the host magma chamber triggered the rapid escalation to eruption. Both mechanisms could account for rapid escalation to eruption with relatively little precursory activity.

The first explosive pulse started on 22nd April, at 21:04 and had a duration of 1.5 hours (SERNAGEOMIN 2015c,d; Van Eaton et al. 2016) with a buoyant plume ascending to ~15 km above the vent, which was dispersed to the N and NE (Sernageomin 2015c; Romero et al. 2016). After a brief period (<3 hours) of “calm” in seismic and surface activity, followed by ~3 hours of precursory seismicity, the second explosive phase started on 23<sup>rd</sup> April at ~04:00 (Van Eaton et al. 2016). The eruption column rose to 17 km above the vent and was dispersed in a similar direction to the first pulse, to the NE (Van Eaton et al. 2016; Castruccio et al. 2016). In comparison with the initial pulse, several pyroclastic density currents of substantial volumes occurred during the second phase, as revealed by (1) the wildfires observed on the flanks of the volcano in the early morning of 3<sup>rd</sup> April during the second eruptive pulse, (2) the PDC units deposited on top of the ash fall layers (Castruccio et al. 2016), as well as (3) indirect observations indicating explosive volcanic activity including lighting and seismicity (Van Eaton et al. 2016; Matoza et al 2018). The emplacement of these pyroclastic flows over the Calbuco glacier generated lahars to the north,

northeast and south of the volcano during the early morning of 23<sup>rd</sup> April (Castruccio et al. 2016) (Figure 1).

After 8 days of fumarolic activity and sporadic low energy explosions (SERNAGEOMIN 2015d), on 30<sup>th</sup> April, at 16:08, a third low-energy pulse occurred with an eruption column of 3—5 km height over the vent which was dispersed to the SE (SERNAGEOMIN 2015e). This pulse was significantly less voluminous and contained less juvenile material compared to the two earlier major sub-Plinian phases (Van Eaton et al., 2016). Over the next weeks and months, a gradual decrease in surface and seismic activity was observed (SERNAGEOMIN 2015f, g, h), and finally, on 18<sup>th</sup> August, SERNAGEOMIN issued a green alert due to the return of volcanic monitoring parameters to the baseline levels (SERNAGEOMIN 2015i).

A total bulk volume for both 22—23 April main explosive eruptive phases (non-DRE) has been estimated in a range from 0.267--0.277 km<sup>3</sup> (Romero et al. 2016) to 0.58 km<sup>3</sup> (Van Eaton et al., 2016), while Castruccio et al. (2016) suggest 0.38 km<sup>3</sup> as the best estimate for total bulk volume. These volume estimates allow us to classify the eruption as a VEI 4 (Newhall and Self 1982). Volcanic products had a basaltic-andesite composition (57-58 SiO<sub>2</sub>; Van Eaton et al. 2016). In contrast with recent historical eruptions, where lava flows or domes have been erupted, such as andesitic blocky lava flow of 1961 (Sellés and Moreno, 2011), the 1893 dome Petit Breuilh (1999) and the other historical lavas listed in Table 1, the 2015 event did not have an effusive phase associated.

While there were fortunately no fatalities reported during the eruption, particularly given the limited warning and initiation of the second pulse at night, the eruption had major impacts on the local area. Notably, these include damage and destruction of houses, fisheries facilities, and bridges by lahars in the Río Blanco-Correntoso Valley, and damage to agricultural land and roof collapse by ash fall in the Ensenada area (Hayes et al. 2019). The vulnerability of local communities exposed to lahars on the southern flank of Calbuco had been recognized and, despite the rapid escalation of activity, a significant number of inhabitants were evacuated.

## 2.4 Methods

To determine the chronology of the 2015 eruption and a physical description of volcanic flows and impacts on the southern valleys of Calbuco, we have compiled data from multiple diverse sources. We use both traditional methods of field observation and characterization of flow deposits, together with modern measurement techniques and data sourced from the national agencies and the public. Here we introduce the data we have collated, and the methods used in processing.

## 2.4.1 Multi-source data records of the eruption

Four different data types were compiled and analysed in order to determine (i) pre-eruptive conditions, (ii) eruption chronology, (iii) volcanic flow dynamics and (iv) post eruption conditions of the volcano and the deposits.

### 2.4.1.1 Video and photographic records from monitoring institutions

Seven sets of photographs and videos taken by the teams of OTPV and the RNVV were compiled. The first set was obtained on 9<sup>th</sup> March 2015, 6 weeks before eruption, during a routine overflight of the region. These data allow us to observe the glacio-hydrological conditions of basins and the geomorphology of valleys prior to eruptions, and thus provides pre-event observations from which we can determine changes attributable to the eruption.

A second collection of photographs were taken from the ground during the eruption from Puerto Varas city (30 km to the east from volcano), in which it is possible to recognize volcanic processes and distinguish different areas impacted by the activity.

Finally, five groups of post eruption photographs from overflight and field studies were analysed to map volcanic deposits, assess morphological changes, and describe their characteristics.

### 2.4.1.2 News and social media (press, authorities, and community sources)

The use of social media and crowdsourced 'citizen science' is emerging as a valuable tool for disaster management and crisis mapping (Ricardi 2016; Bacigalupe et al. 2016; Tavra et al. 2021). There are good examples of freely accessible web tools for the public to report the impact of natural hazards (Ogie et al. 2019) or volcanic processes (Wallace et al. 2015).

In this context, and thanks to the relatively high percentage (~66%) of internet users in Chile in 2015 (SUBTEL 2016), we are able to use a simple, non-automatized method to search for information about the Calbuco eruption in social media and online sources. Using the keywords: "Erupción Calbuco 2015" and "Volcán Calbuco" (in Spanish) it is possible to find a comprehensive chronology of the eruption impacts and responses in the press and online newspapers (e.g., Cooperativa.cl, 2015; Toledo 2015), and several social media records from YouTube (Almonacid 2015; Bravo 2015; CHV Noticias 2015), Twitter posts (Paredes 2015), and Flickr images (León Cabello 2015).

This information was used to trace the progression of the eruption, to locate events in time and space, and identify stages of the evolving volcanic activity, community response and mobilization of responders. However, there is a need to carefully assess and validate these records, to filter-out incorrect or imprecise information (e.g., on location and timing). Therefore, good local knowledge of the volcano is an essential component when using publicly derived data.

Our experience of working at Calbuco volcano provides this local knowledge, allowing us to confidently assess public data. Additionally, we further validate the crowdsourced information using official data sources and cross-compare with other data to produce a coherent eruption chronology. Specifically, we searched official reports of the local and national authorities and civil protection agencies and their 'tweets' made between 22<sup>nd</sup> and 23<sup>rd</sup> April (@Sernageomin, @onemichile, @mop\_chile, @Int\_LosLagos, @Carabdechile).

#### 2.4.1.3 Technical and instrumental data

The RNVV monitoring has been in place at Calbuco volcano since December 2009 providing near-real-time data. At the time of the eruption, the Calbuco monitoring network consisted of two seismic stations in the near field, one true colour camera and one electronic tiltmeter (Valderrama, 2015). The seismic stations were able to detect several signals in the seismicity and analysis of the records allow us to identify the stages and evolution of volcanic activity. In this work, the camera and tiltmeter were not analysed.

Records from "Río Blanco Ante Junta Río Chamiza" and "Lago Chapo" monitoring stations of the Chilean General Water Management (DGA) were analysed to obtain hydrological information and a time-series reconstruction of lahar flow. Specifically, the Río Blanco Ante Junta Río Chamiza station (41° 25' 52" S, 72° 35' 43"W), is a fluvimetric station that measures discharge, and it is located in a distal area of the flow, 10 km from the source and only 500 m upstream from the Río Blanco outlet into Río Chamiza. In addition, Lago Chapo station (41° 26' 2" S, 72° 34' 40 " W) measures meteorological data and the static level of water in the lake in the north area, near to the outlet of the Río Blanco. The data from both stations are freely available on the DGA web database (Información Oficial Hidrometeorológica y de Calidad de Aguas en Línea; <https://snia.mop.gob.cl/BNAConsultas/reportes>, Accessed 21/06/2021).

#### 2.4.1.4 Satellite and aerial image mapping and GIS processing

Freely available images from Google, Esri and Bing Imagery databases provide satellite and aerial imagery both pre- and post-eruption. We analyse the images in order to map glaciers, volcanic deposits, and other identifiable features left by the eruption. The Google Earth images dataset include historical images since 2003. In addition, the 'spatial analysis' and '3d analysis' toolboxes of the Esri ArcMap GIS software package were used to delimit basins and make spatial measurements.

For the hydrological and geomorphology analysis we use the Alos Palsar (<https://earth.esa.int/eogateway/catalog/alos-palsar-products>) Digital Elevation Model (DEM) with a pixel resolution of 12.5 m. The Alos satellite mission was in orbit from May, 2006 to April 2011, and therefore the DEM used here captures the pre-eruptive topography.

## 2.4.2 Post eruption field studies

Two geological fieldtrips to Calbuco volcano were carried out in April 2016 (by the author working at SERNAGEOMIN) and in January 2020 (as part of this study). Two basins (the Blanco--Correntoso rivers and Este-Amarillo rivers system) located on the southern flank of Calbuco and their floodplains were examined (Figure 1 and Figure 3), with a focus on identifying the signatures and deposits of pyroclastic density currents and lahars of the 2015 eruption. In addition, the Río Pescado riverbeds to the north and the Ensenada area, located to the northeast of Calbuco (downwind of the vent at the time of the eruption), were visited to obtain an overview of lahar impacts in the northern valleys in order to compare and contrast with lahars in the southern valleys. Additionally, ashfall from different layers was sampled in order to compare to components in lahar deposits.

The geological survey made during the two fieldtrips included descriptions of a total of 51 outcrops and 29 cross sections (Figure 3). At each location, a qualitative description was composed, and measurements were made of deposits, flow markings and the footprint left by volcanic flows, including flow depth and deposit thickness measurements.

While there are recent examples of unmanned aerial vehicles (UAV) used in field studies of lahars (e.g., Sakamoto & Gomez 2019; Andaru et al, 2021), in our study we used a ground based GNSS system for topographic data collection as it was the unique tool available during post eruption surveys. This also offered advantages in comparison with remote sensing tools and aerial photogrammetry, for example in determining cross sections under forest canopy, and provides complementary data, for example with outcrop scale descriptions of deposit and marks.

### 2.4.2.1 Grain size analysis

Thirty-five bulk samples of lahar and pyroclastic density current deposits were dry sieved in the SERNAGEOMIN laboratory to determine the evolution of the grain size distribution in the deposits, both downstream and laterally. Samples were taken up to very small boulders (128 mm) size, following the scale proposed in Blott & Pye (2012). This fraction is present in most of the facies of the deposits, and therefore is an appropriate range to assess the evolution in transport and deposition phenomena. We avoid sampling coarser sizes due the difficulty in sampling and sieving representative volumes that include sediments > 128 mm. However, we estimate a relative proportion of >128 mm clasts from the deposit and its surface in the field and using photograph and satellite images, to qualitatively distinguish between flow that are rich or poor in boulders and block deposits. Statistics and plots of the sieved samples were made using the Gradistat program (Blott & Pye, 2001).





### 2.4.2.2 Physical Measurement

#### i. Cross-section surveys

The survey of cross sections performed in the Río Blanco and Río Este basins spanned proximal to distal areas. Twenty-three cross-sections were analysed using a high precision GNSS survey with a differential GPS (dGPS), but where there was not satellite signal (e.g., dense forest area) or when equipment was not available, six additional cross sections were measured in the field using a tape measure and a compass. Grain samples were collected at 36 sites for grain-size (Table 6 and 7 in supplementary material), componentry, and textural analysis.

The 23 high-precision cross sections were plotted using topography data taken in 2016 as a part of post eruption surveys performed by SERNAGEOMIN (carried out by the author). Data collected include dGPS points taken in a post-processing kinematic (ppk) mode and processed on Trimble Business Center (TBC) software with <0.5m vertical and horizontal precision for most of the points. Measurement was taken each ~5m in the cross-stream direction to capture the main features (e.g. channels, debris flow deposit, lateral overflow deposit, older bed lithology, tree marks). Profiles were drawn using Esri ArcMap software in a 2D workspace with arbitrary metric coordinate system, allowing the measurement of the deposit and peak-flow cross-sectional area, and describe the valley shape (Figure 4). The bed shape under deposited material was inferred according to lahar terrace architecture, as described by Gomez & Lavigne (2010) and schemes presented by Pierson et al. (2009) and Pierson et al. (2011).

Measurements in a cross-section were made with a horizontal spacing of  $\Delta x = 5$  m. Assuming that the measurement errors for the lateral position and elevation are random and independent, each with standard deviation  $\sigma = 0.1667$  m (i.e.  $3\sigma = 0.5$  m) we can estimate the standard deviation in the cross-section from the quadrature that of the points as

$$\sigma_A^2 = \sum_{k=1}^n (5h_k)^2 \left[ \left( \frac{\sigma}{\Delta x} \right)^2 + \left( \frac{\sigma}{h_k} \right)^2 \right]$$

where  $n$  is the number of measured points and  $h_k$  denotes the height of a measured point. If we approximate  $h_k \approx \bar{h}$  (i.e. each height is approximated by the mean) we obtain

$$\sigma_A = A \sqrt{\left( \frac{\sigma}{\Delta x} \right)^2 + \left( \frac{\sigma}{\bar{h}} \right)^2}$$

so that the relative error in the cross-section area is approximately

$$\frac{\delta A}{A} \approx \frac{3\sigma_A}{A} = \frac{3\sigma}{\Delta x \bar{h}} \sqrt{\bar{h}^2 + \Delta x^2} \quad (1)$$

Taking as an example a mean height of 2.5 m gives a relative error of approximately 22%. Note, the relative error for the cross-section area increases for small depths, so uncertainties in estimates of deposit cross-section area are likely to be larger than uncertainties in the estimates of the area for peak flows.

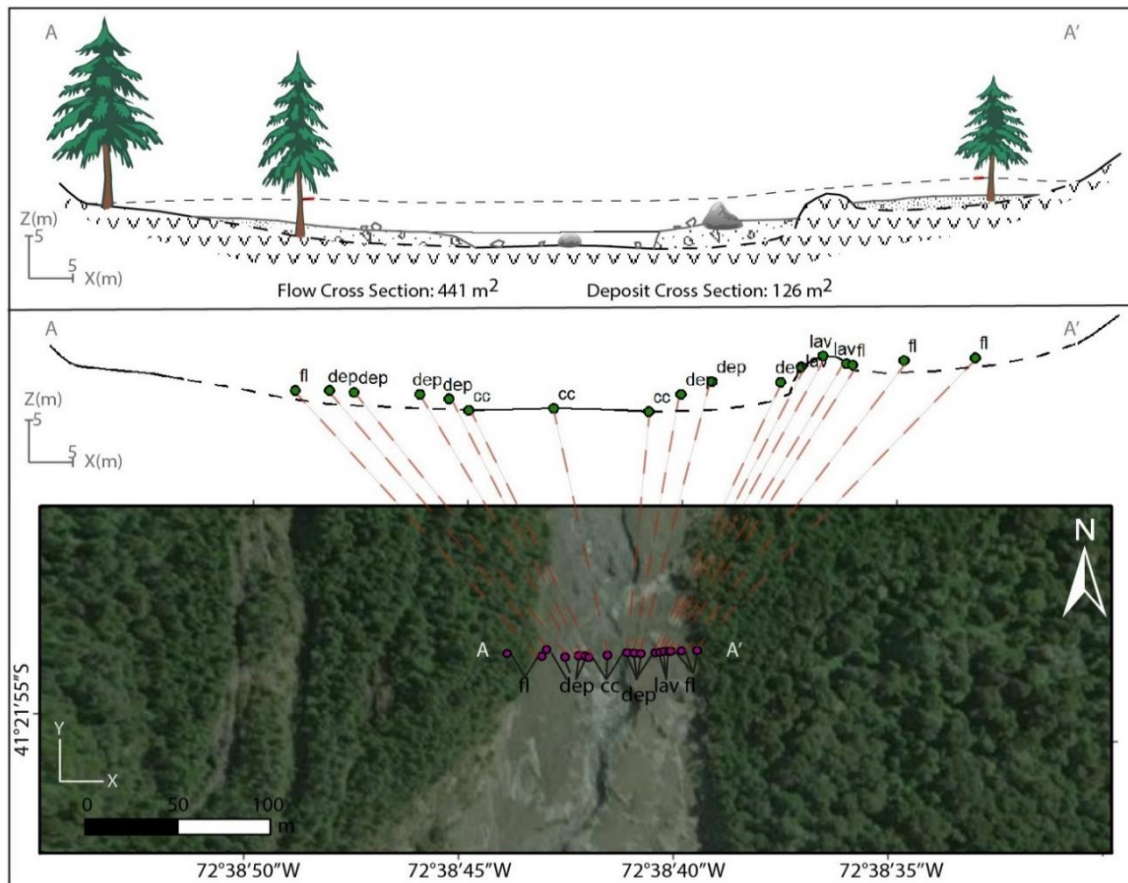


Figure 4. Illustration of reconstruction of channel cross sections. The bottom panel shows an aerial plan view of the distribution of dGPS points taken in the field. The middle panel is a cross-sectional view of the dGPS points along the transect A-A', plotted in a GIS software. Note that the plot takes an arbitrary coordinate system Z (elevation) – X (A-A' direction). The top panel shows the reconstructed channel cross section including dGPS points, tree mark observations (red line), deposit distribution and an inferred topography under deposits. Nomenclature for points is: fl: flood or lateral facies deposits; dep: main flow deposit; cc: central channel; lav: older lava flow.

## ii. Volume of deposits

The deposit of the 2015 eruption has both subaerial and subaqueous facies. The volume of the deposit is estimated by discretization of the entire deposit in a finite number of sections (Figure 5). For simplicity, we assume that the deposit varies continuously between these sections. This assumption will fail in locations where there is no material deposited, and therefore this method could lead to an overestimation of the deposit volume. However, our field observations across the area of the flow downstream from the source suggest that this overestimation is negligible since deposits are observed continuously along the valley. The volume estimated represents a total, absolute volume of deposit, independent of the source and transport of sediment; our calculation does not discriminate between a deposited grain originating from the source area and a grain that has been remobilized from the pre-eruptive channel bed. Additionally, we assume that flows can deposit even in areas where there is net erosion, since the erosive front and peak



stages of lahars are typically followed by a sediment rich tail which actively deposit sediment over the pre-eroded surface (Vallance 2000).

We estimate the subaerial volume of the deposit,  $V$ , as

$$V = \sum_{i=1}^n \left( \frac{A_i + A_{i+1}}{2} \right) L_i \quad (2)$$

where  $A_i$  is a cross section area of discretized section  $i$ , and  $L_i$ , is the length of the flow path between  $A_i$  and  $A_{i+1}$  along the thalweg of the river, considering the channel slope (Figure 5), and  $n$  is the number of sections.

The uncertainty in the deposit volume results from the propagation of uncertainties from cross-section areas (equation (1)) and the length of the channel. Taking  $\sigma_L$  is the uncertainty in the measurement of the length of the thalweg, the uncertainty in the deposit volume is estimate as

$$\sigma_V^2 = \sum_{i=1}^n V_i^2 \left[ \left( \frac{\sigma_A}{A_i} \right)^2 + \left( \frac{\sigma_L}{L_i} \right)^2 \right] \quad (3)$$

where  $V_i = \left( \frac{A_i + A_{i+1}}{2} \right) L_i$  is the estimated volume of the deposit between cross-sections. This uncertainty is likely to be dominated by the uncertainty in the cross-section area, as the length of the thalweg can be estimate using the DEM with a relative error that is smaller than the relative error for the cross-section. Using our typical value above for the uncertainty in the cross-section area gives an approximate relative error in the deposit volume of 22%.

A fraction of the deposit of the lahar in the Río Blanco reached the Chapo lake, forming a subaquatic depositional fan, confined in an estuary-type branch of the lake (Figure 5). This volume was calculated using equation 1, where cross sections are drawn by taking the subaquatic projection of the Alos Palsar DEM.

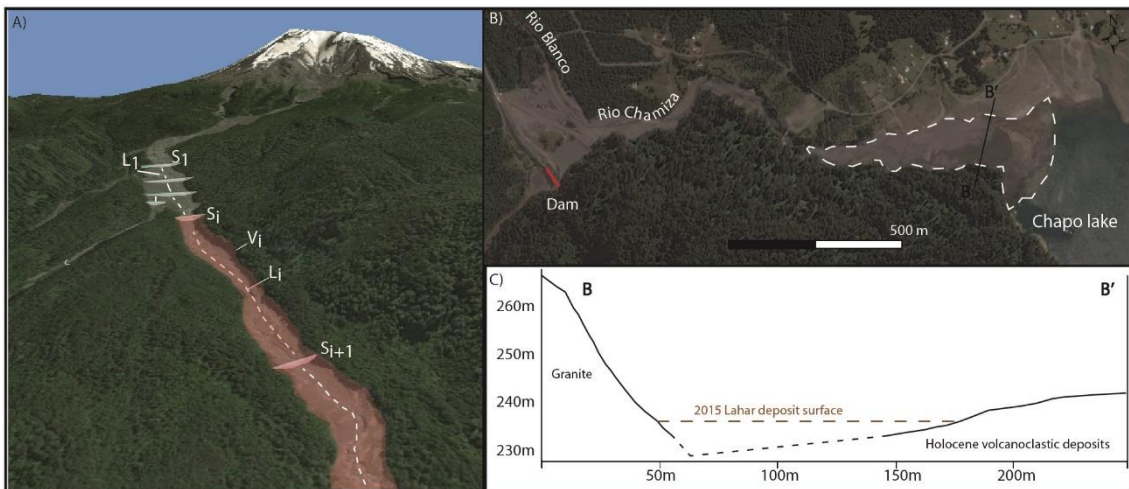


Figure 5. Illustration of volume estimation method. A) Division of deposit in portions between successive cross sections. B) Fan morphology of distal deposit and C) reconstruction of bathymetry under Chapo Lake to estimate deposit cross section area.

### iii. Velocity and discharge estimation

There are several approaches that have been used to compute the velocity of a lahar. The most reliable methods involve the direct measurement during the flow using different types of instruments, including infrasound arrays (e.g., Johnson & Palma, 2015), geophones and gauging stations (e.g., Worni et al., 2012), and video records (e.g., Lavigne et al., 2003). However, direct measurements are not always available and therefore velocities and discharge of lahar flows are often estimated from deposits and flow markings. Methods have been developed using either physical reasoning or empirical relationships and have been widely used for velocity estimation (Prochaska et al. 2008) based on different input data.

Methods based on physical reasoning include energy balances based on a runup height of the flow and measurements of flow superelevation. Flow velocity,  $v$ , can be estimated from the balance of kinetic and potential energy in a control volume (Pierson, 1985),

$$\frac{1}{2} m v^2 = m g h \Rightarrow v = \sqrt{2gh} \quad (4)$$

where  $m$  is the mass of the flow,  $g$  is the acceleration due to gravity ( $9.81 \text{ m s}^{-2}$ ), and  $h$  is the height of the flow. Thus, from runup marks of the flow (Figure 6a) is possible to measure the height,  $h$ , that the flow reached when impinging perpendicularly with an obstacle (e.g., a bridge, a wall, hills, etc.) and thus estimate the velocity,  $v$ . Despite the simplification of open channel hydraulics, this method has been widely used in debris flows (Prochaska et al. 2008).

The measurement uncertainty in the flow velocity estimated using equation (4) is directly related to the uncertainty in the height measurement and is given by

$$\sigma_v^2 = g \sigma_h^2 / 2h,$$

where  $\sigma_h$  is the uncertainty in the height measurement. Typical values ( $h = 1 \text{ m}$  and  $\sigma_h = 1 \text{ cm}$ ) give a relative error in the velocity measurement of 2%. However, this neglects errors that are implicit in the use of equation (4).

The superelevation method has been used to estimate velocities in debris flows and lahars (Pierson 1985; Muñoz-Salinas et al, 2007). It is based on the fluid mechanics of a flow in a curved section of a channel (Chow, 1959), that balance fluid pressure and centrifugal force to give an equation for flow velocity (McClung, 2001),

$$v = (g R_c \cos \delta \tan \beta)^{0.5} \quad (5)$$

where  $R_c$  is the radius of curvature of the channel thalweg, estimated by the method described by Prochaska et al. (2008) from GoogleEarth® images,  $\delta$  is the channel slope in degrees calculated from the Also Palsar DEM, and  $\beta$  is the deposit tilt angle measured in the field using differential GPS (Figure 6b).

The measurement uncertainty in the velocity estimation using equation (5) results from uncertainties in the radius of curvature, channel slope and deposit tilt angle. The measurement error in the deposit tilt angle is likely to be the smallest, as it is made using an accurate differential GPS. The error in the radius of curvature estimate using Google Earth® images is likely to be large. The calculation of the channel slope from the DEM introduces relatively large errors due to the low resolution (12.5 m) of the DEM.

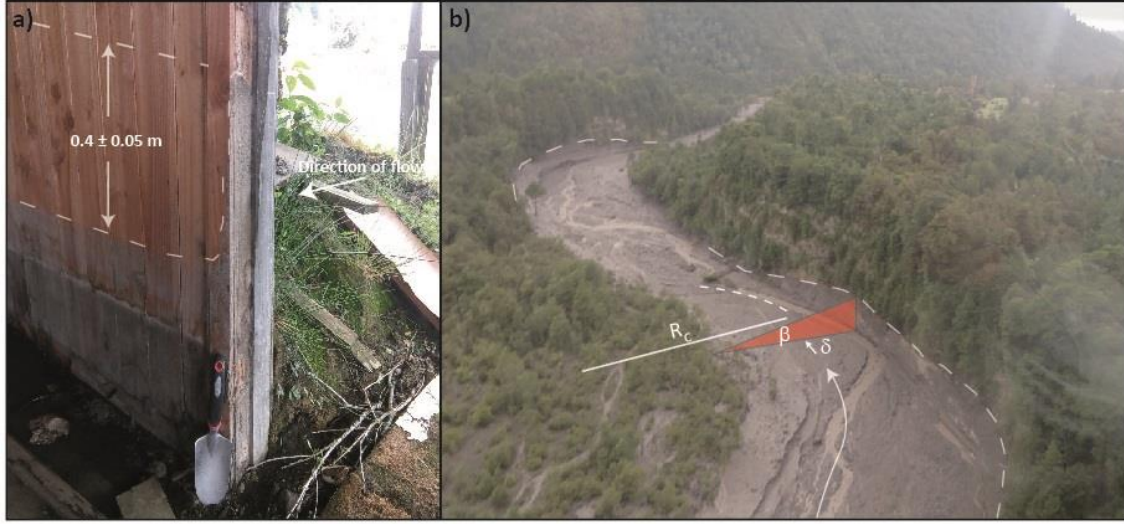


Figure 6. a) Flow marks on the walls of a wooden house in Río Blanco Village (UTM 18G 699432/ 5412772). Notice the different heights reached by the flow on the internal and external (with grass) walls. There is a sediment cap inside the house with a layer of fines in the top that is left by lahar material that has been removed. b) Parameters used in the super elevation technique (equation 3) for flow speed estimation in a bend of the Rio Este.

Comparing these methods, the super elevation technique is often more challenging to apply in practice as it requires more input variables which are not commonly observable in the field. Moreover, variables such as the radius of curvature and the tilt angle are not easy to determine and may not represent the actual maximum of super elevation (Rahman & Konagai, 2016). In addition, in deriving equation (5), some additional assumptions are required: the flow is subcritical, all streamlines of the velocity field are equal to the mean flow velocity and all streamlines have the same radius of curvature (Pierson, 1985). It is not apparent that these conditions are satisfied for natural flows.

A widely-used empirical formula to describe energy loss and velocity of flows in open channel and pipes is the Manning equation (Brater et al., 1996),

$$v = \frac{r^{2/3} s^{1/2}}{n} \quad (6)$$

where  $v$  is flow speed,  $r$  is the hydraulic radius, which is estimated from flow cross section,  $s$  the hydraulic gradient (downstream slope) of the channel, which is calculated from the ALOS

Palsar DEM, and  $n$  is the roughness coefficient, which is empirically determined. (Note, formally the roughness coefficient is dimensional, but typically changes in units are incorporated into a dimensional prefactor applied to equation 4, so that  $n$  can be taken to be dimensionless; see e.g. Chow, 1959 for details.)

Measurement errors in the hydraulic radius,  $\sigma_r$ , and hydraulic gradient,  $\sigma_s$ , are propagated into the estimate of the velocity, along with the epistemic uncertainty in the roughness coefficient,  $\sigma_n$ , so that the uncertainty of the velocity can be estimated as

$$\frac{\sigma_v^2}{v^2} = \left( \frac{2\sigma_r}{3r^{2/3}} \right)^2 + \left( \frac{\sigma_s}{2s^{1/2}} \right)^2 + \left( \frac{\sigma_n}{n} \right)^2.$$

(7)

Estimating the hydraulic radius relies on the cross-section area and wetted perimeter, both of which have substantial uncertainties (recalling our order-of-magnitude estimate gives a ~20% relative error in the cross-section area). However, the cross-section is correlated with the perimeter, and this reduces the error in the hydraulic radius. The 12.5 m resolution of the DEM means that the hydraulic gradient is likely have relatively high uncertainty, but the epistemic uncertainty in the roughness coefficient is likely to dominant in many situations.

In this study, we determine the roughness coefficient  $n$  as the best match value in sectors where both a hydraulic radius and a speed estimated by either the runup height (equation (4) or superelevation (equation (5)) methods is available. Values of the roughness coefficient for natural streams vary from 0.03 for minor, straight, clean streams on a plain, 0.05 for mountain streams on cobbles and boulders and flows on brush covered flood plains, to 0.12 for flows on tree covered flood plains with flow depths reaching branches (Chow, 1959). For our calculation we use Manning values in the range 0.05 to 0.08 (details in section 2.5.3) consistent with these values for conditions at Calbuco.

Determination of the roughness coefficient requires consideration of the channel morphology and bed properties, as well as vegetation cover and flow condition (Arcement & Schneider, 1989). These can vary substantially over the length of the river, and may differ for different lahar pulses, as subsequent flows propagate in channels modified by erosion and deposition from previous pulses, and some pulses may overbank and interact with vegetation. Uncertainties in the value of the roughness coefficient are propagated into the estimated velocities, producing substantial uncertainties. For example, an uncertainty of  $\pm 0.01$  in the roughness coefficient for  $n = 0.05$  corresponds to an uncertainty of  $\pm 20\%$  in the calculated speed, and an uncertainty of  $n = 0.08 \pm 0.01$  gives an uncertainty of  $\pm 25\%$  in the speed.

While the Manning formula is easy to apply, there are limitations. The Manning formula was originally formulated for water flows at typical fluvial temperatures and gives satisfactory results for high Reynolds or turbulent flows (Brater et al., 1996). For lahars, the rheology of the flow is markedly different from water, and can change in space and time (Iverson, 2003). Despite this, the Manning equation has been used to estimate lahar speeds in different volcanic

environments with reasonable results (e.g., Laenen & Hansen, 1988; Worni et al., 2012; Jenkins et al., 2015). In accordance with the mixture theory of Iverson (1997) and Iverson & Denlinger (2001), intergranular fluids (with clay and silt carried in suspension) in a debris flow behave as a Newtonian viscous fluid. For dilute lahars, Jenkins et al. (2015) suggest the material behaves as a Newtonian flow, and therefore that the use of Manning's law is appropriate. However, for more concentrated lahars, such as debris flow, the rheology is non-Newtonian, and we expect the Manning formula to provide unreliable estimates. The calculation using the Manning formula gives an instantaneous velocity of the head or peak of the flow rather than a mean velocity between two locations along the thalweg.

Discharges were estimated with the area-velocity method (Hersch, 2003), using the velocities estimated with the methods described above and the cross-sectional area estimated for the flow at the locations of Figure 3. Field survey sites, sample codes and cross sections locations (details of cross sections in Figure 18 Figure 26 and Table 4).. These discharge estimations combine the uncertainties in the cross-section area and velocities, so that relative errors in excess of 20% are likely.

Since the aim of this study is to develop an overall quantitative and qualitative understanding of the dynamics of volcanic flows from the Calbuco 2015 eruption, we make use of each of the methods above, noting their limitations in the interpretation of the results. Such estimates of speed, despite their uncertainty, are useful as comparisons to existing studies where these techniques have been used.

#### 2.4.2.3 Componentry analysis

Lahars transport a mixture of particles incorporated directly at the source, but also entrain material in substantial volumes from the erosion of the channel walls and stream bed in a process known as bulking (Vallance, 2000). Analysis of the proportion of each component along the lahar deposit, and determination of their source, allows us to understand the behaviour of the erosional and depositional dynamics of lahars.

In this study, fourteen samples from the volcanic flow deposits from the 2015 eruption were collected from different locations along the Río Blanco (Figure 3), distributed from the source to the distal area. In some places, we sampled across the stream channel and in different beds of a deposit, to explore transversal and vertical changes, respectively, at a specific distance from source.

Samples were first dry sieved and the single fraction in the range  $\phi_1 - \phi_2$  (250-500  $\mu\text{m}$ ) examined using a stereoscopic microscope (model Nikon SMZ745T). The use of a single size is a standard method to compare componentry of different samples (Halper et al. 2011), and this size was chosen because (i) particles can be easily identified in the stereoscopic microscope, (ii) all samples have a statistically robust representative mass to compare, and (iii)



a sand-sized grain is likely to be neither rapidly deposited nor held in suspension for long durations (a voluminous fraction like gravel sized grains are likely to be highly sensitive to flow energy loss and rapidly deposit, while fine silt and clay fractions have a relatively high transport capacity and held in suspension in the fluid phase of a lahar). Sediment grains were classified in 4 groups (juveniles, lithics, crystals and altered) which are a common first level of classification for volcanic ash (Gaunt et al. 2016; Benet et al. 2021) or sedimentary volcanic deposits (Halper et al. 2011). Due to the wide range of sediments encountered, a second level of classification is necessary, and here we have used the categories proposed by Benet et al. (2021), i.e., crystallinity, vesicularity (juveniles) and alteration (lithics) and morphological parameters including sphericity and rounding. For each sample, approximately 150-180 grains were counted.

Given the scope of this work, the counting of components is done to get a first notion of the components and their proportions along the flow, without performing a detailed quantitative analysis or automated particle counting through specialized softwares.

## 2.5 Results

### 2.5.1 Initial and pre-eruptive conditions of the valley and glacier

Photographs taken in an overflight performed on 9<sup>th</sup> March 2015 by a member of OTPV (Sernageomin), 44 days prior the eruption, provide an overview of the southern valleys of Calbuco preceding the eruption. This set of images shows no snow cover on the volcanic summit (Figure 7A, B) and provides a general view of the valleys and depositional plain of the Río Blanco and Río Este rivers, where characteristics such as a well-developed vegetal cover, active channels of water flow and the Chapo lake coastline shape can be recognized. These provide a useful basis for a comparison with post eruption images. Figure 7 show the pre-eruptive conditions that could be compared with post eruptive images (e.g. Figure 15 and Figure 16).

In addition, photographs of Calbuco on Twitter published by the community one week before the eruption and likely (in most cases) taken on the same day of the posting, show the volcano without snow (Nuñez, 2015; Arel Silva, 2015). However, inhabitants of the southern area of Calbuco volcano, report snowfall on the summit of the volcano just a few days prior the eruption (24horas.cl, 2015), and a thin snow cap in the vicinity of the glacier could be observed from videos and photographs of the initial stages of eruption.

These observations are consistent with meteorological data recorded at Lago Chapo station (DGA), which reports 123.20 mm of rainfall from 12 April to 19 April 2015. For autumn in the study area, a meteorological model proposed by Miranda (2019) predicts a mean zero-degree isotherm at 2614 m a.s.l., 611 m above the volcano summit, and therefore only a thin snow cap

on the volcano is expected in early—mid April. This suggests that, in the absence of syn-eruption rainfall, the glaciers are likely to be the most important source of water for lahars during the 2015 eruption, with significantly less contribution from snow and water trapped in saturated substrates.

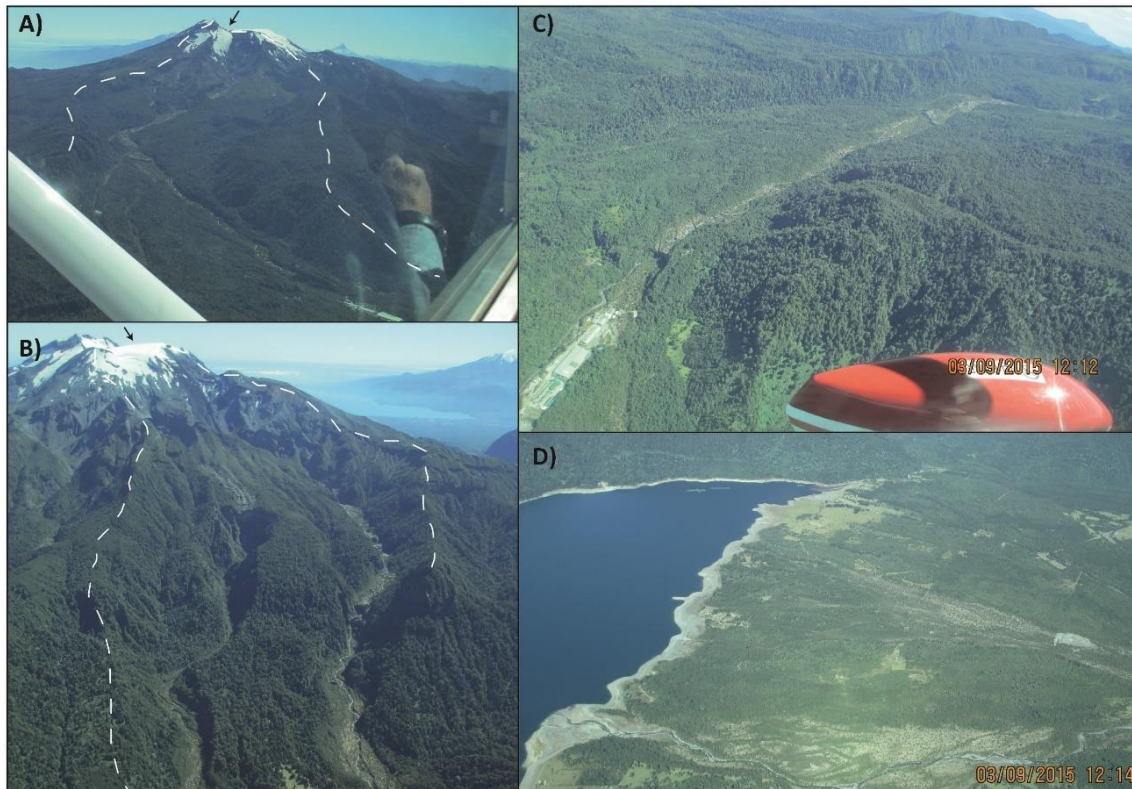


Figure 7. Aerial photographs of Calbuco and the southern valleys taken on 09/03/2015, seven weeks before eruption. A) Rio Blanco basin catchment area from south. B) Rio Este-Amarilla basin catchment area from south. For A) and B), white dashed lines represent basin borders, and black arrow indicate the glacier. C) Rio Blanco valley proximal-medial area. D) Chapo lake depositional fan and its coastline. Credits to Mauricio Mella (SERNAGEOMIN).

High resolution satellite images available in the Google Earth historical repository (Google Earth, 2012), allow us to distinguish and map seven different glaciers on the Calbuco summit (Figure 8). In Table 2 we list the area, mean slope, and median elevation of the seven glaciers, as determined from analysis of the Google Earth imagery, taken on 19<sup>th</sup> March 2012 (Google Earth, 2012). Additionally, it is possible to estimate hydrological parameters for each glacier (Table 2) using ice thickness data from the Chilean National Glacier Inventory (DGA, 2015). We estimate the volume of each glacier using the area and mean thickness. Assuming an ice density of 900 kg/m<sup>3</sup> (Huss, 2013), we estimate the equivalent liquid water volume from each glacier. This provides an estimate of the maximum water contribution from melting of glacial ice, which for the Río Blanco basin is  $11.3 \times 10^6 \text{ m}^3$ , for Río Este is  $8.1 \times 10^6 \text{ m}^3$ , and for Río Amarillo  $2.5 \times 10^6 \text{ m}^3$ .

Examining the mean slope of the glaciers allows us to identify *intra caldera glaciers*, which have values in the range 18°--23° (glaciers 6 and 7 in Figure 1), and *outer caldera hanging type*

glaciers, with a mean slope of  $28^{\circ}$ -- $34^{\circ}$  (glaciers 1 to 5 in Figure 8). An additional, notable characteristic is the occurrence of a high density of crevasses in the East Rio Blanco glacier (glacier 3 in Figure 8) and in the south-east area of the Caldera glacier (glacier 6 in Figure 8). In both cases the largest crevasses are perpendicular to the mean slope direction with  $\sim 10$  m width and  $\sim 100$  m length for the main fractures in glacier 3, and  $\sim 15$  m width and  $\sim 250$  m length for the main fractures in the south-east area of glacier 6. Considering the slope and crevasse density as key factors for stability, hanging and highly fractured glaciers are the most susceptible to a mechanical collapse which could subsequently release water as a mechanism for lahar triggering. The estimate of the likely total volume of water from “unstable” ice for Río Blanco is  $4.4 \times 10^6 \text{ m}^3$ , for Río Este is  $4.5 \times 10^6 \text{ m}^3$ , and for Río Amarillo  $1.3 \times 10^6 \text{ m}^3$ .

*Table 2. Hydrological values for glaciers in the southern drainage basins of Calbuco volcano. The areas, mean slopes and median elevations ( $H_{\text{median}}$ ) of the glaciers are estimated from Google Earth aerial imagery and ALOS Palsar DEM. The mean depth of the glacier is obtained from the Chilean National Glacier Inventory (DGA, 2015). The glacier volumes are estimated as the product of the area and mean depth, and the liquid water equivalent volume is calculated assuming an ice density of  $900 \text{ kg/m}^3$  (Huss, 2013). See Figure 8 for a map of locations of the glaciers.*

Glacier	Basins of drainage	Area [km <sup>2</sup> ]	Mean Depth [m]	Mean Slope [degrees]	$H_{\text{median}}$ [m a.s.l.]	Volume [ $\times 10^6$ m <sup>3</sup> ]	Liquid water equivalent [ $\times 10^6 \text{ m}^3$ ]
<b>1: West Glacier</b>	Pescado river	0.034	9	30	1876	0.306	0.36
<b>2: West Blanco River Glacier</b>	Río Blanco river	0.096	13	34	1705	1.248	1.47
<b>3: East Blanco River Glacier</b>	Río Blanco river	0.13	14	34	1718	1.82	2.14
<b>4: South Glacier</b>	Río Blanco river	0.018	26	28	1770	0.468	0.55
<b>5: East Glacier</b>	Este-Amarillo rivers	0.02	26	34	1603	0.52	0.61
<b>6: Caldera Glacier</b>	Río Blanco, Este-Amarillo, Colorado, Tepu and Blanco-Hueñu Hueñu Rivers	0.88	22	18	1833	19.36	22.78
<b>7: East Caldera Glacier</b>	Pescado and Río Blanco rivers	0.12	13	23	1915	1.56	1.84

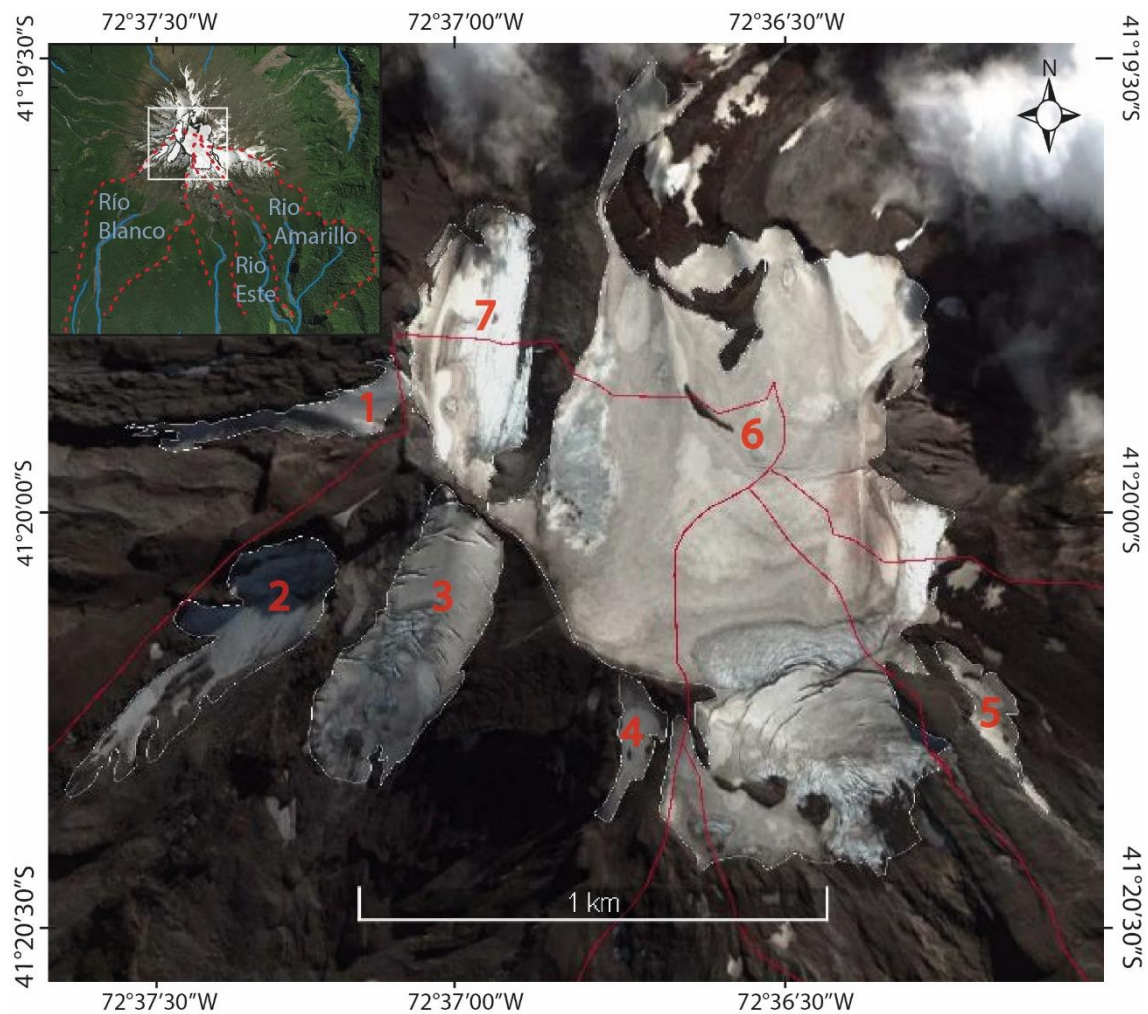


Figure 8. Satellite image of the glaciers of Calbuco, taken on 19<sup>th</sup> March 2012 (GoogleEarth, 2012). Glaciers 2, 3, 4 and part of glaciers 6 and 7 are in the catchment area of Rio Blanco basin. The southern part of glacier 6 drains towards Rio Este. Glacier 5 and the southeastern sector of glacier 6 are emplaced in the high zone of Rio Amarillo. Note there is a high density of crevasses and fractures in glaciers 3 and in the south - southeastern zone of glacier 6. Red lines indicate the boundaries of drainage basins.

## 2.5.2 Eruption chronology and characteristics of surface volcanic activity

The 2015 Calbuco eruption had two main paroxysmal pulses on the 22<sup>nd</sup> and 23<sup>rd</sup> April. Previous work provides details of the precursory activity, eruption triggering mechanism, large scale physical measurements and impacts (section 2.3). However, there is no complete chronology of the eruption, in particular in relation to the generation and propagation of lahars. Here we analyze observations of the volcanic plume and activity in the valleys in order to reconstruct the chronology of volcanic flows, determine vents positions and their dimensions, and identify the valleys impacted.



### 2.5.2.1 1st Pulse (21:04 – 22:30 UTC, April 22nd)

The analysis of photographs and videos of the eruption allow us to distinguish three main stages during the first pulse that occur as the eruption column evolves in time (Figure 9) which we identify as: (1) initial stage of vent opening and ascent of the starting plume (21:04 ~ 21:15; Figure 9A and 9D); (2) period of quasi-steady eruption column dynamics (~21:15 ~ 22:00; Figure 9B and 9E); and (3) cessation of the first pulse with a partially collapsing column (~22:00 ~ 22:30; Figure 9C, 9F). In Figure 9 and Figure 10, the pictures in the upper row have similar scale and show the entire column from vent to plume top, while the lower row images focus on surface process on the volcanic edifice.

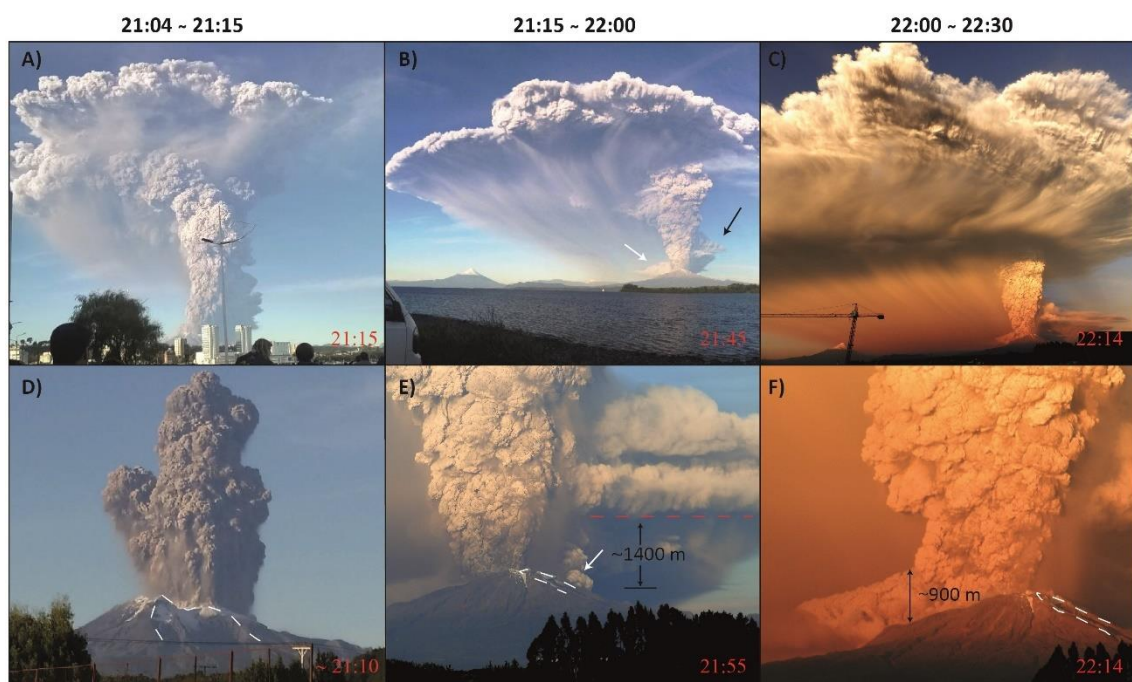


Figure 9. Photographs of the eruption column at different times (as shown in the images) of the first eruptive pulse of the 2015 Calbuco Eruption. Upper pictures have similar scale and show the entire column from vent to neutral buoyancy, while the lower pictures focus on surface process on the volcanic edifice. Dashed white lines on the images indicate the Rio Blanco river basin boundaries. Photographs in the left column (A,D) correspond to the initial stage of vent opening and the transient starting plume. Photographs in the centre column (B,E) show the period for which there is a quasi-steady buoyancy-driven plume. Photographs in the right column (C, F) show the late stage of the first pulse. Image A is taken from Puerto Montt, southwest of the vent. Images B and E are taken from Puerto Varas, East of the volcano. Images C and F are taken from Puerto Varas. Image D is taken from Chamiza-Correntoso, south-southwest of the volcano). Credits: @N3urOottica (2015) for image A; @Sernageomin for Image B, @zepellin\_lh (2015) for Image D. Images C, E and F credits to Natalia Garrido (SERNAGEOMIN).

Photographs in the left column (Figure 9A and 9D) correspond to the initial stage of vent opening and the transient starting plume. Figure 9A is taken from Puerto Montt (~30 km South-West of the volcano) and shows the incipient umbrella cloud at the top of the plume and bending of the plume trajectory by atmospheric winds. Figure 9D is taken from Chamiza-Correntoso (~15 km south-southwest of the volcano) and is the earliest image in the sequence showing the initial explosive pulse and early formation of the volcanic jet that forms the eruption column. The dark colour of

the jet indicates a high concentration of pyroclasts. This is also visible in the lower plume in Figure 9A, taken ~5 minutes after the image in Figure 9D.

Photographs in the centre column (Figure 9B and 9E) are taken from Puerto Varas (30 km east of the volcano) during the period for which there is a quasi-steady buoyancy-driven plume, approximately 35 minutes after initiation. We observe a white cloud forming at the base of the column (indicated by the white arrow in Figure 9B), in contrast to the dark colour seen earlier in the eruption. This could indicate incorporation of water vapour in the lower plume.

We also note the incipient secondary intrusion (indicated by the black arrow in Figure 9B) at a neutral buoyancy height below the extensive main umbrella cloud. The secondary intrusion is likely due to ascent of a co-ignimbrite plume (Carey and Bursik, 2000) formed in the NE to SE area of the vent (Figure 9B and 9E). A co-ignimbrite plume forms from a pyroclastic density current due the entrainment and heating of air and volcanic gases and the simultaneous sedimentation of particles (Carey and Bursik, 2000; Dufek, 2016) in a coupled process that enhances a gas particle-drag regime and the onset of a buoyancy-driven plume above a denser granular regime. The interaction of the pyroclastic density current with ice and the addition of water vapor, increase the gas proportion in the current and change the temperature of the pyroclastic-air mixture, as well as enhance the aggradation of particles (Bonadonna et al., 2011). Therefore, the water vapor derived from melting of the glacier is likely playing a role in the intensity of buoyancy force acting. This smaller plume was dispersed at low heights ( $< \sim 1500\text{m}$  above the vent) to the SE direction, where inhabitants, 8 km from volcano, reported traces of ash fall-out. These features are shown in detail in Figure 9E with the white arrow indicating a secondary co-ignimbrite plume, rising above PDCs that are descending to the southeast, which ascend to a neutral buoyancy height  $\sim 1400\text{ m}$  above the vent, marked by the red dashed line.

Photographs in the right column (Figure 9C and 9F) show the late stage of the first pulse, approximately one hour after initiation. These images show extensive tephra fallout visible from the umbrella cloud in Figure 9C. We also note there is partial collapse of the plume to the north of the vent in Figure 9F. Column collapse can result from a variation of the eruption rate, and/or a change in the pyroclast concentration and size distribution (Woods 1998; Michaud-Dubuy et al 2018), so that the erupted material does not become buoyant. The mass eruption rate and gas content at the vent are primary controls on the column collapse condition (Wilson, Sparks & Walker, 1980; Carazzo, Kaminski & Tait, 2015), although the vent and crater geometry (Koyaguchi & Suzuki, 2018) and clast density (Shea et al., 2011) also influence column stability. Column collapse may be partial, with the near-source jet separating into a dense fountain and buoyant plume (Carazzo, Kaminski & Tait, 2015). The conditions of partial collapse are not well characterized but are thought to occur when eruption conditions are close to the buoyant—collapse transition (Michaud-Dubuy et al 2018). The partially collapsing column provides dilute pyroclastic material to pyroclastic density currents (Sparks & Wilson 1976) with experiments and field studies indicating that approximately 40% of the erupted mass is partitioned into pyroclastic density currents during partial collapse (Carazzo, Kaminski & Tait, 2015).

The timing of the three stages inferred from photographs match relatively well with the Real-time Seismic Amplitude Measurement (RSAM; Endo and Murray, 1991) trend of the nearest seismic station to Calbuco (located 5 km from the 2015 vent) presented by Valderrama et al. (2016). RSAM values show a clear increase during first ~40 minutes of eruption, then ~30 minutes of a peak plateau of values, followed by a decrease in the last ~20 minutes of first pulse (Valderrama et al., 2016). Moreover, our observations of three distinct stages during the first pulse are consistent with the eruption model proposed by Romero et al (2016), which is based on tephra deposits and plume observations, of an initial stage of explosive activity, reaching a paroxysmal phase, and followed by a less energetic final phase with a collapsing column.

Further support of the progression of the first eruptive pulse can be inferred from other photographs and video taken from different directions and at different times, as shown in Figure 10. Photographs in the upper row of Figure 10 are taken from north provide a good perspective to locate the 2015 vent. This crater is the same vent as the 1961 lava flows, which was the last eruptive activity of Calbuco prior to the 2015 eruption and is directly emplaced over the upper area of the northeast drainages basins of the volcano, on the northeast sector of the amphitheater morphology left by the collapse and debris avalanches of the volcano, 14 ka ago (Figure 2; Selles et al. 2011), that characterizes the top of the volcanic edifice. This amphitheater is open and has a slope to the northeast, and therefore the vent location enhances volcanic flows and pyroclastic transport towards the Río Tepu and Río Blanco-Hueñuñu river systems located on northeast flank of the volcano. Figure 10B and 10C show pyroclastic density currents descending to northeast valleys (white arrow in Figure 10B).

Photographs in the centre row in Figure 10 are taken from east. Figure 10D shows the partial collapse of the eruption column (indicated by the left white arrow). Additionally, the photograph provides evidence of a secondary vent (indicated by the dashed white line). Figure 10E is a close-up view of the near-vent region from which we observe ballistics falling onto the glacier. We note the appearance of low-level white-coloured clouds over the fall-out zone that may result from ice-melting by the hot ballistics and indicate a source of water for volcanic flows. In Figure 10 we observed that parts of the margin of the eruption column, over the glacier area (white lines in Figure 10), appears to be a lighter gray colour. In other eruptions, observations of light grey and white parts of eruption columns have been interpreted as indicating an elevated concentration of water vapour in the mixture (e.g. Prata et al., 2017). Water vapour during the Calbuco eruption could be sourced from intense pyroclastic-ice interaction, producing steam that is entrained into the eruption column and mixed with magmatic gases.

The lower row of photographs in Figure 10 are taken from the southwest and south. Figure 10G and 10H show a PDC and lahar descending in Rio Amarillo valley (indicated by the white arrow in Figure 10G). In contrast, there is a noticeable absence of activity in the Rio Blanco basin (demarcated by the dashed line in Figure 10H). Figure 10I, taken during the late stage of the first pulse, shows that the glaciers on the western and southern valleys have received relatively little pyroclastic material.

Figure 11 presents a pair of aerial photographs of the first pulse taken from the southeast. We note the clouds ascending in Río Este valley (Figure 11A, image from biobiochile.cl, 2015), with a colour indicative of a mixture of pyroclastic material and steam. In contrast, there is no discernible lofting of material above the Río Blanco basin. Figure 11B (extracted from CHV Noticias 2015) shows the southern area of crater. We note the intense vapour release from the glacier area in the catchment of Río Pescado and Río Blanco basin, suggesting active interaction of volcanic products and ice.

The compilation of photographs shows that, during the first pulse, volcanic flows, and ice melt occurred mostly in the N to SE (clockwise direction) basins. In addition, the photographs show vapor cloud in some valleys (e.g. Figure 10E and 10G) which we infer as being related increases in river discharge. At the end of the first pulse, images reveal some interactions between the plume, ballistic fragments and ice in the east and southeast border of the amphitheater on the volcanic edifice, in the upper area of Río Blanco and Río Pescado valleys (Figure 10 and 11). In addition, photographs taken ~ 1.5 hours after the end of the first pulse (Aletto75., 2015), clearly show an area of burning on the north flank of volcano, likely as a consequence of the pyroclastic density currents descending in these directions.

Twitter posts from authorities and emergency services (@GobiernodeChile, 2015; @munipuertomontt, 2015; @CBPMO, 2015) suggest that evacuation of most of community of Lago Chapo village began after the end of the first pulse, so it is reasonable to infer that, bridges in Correntoso and Río Blanco rivers, on the south flank, had not collapsed yet, allowing vehicles to pass. Note that later, many of the bridges of Río Blanco were completely destroyed by lahars and the road link to Lago Chapo was only re-established several weeks after the eruption (Hayes et al. 2015).

Discharge measurements from Río Blanco Ante Junta Río Chamiza gauge station (taken hourly) show a dramatic increase from 1.3 m<sup>3</sup>/s to 2 m<sup>3</sup>/s at 23:00 UTC (Figure 12). This is likely related to ice melting by pyroclasts delivered to the south and southeast of the volcanic amphitheater during late stages of the first pulse (22:15 – 22:30). The 23:00 measurement of the station is attributable to the embankment of sand, which obstructed the supply of water to the water level sensor (DGA, personal communication). Thus, the sensor was unable to take accurate measurements of the discharge after 23:00, so these later values of discharge do not represent the lahar flow height.





Figure 10. Photographs taken from different directions and at different times during first eruptive pulse. Photographs in the upper row are taken from north giving a view of the vent emplacement. The red arrows in panels A, B, G and H indicate the west wall 14ka collapse amphitheatre. The white arrow on panel B indicates the direction of propagation of the pyroclastic density currents descending to northeast valleys. Photographs in the centre row are taken from east. In panel D we note the partial collapse of the eruption column is indicated by the left white arrow), a secondary vent (dashed white line), and a low-altitude atmospheric intrusion of dilute pyroclastic material (right white line). Panel E shows 'streaks' corresponding to ballistic ejecta falling onto the glacier and low-level light coloured clouds lofting from the glacier (the topographic relief is indicated by white dashed lines). On panel F, white arrows indicate lighter colouring of the margins of the low level plume over the glacier area. Photographs in the lower row are taken from southwest and south. The white arrow on panel G gives the propagation direction of flows descending in Rio Amarillo valley. On panel H, the Rio Blanco basin is demarcated with the white dashed line. Credits: Juan Francisco Veintimilla, 2015 (Image A); Paislobo Prensa, 2015 (Image B); Francisco Molina 2018 (Image C); Natalia Garrido (SERNAGEOMIN, Images D, E and F). Guioteca.com (2015) for Image G AFP PHOTO/STR.

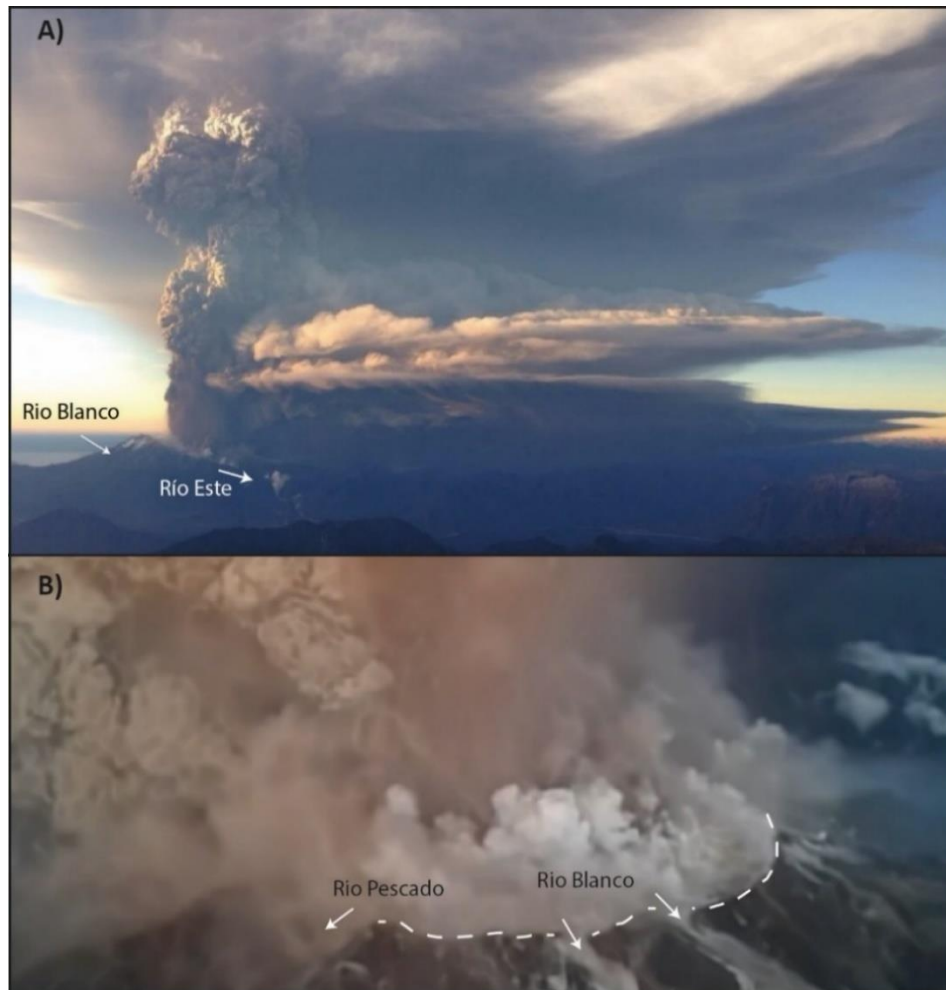


Figure 11. A) Image from first pulse of the eruption taken from southeast of the vent. Note the clouds rising above the Río Este valley and a “clean” Río Blanco basin (image from biobiochile.cl, 2015). B) Image of the southern area of the crater. The crater rim is demarcated by the dashed white line and the heads of the Río Pescado and Río Blanco basins are indicated (extracted from CHV Noticias 2015).

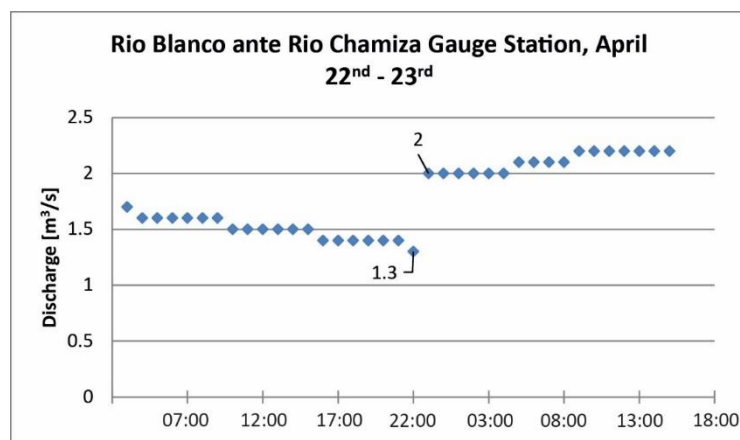


Figure 12. Discharge at Río Blanco ante Río Chamiza gauge station. Note the dramatic rise in discharge at 23:00 (22-04-2022) measurement (data from DGA).

#### 2.5.2.2 2<sup>nd</sup> Pulse (04:00 – 10:15 UTC, April 23<sup>rd</sup>)

In comparison with the first pulse of eruptive activity on 22<sup>nd</sup> April, there are significantly fewer records in social media of the second pulse, likely as most people were sleeping at the time of onset (01:00 to 07:15 local time), there were many fewer witnesses in areas around the volcano as evacuations had commenced and, moreover, night-time photography requires specialist knowledge and equipment. However, some professional photographs and video recordings are available on the web and in the press (Cooperativa.cl, León Cabello 2015), mainly taken from the west of the volcano in Puerto Varas city and from northwest in Frutillar (40 km from the volcano).

The audiovisual record of the second pulse shows intense incandescence and the occurrence of forest fires on the northern and eastern flanks of the volcano. This suggest a major collapse of the column which was able to exceed the 100m high eastern wall of the amphitheater rim, located 700m to the east of the initial vent of the eruption. In addition, post-eruption public and official posts on twitter (@mop\_chile, 2015a; @mop\_chile, 2015b; @mop\_chile, 2015c; @vdj\_ivan\_beroiz, 2015; @grandepatagonia, 2015; @carlitadegaby, 2015), reported the major collapse of Colorado, Rio Blanco, Tronador and Zapatero bridges, located on the south and east drainage streams of Calbuco, and the occurrence of a lahar with widespread inundation in Rio Blanco and Correntoso (@latercera, 2015; @ptomontt\_histor, 2015, soychile.cl, 2015).

When comparing geophysical measurements of the two main eruptive phases of the eruption, such as seismic energy (Valderrama et al., 2015), infrasound acoustic amplitudes (Matoza et al., 2018) and lighting strike frequency (Van Eaton et al. 2016), the second pulse exhibits higher values. The volcano tectonic (VT) seismicity of the second pulse has a notable increase in both events per hour and magnitudes at ~05:00, with a rise from 0 to 200 per hour approximately during the 05:00 to 07:00 period, when  $M_L$  magnitudes ranged between 2.5 to 3.5 (Valderrama et al. 2015). This rise in the number and magnitudes of VT could be associated with an increase in the magma eruption rate or other changes in the magma source which eroded the conduit and eventually open secondary vents. Moreover, during the second pulse Castruccio et al. (2016) identify directly from on-site observation that there was a notable shift in column behaviour and an increase of lighting and incandescence at 6:30 UTC. This change has also been recognized by Matoza et al. (2018) and Van Eaton et al. (2016), who interpret them as indicating the occurrence of major pyroclastic density currents.

#### 2.5.2.3 Water levels in Chapo lake

Monitoring of the water level in Chapo lake provides a record from which we can infer changes in the discharges of the river systems draining into the lake. Chapo lake provides a reservoir of water used by the Canutillar Power Plant, so monitoring of water levels is frequent and reliable.

The time-series of the Chapo Lake level from 20<sup>th</sup> to 26<sup>th</sup> April, shown in Figure 13, has five distinct phases during the week. First, from 20<sup>th</sup> April to midday on the 21<sup>st</sup>, the lake remains in a quasi-constant level. This was followed by a continual decrease in water level for approximately one

day, until ~22:00 UTC on 22<sup>nd</sup> April. From 22:00 on 22<sup>nd</sup> April until 08:00 on 23<sup>rd</sup> the trend of declining lake level was interrupted, and the measured values began fluctuating, with a slight trend to increase from 04:00 23<sup>rd</sup> April. Subsequently, there was an abrupt 6 cm increase in the water level that occurred rapidly between 08:00 and 09:00 (UTC). Finally, from around midday of 23<sup>rd</sup> April and to at least the end of the 26<sup>th</sup> April, the water level of Chapo lake returned to a constant steady rate of decrease.

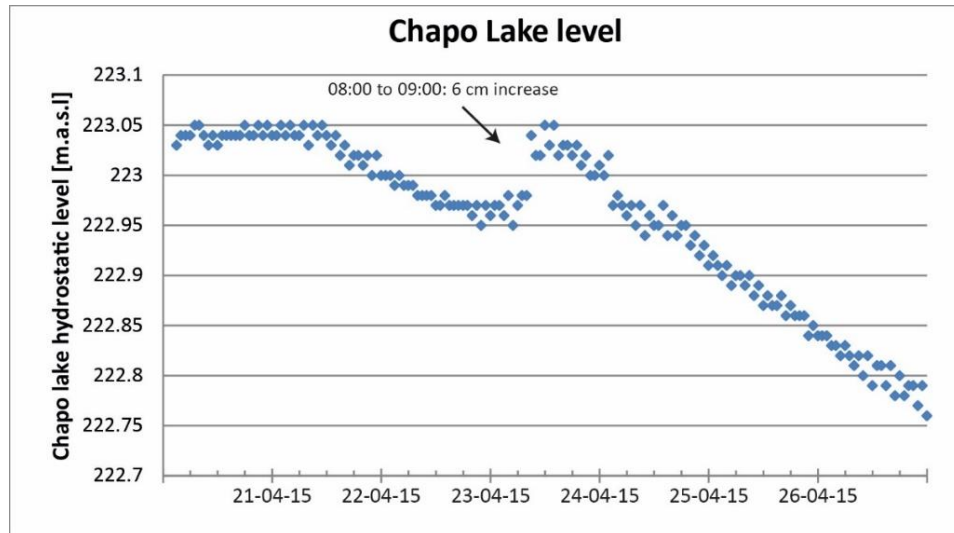


Figure 13..Time series of hydrostatic water level at Chapo lake. Notice the dramatic, 6 cm rise at 05:00-06:00.

The trend of steadily decreasing water level that is prominent at the end of the time period (12:00 on 23<sup>rd</sup> to 26<sup>th</sup> April), but also is observed from 12:00 on 21<sup>st</sup> to 22:00 on 22<sup>nd</sup> April, is likely to represent the regular extraction of water for use at the power plant compensated by the flow of rivers in the steady regime of the season. The initial constant lake level is likely to be due to increased discharge in the river system associated with a rainfall event on 12<sup>th</sup>—19<sup>th</sup> April.

The transition from a decreasing water level to a fluctuating level on 22:00 22<sup>nd</sup> April cannot be explained by rainfall in the catchments. However, the timing is consistent with an increase in the discharge to Chapo lake through Rio Blanco and Rio Este due to glacial melting associated with the first eruptive pulse.

The rapid increase of the water level during the early morning of 23<sup>rd</sup> April is remarkable, with the level increasing by 6 cm in the 08:00 – 09:00 (UTC) period. This rise is clearly an anomalous change in the trend of the water level variation. The timing of this increase strongly suggests it is the result of eruptive activity related to the second explosive pulse. Based on a surface area of Chapo lake of 45.4 km<sup>2</sup>, we estimate that a 6 cm increase in water level represents an increase in volume of  $2.7 \times 10^6$  m<sup>3</sup>. We attribute this volume to the discharge of lahars into Lake Chapo during the second pulse of the eruption.



## 2.5.3 Volcanic flows and deposits

### 2.5.3.1 Glacier and proximal flows

In the 2015 Calbuco eruption, proximal (< 8 km) volcanic processes include those which are typical in sub-Plinian explosive eruptions such as pyroclastic density currents and ballistic projections (Cioni et al. 2015). Most of the activity was located in a 500 m diameter vent, although observations of a grey tephra fall distribution, pyroclastic cone morphologies and a secondary jet region at the base of the column (Figure 10D and 10E) suggest the existence of two additional vents to the south of the main crater, forming an NNW alignment (Figure 14 and Figure 15A). However, these observations, are not sufficient to conclude that the two southern vents emitted material during the 2015 eruption, as they may be inherited morphologies of previous eruptive activity.

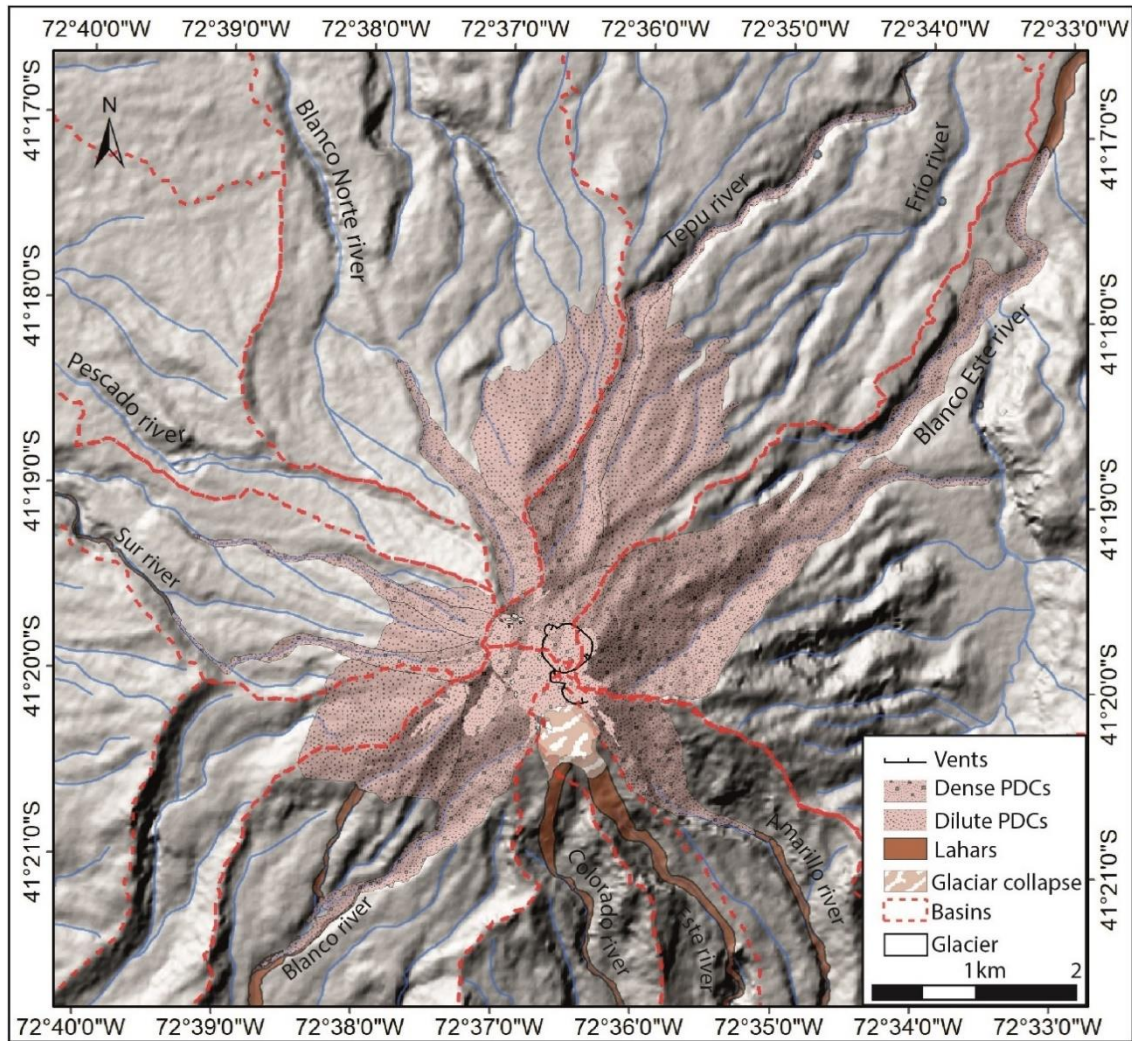


Figure 14. Emplacement map of pyroclastic density currents.

Glaciers were completely covered by ash, and in some cases eroded by thermal transfer and mechanical collapse as revealed by the scar at the head of Rio Este basin in the south area of the volcanic amphitheater (Figure 14 and Figure 15). There are some noticeable concentric holes and depressions (Figure 15A) that appear similar to pipe morphologies observed in lahar deposit of the 1991 Hudson eruption (Branney & Gilbert, 1995) that were interpreted as collapse structures caused by melting of trapped ice blocks beneath the pyroclastic material and the escape of water vapor.

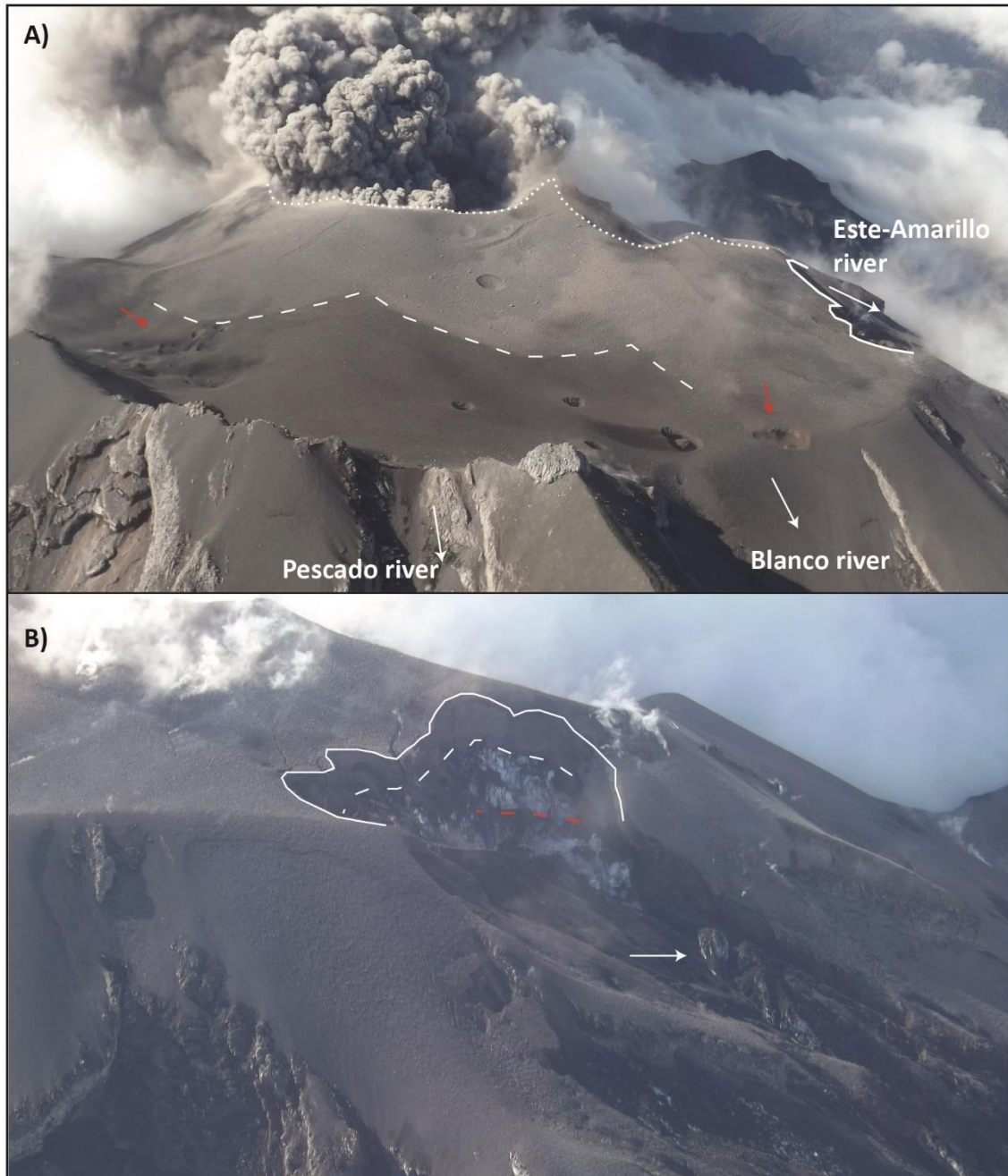


Figure 15. Photographs taken on 25<sup>th</sup> April, 2015. A) Crater and tephra deposit view. Red arrows indicate concentric depressions and pipes likely formed by melting of buried glacial ice and degassing of the water vapour. B) Glacier disturbance on the southern flank. There is a complete collapse of an ice block (white arrow). The estimate of ice thickness is 35m and the tephra deposit thickness is 25m.

Pyroclastic flow deposits were mapped from field surveys, interpretation of images taken on the ground, from helicopter overflights and from satellites, during and post-eruption, and of images and videos on social media (e.g. YouTube). These observations allow us to identify (1) lobe morphologies, fronts, channels or levees similar to the features described by Calder et al. (2000) for the PDCs of Lascar volcano in 1993, (2) deposits with indications of gas and water vapor emanation, (3) trees with erosion features such as fallen branches and leaves, burning, and changes in orientation that is similar to features observed at Chaitén volcano (Major et al., 2013), and (4) fires and co-ignimbrite clouds (Brown & Andrews, 2015).

Pyroclastic density currents deposits are emplaced in two forms: (1) vent-symmetric non-channelized at source and in proximal areas, where incisions in topography are not sharp and valleys are not deep; and (2) channelized high mobility flows in the Sur, Blanco Norte, Tepu, Blanco Este, Amarillo and Blanco rivers.

The unconfined flows can be separated in two sub-facies. In the crater area, a dense very proximal sub-facies (<1.5 km from vent) which covers the entire surface of the glacier and overtops the ~100 m topographic barrier in the western area of the volcano summit to reach distances up to 1.5 km in the Correntoso, Sur and Pescado river catchments (Figure 15 and Figure 16A,B). This sub-facies likely accounts for most of the dark-grey tephra deposit observed over the ice in the Este river collapse scar (Figure 15) where in the centre of these deposits, a temperature close to 250°C was measured using a thermal camera from a helicopter overflight few days after the eruption (Mella et al. 2015), although tephra fallout from the column will also contribute. This sub-facies evolves transitionally to the dilute unconfined sub-facies that reach distances from the vent up to 3.5 km (Figure 16 C,D). This dilute flow impacted the forest relatively weakly, pulling branches from trees and locally toppling some tree trunks, and triggered fires on the northern flank (Blanco Norte and Tepu basins) during the first pulse, and in the western valleys (Sur, Correntoso y Blanco rivers) during the second pulse.

The channelized sub-facies have runout distances in the range 2.5--7.5 km (Table 3), with their maximum length in northeast direction toward the Tepu and Blanco Este rivers. The deposit exhibits two different surfaces: a single, uniform surface deposit (Figure 16E and 16F); and highly lobate deposits (Figure 16E, 16F, 16G and 16H). Similar lobate pyroclastic flow deposits were formed during the 1993 eruption of Láscar, and were interpreted by Calder et al. (2000) as likely associated with multiple collapsing pulses aggrading to form the deposit.

The upper part of the Rio Este basin exhibits a ~25 m thick tephra deposit on the glacier, recognized by the author from an overflight a few days after the eruption (Figure 15), in this place a temperature in the range 200-230°C was measured in the deposits few days after eruption (Mella et al. 2015). This deposit was not attributed to ash fall in previous studies (Castruccio et al. 2016, Romero et al. 2016). Degassing of a whitish gas, possibly composed of water vapor, from this deposit persisted for several weeks after the eruption. This observation is consistent with a hot emplacement on the glacier. In addition, we identify notable erosional features in this area including a collapse scarp in the ice (Figure 15B), with a loss of glacier area of 0.22 km<sup>2</sup>, in



a zone where lava bedrock, covered by the glacier prior to the eruption was exposed, and ice blocks of several meters in size disintegrated and accumulated at the foot of the slope (Figure 15B). Downstream in the Río Este valley, ~4.5 km away from the vent, a partially charred log was found oriented in the direction of flow in a lahar deposit (Figure 17), suggesting the emplacement of hot pyroclastic material in this area or upstream, with sufficiently high temperature to char wood.

These observations, and the images of the sector during the eruption, lead us to propose the occurrence of multiple simultaneous processes in the upper part of the Río Este basin, including intense fall of ballistic projectiles and tephra on the glacier, and hot pyroclastic flows, which would have destabilized the highly fractured ice mass in that sector prior to the eruption (Figure 8), triggering a collapse of the glacier and a mixed avalanche that evolved into a lahar in a zone 3-4 km downstream from the vent.

A summary of the main characteristics of the pyroclastic density currents during the 2015 eruption at Calbuco is presented in Table 3. The runout distance was estimated by the mapping of the deposits. The volume of the PDC deposit of Río Blanco was estimated as the product of the area covered, and the median thickness (4 m) measured in our survey (Figure 29). We include a classification by the occurrence of “lobes” which we define as elongated “*finger shaped*” features in the surface of the deposits, which we observe in the field to develop a coarse clast-supported juveniles-rich front (Figure 16G and Figure 29C) and are common in pyroclastic flows deposits (Brown & Andrews, 2015).

*Table 3 Summary of pyroclastic density currents during the Calbuco 2015 eruption. The runout distance is the estimated as the maximum extent of the deposit from the vent. We note whether the flows transitioned into primary lahars, and whether the pyroclastic deposits have a lobate morphology. High: indicating a deposit with abundant lobes, easy to recognise. Medium: refers to a deposit with low lobe concentration, or where the morphology is partially developed. Low: where a subtle lobe development is recognisable. None: where no lobule development is recognisable.*

Basin	PDC type	Occurrence time	Runout max [km]	Deposit Volume [ $10^6 \text{ m}^3$ ]	Area [ $\text{km}^2$ ]	$A/V^{2/3}$	Primary lahar?	Lobes occurrence?
Río Sur river (south drainage)	Dense - Unconfined	2 <sup>nd</sup> pulse	4	-	0.7	-	Yes	High
Río Sur river (north drainage)	Dense	2 <sup>nd</sup> pulse	3.8	-	0.52	-	No	Medium
Río Sur river	Dilute	2 <sup>nd</sup> pulse	1.6	-	0.41	-	No	None
Río Blanco Norte	Dense?	1 <sup>st</sup> and 2 <sup>nd</sup> pulse	3	-	0.88	-	No	Medium
Río Tepu	Dense	1 <sup>st</sup> and 2 <sup>nd</sup> pulse	7	-	1.46	-	No	None
Río Tepu	Dilute	1 <sup>st</sup> and 2 <sup>nd</sup> pulse	3.5	-	3.7	-	No	None
Río Blanco Este	Dense	1 <sup>st</sup> and 2 <sup>nd</sup> pulse	7.5	-	4.6	-	No	Low
Río Amarillo	Dense?	1 <sup>st</sup> and 2 <sup>nd</sup> pulse	2.5	-	0.88	-	Yes	None
Río Blanco	Dense	2 <sup>nd</sup> pulse	4.3	1.8	1.4	94.6	Yes	High



### 2.5.3.2 Flows in the North, East, and West valleys

Despite the occurrence of a large PDC on the north flank and the presence of ice in the upper zone of the northern valleys, the major primary lahars were generated in the southern basins. Only a few minor primary lahars were reported in the northern, eastern, and western valleys during the 2015 eruption that were confined to the fluvial channels. In particular, previous studies have reported and mapped a small lahar in Tepu river (Castruccio et al. 2016) on the northern flank, as well as a noticeable sediment delivery through Rio Blanco Este-HueñuHueñu that was attributed to fluvial transport of the tephra from the large pyroclastic density current emplaced in North and East valley (Castruccio et al. 2016).

On the western flank, the pyroclastic density current in the Rio Sur triggered a primary lahar which reached ~10 km from the source and subsequently diluted and transformed into a sediment-rich stream flow. This lahar remained channelized along all of the thalweg of the river without overflowing. The flow depth was up to 4 m, which was sufficient to destroy some wood bridges. We estimate a maximum total volume of ca.  $1 \times 10^5 \text{ m}^3$  for this lahar.

### 2.5.3.3 Río Este – Amarillo fluvial system

The Rio Este-Amarillo valley is a fluvial system fed by rain, snow and melt from Calbuco's glaciers that drains from the volcano to the south and discharges into Chapo lake (Figure 1, Figure 14 and Figure 18). The catchment area extends from the volcano summit, where lava flows form the main riverbed and are a source of large blocks (>1 m), and pyroclastic deposits are an important source of sediment. Within the first ~7 km from the upper point of watershed (the proximal area, Figure 18), the system is divided into two tributaries with similar discharges, the Este and Amarillo rivers., Slopes at the water source area are in the range 22°--26°, with a gradual decrease to ~8° at a distance of between 2.5 to 5 km (Figure 18 and Figure 19). In this proximal area, the valleys are narrow, and bedrocks of channel are mostly lava flows, cover by non-consolidated volcanic sediment that form terraces. In this section of the river, waterfalls of meters or tens of meters are common.

The two tributaries, Rio Este and Rio Amarillo, converge 5 km upstream of the discharge into Chapo lake (the medial area, Figure 18 and Figure 21), forming a single active channel until its mouth. In the last 3 km of the river before the outlet, the channel is divided in two semi-parallel branches, with only the east branch, called Rio Sin Nombre, being fluvially active at the time of eruption in 2015 (the distal area, Figure 18). Historically, both channels have been active, but the dynamics of the fluvial system has alternated the flow of water between them, and according to older local residents, the Rio Sin Nombre has been the active from ~70 years ago. Change in vegetation coverage (not attributable to human activity), fresh sandy deposits with poorly developed soil, channel morphologies, and large debris flows deposits, suggest that both channels have transported lahars in recent times, likely during the historical eruption, and confirm the sensitivity of the hydrological network to erosion-deposition processes.

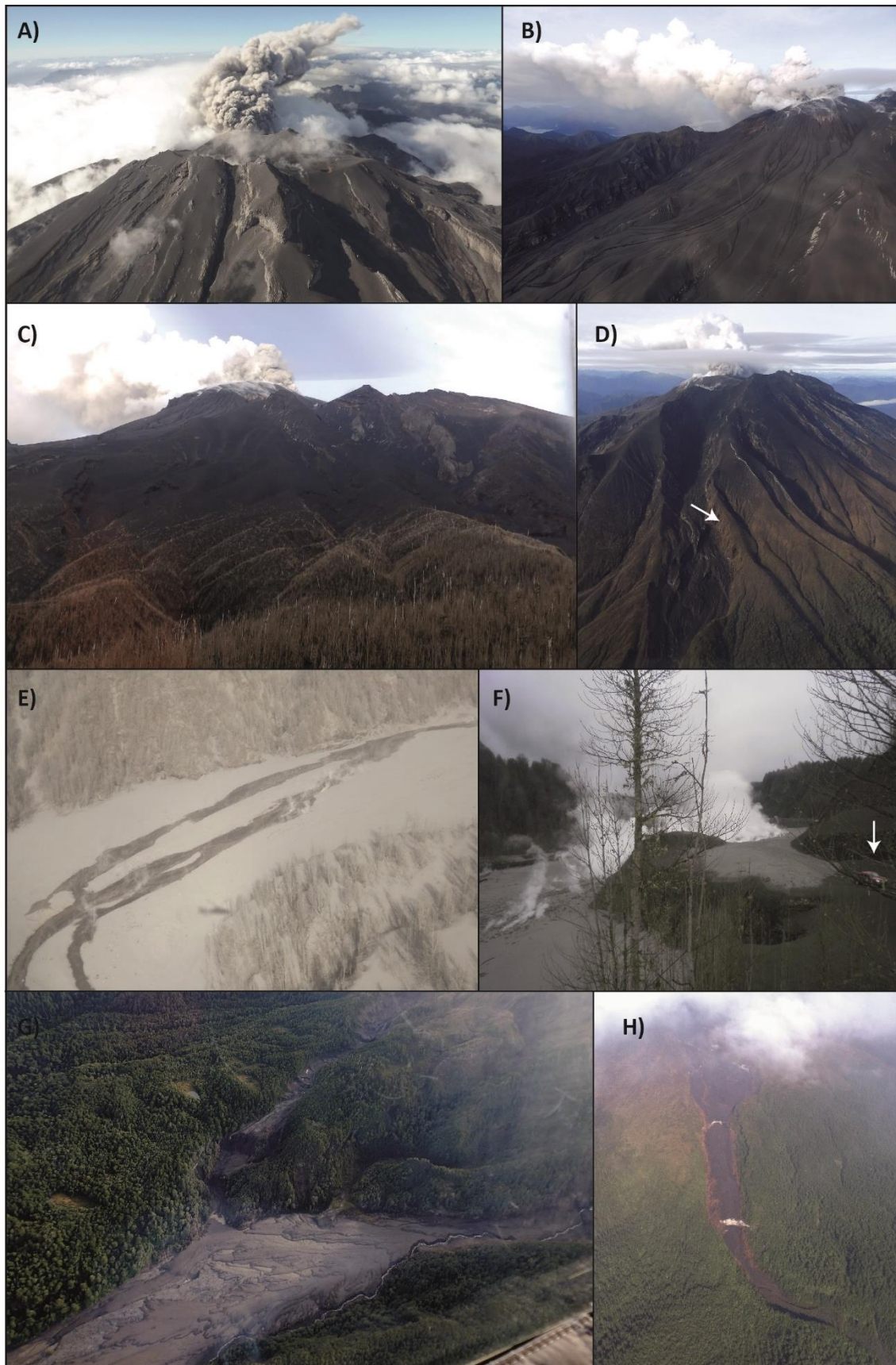


Figure 16. A) Proximal pyroclastic density current deposit in Rio Blanco and Rio Sur - Pescado rivers. At the end of the first pulse (Figure 10E and 10F) there was no ash deposited on the upper catchments of the Rio Blanco and Rio Sur - Pescado rivers. Therefore, we propose that the majority of this dark tephra is derived from the pyroclastic density current deposit emplaced during the 2nd pulse. B) Proximal deposit in NE flank.

*C) and D) Unconfined flow from north and northwest. Note the burnt forest (white arrow in D). E) and F) show dense pyroclastic density currents in Río Blanco Este.*



*Figure 17. A partially charred tree found in the Río Este valley, ~4.5 km downstream from the vent. Notice that the trunk is not completely burnt, with charring only on one side surface.*

The 2015 lahar modified the active river channel from the Río Sin Nombre towards the Río Este, likely due to sedimentation filling the Río Sin Nombre channel (which initially transported the lahar), causing the later part of the flow to erode a channel to the west to join the Río Este. Post eruption recovery works has cleared the sediment deposited in Río Sin Nombre using machinery and the active flow of water has returned to this channel (Figure 20C).



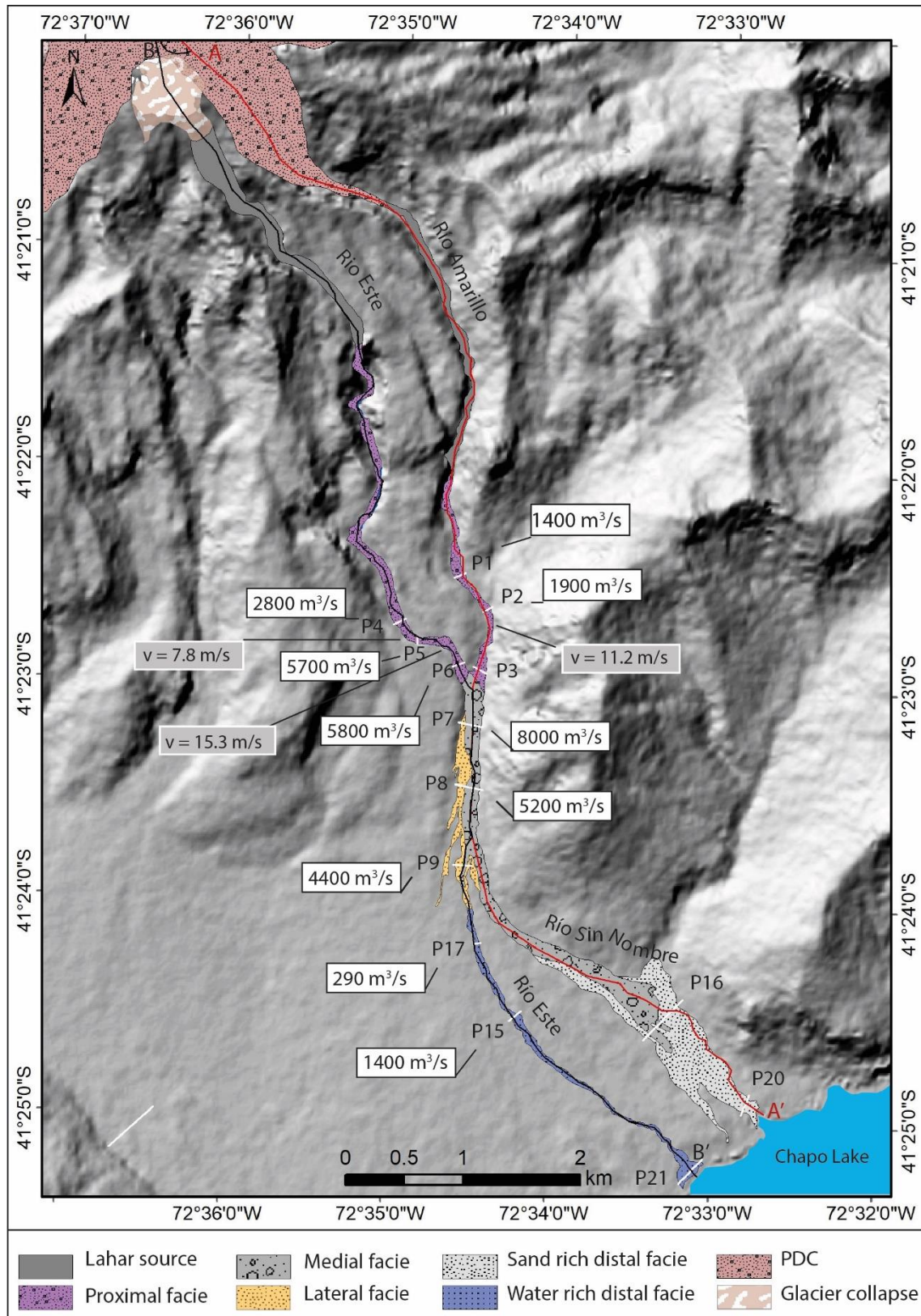


Figure 18. Map of facies of the lahar deposit and its source. Point estimates of discharge and speed (white squares and grey square, respectively) derived from field observation are shown. Discharge is estimated by the velocity-area method, using the differential GPS cross section method described in section 2.4.2 and speed is estimated using the Manning equation.

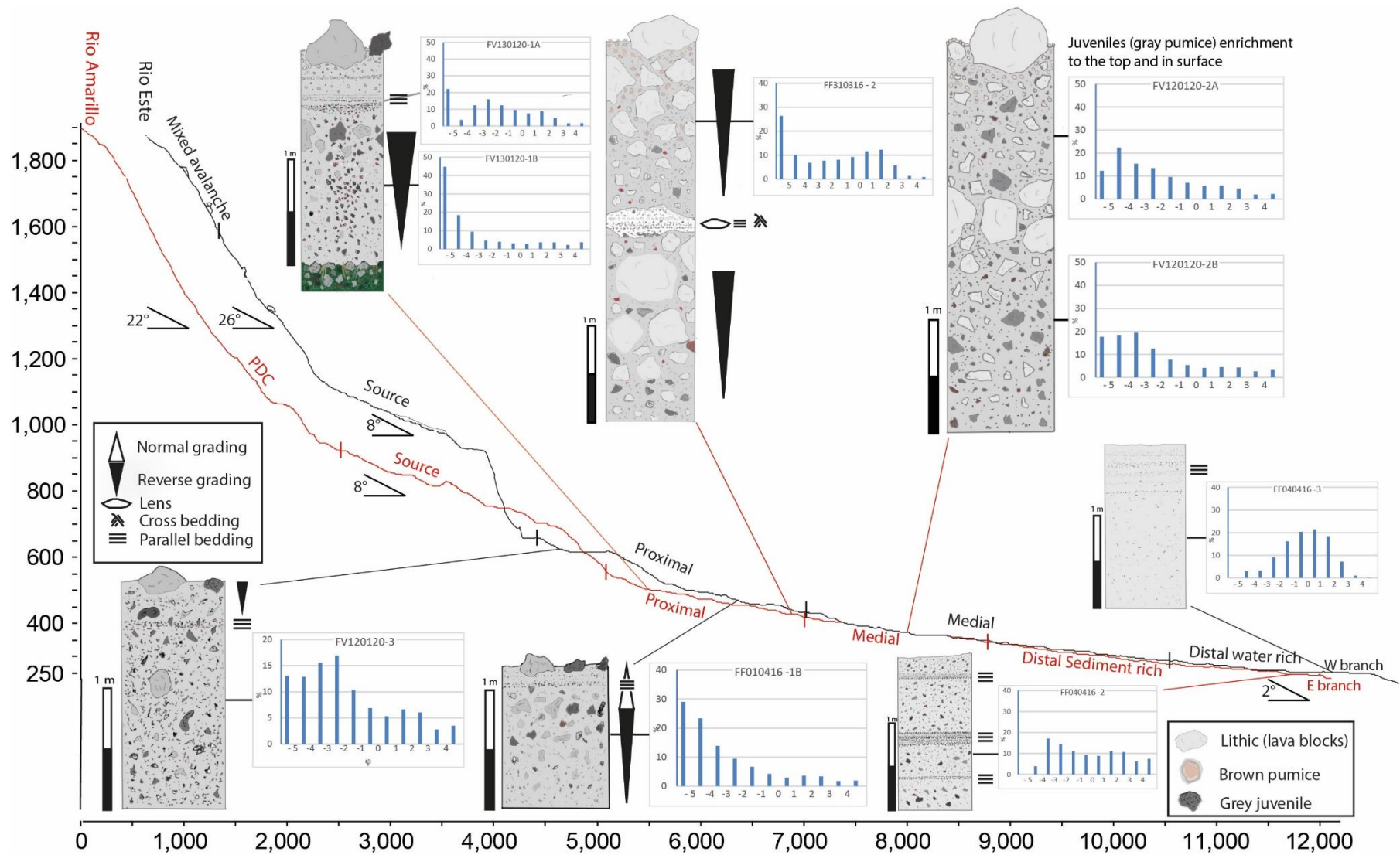


Figure 19. Summary of main sedimentary characteristics and grain sizes of the deposit along the lahar flow path in the Rio Este-Amarillo valley.



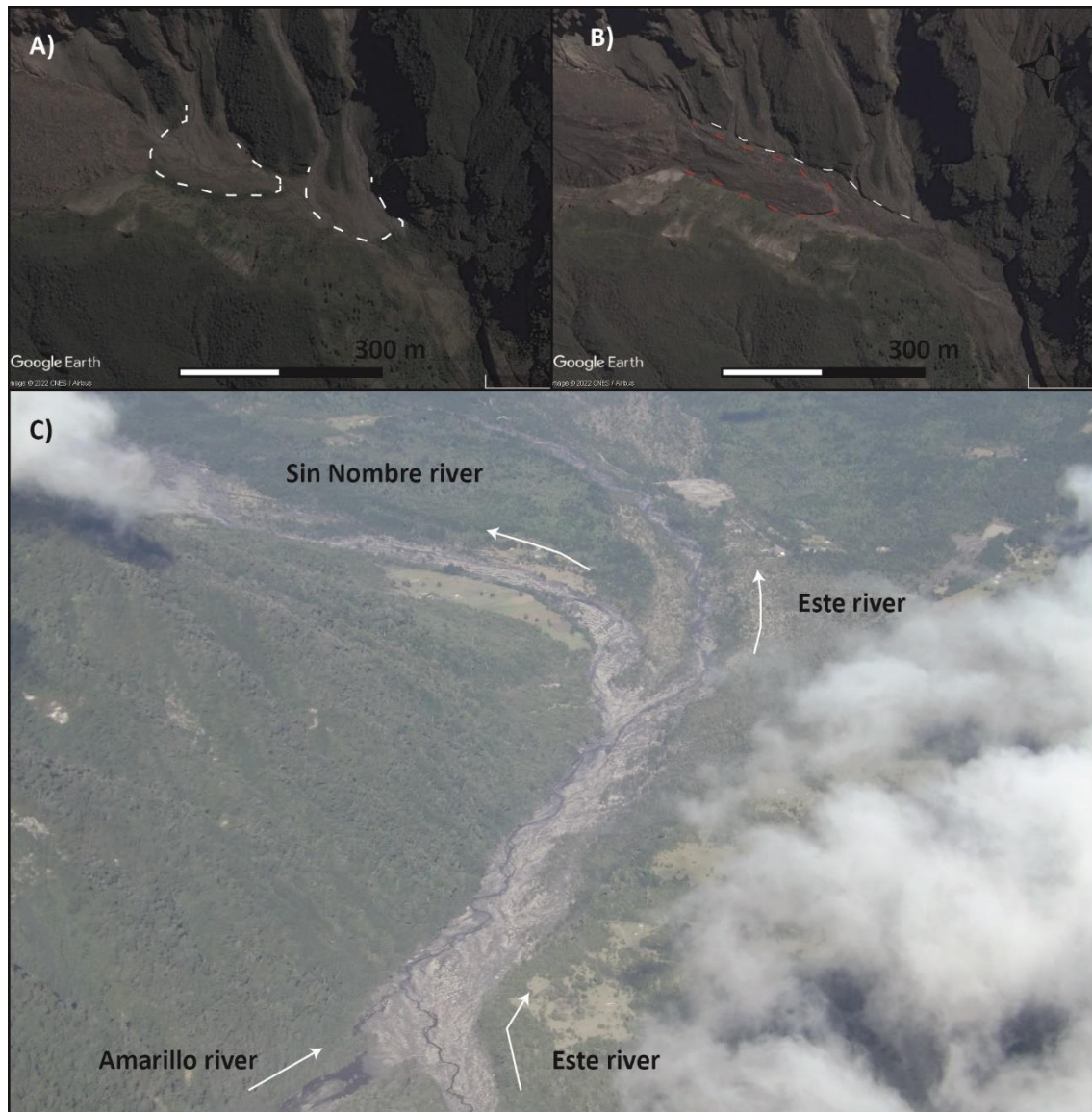


Figure 20. The Rio Este-Amarillo river system. A) and B) are views of the proximal area of Rio Amarillo taken in 2012 (pre-eruption) and 2016 (post eruption) respectively. In A) it is possible to distinguish two alluvial fans at the outlet of small streams towards the Amarillo river (white dashed lines). In B) the pyroclastic flow deposit (red dashed line) and an escarpment (white dashed line) in the fluvial and alluvial deposits are marked. We propose that the cut in the pre-eruptive alluvial deposits is due to erosion by lahars and the incorporation of non-volcanic sediment into the flow. C) Hydrology of the East River fluvial system, with the foreground corresponding to the upstream catchment, flowing towards Lago Chapo that is out of the image to the upper left. The two tributaries, Rio Amarillo and Rio Este, converge ~5 km from Lago Chapo, but bifurcate ~3km from their outlet. The eastern branch, Rio Sin Nombre, was the active flow channel prior to the eruption in 2015..



Figure 21. Post-eruption photographs of the confluence zone of the two tributaries of the Este-Amarillo fluvial system. A) Aerial image showing the Rio Este (left valley) and Rio Amarillo (right valley). The photograph is taken looking upstream. The red arrow indicates the mega block shown in panel B. Notice the alignment of blocks with the flow direction in the Rio Este. B) Photograph of a mega block found in the confluence zone ~ 4m size.

#### 2.5.3.4 Rio Este – Amarillo Lahars

Lahars in Este-Amarillo system were emplaced during the two main pulses of the eruption, likely with a major intensity during the second pulse, as shown in pictures and reports of the eruption (see section 2.5.2). In this valley, multiple lahars flowed with a sustained discharge during the first hours (with some discrete peaks). These flows were followed by a higher discharge flow, during the main paroxysmal second half of the eruption, consistent with a major column collapse reported during the second pulse (Castruccio et al., 2016; Van Eaton et al. 2016).

We estimate lahar speeds directly at three points. Two sites were measured using superelevation techniques, with speeds estimated to be 7.8 m/s in a location between cross sections P4 and P5,



and 11.2 m/s between P2 and P3 (Figure 18). At a third point, located between P5 and P6, we estimated the speed to be 15.3 m/s using the run-up method (Figure 18).

To complement these direct speed estimates, we have also estimated speed indirectly at locations where we measured channel cross-sections that provide estimates of the hydraulic radius. We then use the Manning equation (equation 4) to estimate the flow speed, for which we require a roughness coefficient for the channel, which is likely to vary along the flow path. We take a roughness coefficient of 0.08 in proximal areas, as the flow is here likely to contain a high concentration of solids and here are frequent bends in the channel path, both of which increase the resistance to motion. In distal areas the flow is likely to be more dilute, as inferred from observed deposits, but is also less strongly channel confined and may flow over terrain with vegetation cover, so we take a roughness coefficient of 0.05. As discussed previously, assumed values of the roughness coefficient introduce substantial uncertainties into the estimated flow speed of  $\pm 20$ –25%.

We measured 14 cross sections (Figure 18 and Table 4) from the proximal area to the distal depositional zones. The maximum discharge was estimated as 8000 m<sup>3</sup>/s in the beginning of the medial area. Estimation of discharge show a clear trend of rise from source and proximal area until the medial, where the peak occurs and then the flux gradually decreases until the distal zone, suggesting an erosive behaviour in the source and proximal zone changing to a more depositional regime in medial and distal area. Nevertheless, the west distal branch of Rio Este (Figure 19), exhibits an opposite behaviour, increasing the discharge in the downstream direction as shown by cross sections P17 and P15 (Figure 18 and Table 4) likely related to the high lateral and basal erosion of the bed observed in field (Figure 24). The maximum flow depths are reached in the Rio Este, in zones at the transition between the proximal and medial areas, with a measured depth of 7 m, although at the point with the narrowest channel cross-section in the proximal zone of Rio Este, the flow locally reached 10 m depth at a channel constriction of only 12 m width.

*Table 4. Summary of characteristics of lahars in Rio Este – Amarillo and Rio Blanco-Correntoso systems.*

Cross Section	Location	Main facie	Deposit area [m <sup>2</sup> ]	Flow inundated area [m <sup>2</sup> ]	Max. depth [m]	Hydraulic Radius	Terrain Slope [°]	Distance from source [km]	Speed (using Manning) [m/s]	Peak Discharge [m <sup>3</sup> /s]
P1	Amarillo river	Proximal	73	212	3	2.3	5.6	6	6.7	1400
P2	Amarillo river	Proximal	90	193	4	2.8	8.7	6.4	9.7	1900
P3	Amarillo river	Proximal	128					6.9	0.0	0
P4	Este river	Proximal	78	360	5.5	3.4	4.5	6	7.9	2800
P5	Este river	Proximal	80	344	7	5.1	11.7	6.3	16.7	5700
P6	Este river	Proximal	87	402	5	4.1	11.7	6.8	14.5	5800
P7	Este river	Medial	312	661	6.5	3.7	5.4	7.4	12.2	8000
P8	Este river	Medial-Lateral	248	657	5	3.8	2.2	7.9	8.0	5200



P9	Este river W	Medial-Lateral	244	493	4.5	3.6	3	8.7	9.0	4400
P17	Este river E	Distal water rich	14	50	2	1.4	3	9.4	5.8	290
P15	Este river W	Distal water rich	63	172	3	2.2	3.4	10.1	8.2	1400
P16	Este river E	Medial - distal sandy	209	n/d	n/d	n/d	n/d	10.9	n/d	n/d
P20	Este river E	Distal sandy	48	n/d	n/d	n/d	n/d	12	n/d	n/d
P21	Este river W	Distal water rich	77	n/d	n/d	n/d	n/d	12.1	n/d	n/d
P10	Blanco river	Source	147	441	5.4	3.7	5.8	0.5	9.5	4200
P11	Blanco river	Proximal	383	693	3	3.2	7.5	0.8	9.8	6800
P13	Blanco river	Proximal	677	1098	7.3	5.0	5.5	1.1	11.3	12400
P12	Blanco river	Proximal	25	47	1.6	1.2	4.82	1.3	4.2	200
P14	Blanco river	Proximal	242	401	6.5	5.3	8.1	1.5	14.2	5700
P18	Blanco river	Proximal	298	382	5.5	4.1	10.1	2.6	13.3	5100
P19	Blanco river	Medial	68	126	2.2	1.4	4.3	3.7	5.0	630
P22	Blanco river	Medial	162	243	3.4	2.6	3.9	4.1	7.1	1700
P26	Blanco river	Medial	142				2.2	4.3	0.0	0
P23	Blanco river	Distal sandy	106	189	4	3.4	3.4	9.1	7.8	1500
P24 W	Blanco river	Distal sandy	359	498	4.7	1.8	3.9	7.6	5.6	2800
P24 E	Blanco river	Distal sandy	133	223	2.5	1.1	2.2	7.6	2.9	650
P25	Blanco river	Distal sandy	24	62	4.5	2.7	2.8	9.7	6.1	380
P27	Overflow to Correntoso	Overflow	58	100	8	1.4	5.3	4.6	5.4	540
P28	Overflow to Correntoso	Overflow	14	n/d	n/d	n/d	5.2	6.5	0.0	0
P29	Overflow to Correntoso	Distal diluted	n/d	29	3.5	1.9	5.4	7.5	3.1	90

The lahar deposits are made up of a mixture of clay and silt, suggesting different sources of material or various pulses with different energies, and without a clear trend in the gravel-sand-mud proportion along the flow. Gravel size fractions are poorly sorted and consist of mostly sandy gravel and muddy sandy gravel, with some samples of gravel and one gravelly muddy sand (Figure 22). On the basis of the observed sedimentary and emplacement characteristics of deposits such as thickness, sedimentary structures, grain size distribution and planimetric geometry of deposit, we identified five different facies that evolve gradually from source to distal depositional areas. We denote these distinct facies as follows: (i) Source, (ii) Proximal, (iii) Medial, (iv) Lateral and (v) Distal Sandy and Distal Water-rich (Figure 18 and 19), with characteristics as follows.

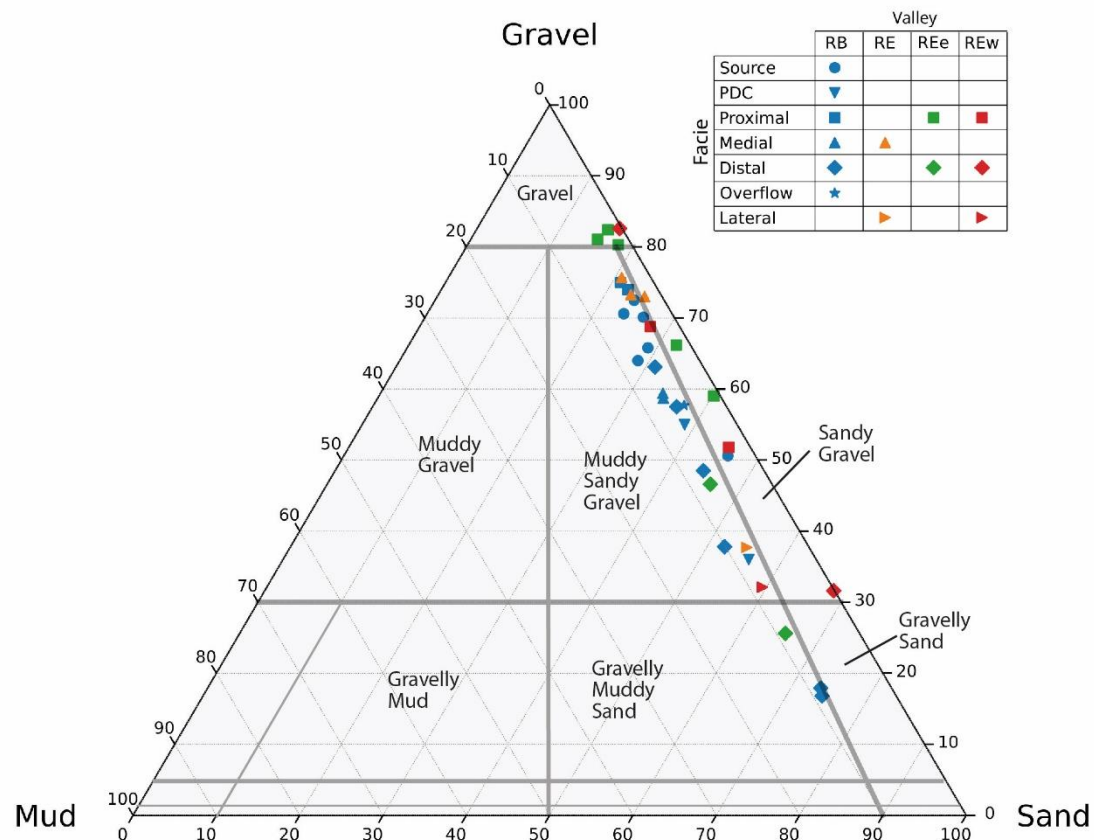


Figure 22. Ternary gravel-sand-mud plot of sample from deposit of 2015 lahar in Calbuco volcano. We distinguish the stream channel for each samples (RB – Rio Blanco; RE – Rio Este; REe – Rio Este distal eastern branch; REw – Rio Este distal western branch). Folk & Ward (1957)

The Source facies represent the transition between the deposits produced by the flow triggering processes and the deposits from a well–developed mixture of sediment and water characteristic of lahars. The triggering processes include pyroclastic flows interaction with glacial ice, and mixed avalanches of ice, tephra and rocks, that primarily contribute mass (solid and liquid) to the flow. These facies are in areas that are difficult to access, and we could not obtain samples or make direct field observations. A remote analysis from satellite images and photographs reveals that this area was highly eroded by flow where was emplaced alluvia, fluvial and volcanoclastic deposits; and older pyroclastic deposits and lava flow. Therefore the Source facies of the flow is predominantly erosive (Figure 20A,B).

The Proximal facies are not continuous and are interrupted by high slope morphologies of lava flows outcrops. Deposits are mainly on the channel beds, in a section inside older deposit terrace walls. The main sub-facies comprise deposits with 1.5--2 m depth, which are poorly sorted with a polymictic component, and are sand matrix supported (Figure 19 and 23). Large blocks with diameters up to ~50 cm are immersed in the deposit with a chaotic distribution but with a weak trend of being inversely graded and occasionally inverse-normal graded. Blocks are common on the deposit surface, and their proportion increases close to outcrops of lava flows, especially

where they are highly fractured, and the blocks can reach up to 3--4 m diameter (Figure 21) in the Rio Este. Rio Amarillo sample granulometry reveals these facies is notably poor in mud; all five samples had a mud content lower than 3%. Deposits in the Rio Amarillo show several sedimentary structures including inverse grading, parallel laminations, and coarse grain lenses towards the top. The deposits are polymictic with a high proportion of angular to subangular gravel fragments that are mainly volcanic clast (around 95%), but additionally there are granitic fragments inside (roughly 5%). In the proximal – medial transition, this unit has thicknesses in outcrops up to 4 m. Proximal deposits in the Rio Este are macroscopically similar to those in Rio Amarillo, although juvenile contents in Rio Este deposits are higher, and plotting samples from both streams in the gravel-sand-mud ternary plot, they fall in distinctive field of the classification ternary plot of Folk & Ward (1957) (Figure 22). In this proximal area, both in Rio Amarillo and Este, we find areas where a sandy facie locally covers older lateral terraces that are noticeably different to the deposits of the central channels. These features could be considered as a sub-facie of the main Proximal facie. Due the scale of the mapping used for this analysis, we neither map nor describe in detail this facie. These deposits have less than 50 cm thickness and blocks are absent or are erratic.

Deposits of the Medial Facies are continually present from the confluence of Rio Amarillo and Rio Este, until the dilution of the flow which occurs mainly in the Rio Sin Nombre, and to a lesser extent in the small overflow, until the beginning of the Rio Este branch in the distal zone of the valley (Figure 18 Figure 20). The deposits are 3-4 m thick and contain large amounts of blocks (Figure 21, Figure 23 and Figure 24). It is poorly-sorted, matrix-supported with a chaotic structure. There are two groups of clasts; the first are lithic clasts with subangular shapes, and a second family of juvenile sub-rounded clasts that are concentrated to the top of the deposit. Gravel and major clasts are composed of lava fragments and juveniles, with an approximate of proportion of 4:1, respectively, and with a marginal proportion of granitoids (<2%). Grading or sedimentary structures were not observed, except in a levee of mega blocks (<2 m) located at the initiation of the medial facies, where the Rio Este loses its confinement and joins with the Rio Amarillo.

The Lateral Flood Facies represent the lateral segregation of material from the main body of the flow, and is emplaced on the unconfined border of the medial facie, and in some locations on the border of the proximal facies, and gradually evolves from those facies. The deposits show an enrichment in juvenile lapilli fragments towards their top. The deposit thickness ranges from a few centimetres to roughly 1 m, and they are sand-rich, matrix-supported, and moderate to well sorted. We also observe different sedimentary structures such as parallel lamination, fine gravel lens, and incipient gradation, normal on the base of the deposit and inverse in the middle and top. Clasts are subangular, polymictic with gravel (pebble) sizes of 1 cm as their mode. Moreover, granitic and lava boulders are inside the deposit and over the surface, with sizes up to 1 – 1.5 m (Figure 23 Figure 24). Granulometry classifies the two samples of this facies as muddy sandy gravel, with a mud proportion of 7.5 – 8.3% in the matrix (Figure 22).

The Distal Sandy Facies are found downstream of the Medial Facies deposits. These facies

consist of sand-rich matrix-supported deposits (80% by volume of matrix approximately), exposed in a fluvial flood plain located at distance between 9 km and 12 km from the source. The deposits are unconfined to the west side where the flows inundated a large area of a gently sloping ( $<2^\circ$  slope) plain. Deposit thicknesses range from a few cm at the flow boundaries to  $\sim 1.5$  m in thicker areas, and the deposits buried almost completely some fences (Figure 24). Deposits show moderate to good sorting, and the clasts are polymictic, mainly subangular lava lithics. There is an enrichment of juvenile sub-rounded lapilli towards the top of the deposit. The deposit has normal grading of lithics and an incipient inverse grading of juveniles. Granulometry classifies these facies as muddy sandy gravel and gravelly muddy sand, with mud mass proportion between 7.4 and 8.9% (Figure 22).



Figure 23. Photographs at outcrop scale. A) A Proximal facies in Rio Este. Note the dark grey deposit and a columnar basalt block transported by the flow. B) A Proximal facies at Rio Amarillo with a gravel lens and imbricated clast. C) A Proximal facies before the transition to Medial facies. There are two main debris flow deposits, suggesting at least two pulses through the Amarillo valley. D) In the medial zone, 500 m



downstream of the image in panel C, there is an abrupt change from two distinctive units (panel C) to a more uniform and chaotic deposit (panel D). This suggests that a large pulse propagated down Rio Este and eroded earlier deposits that had formed from flows in Rio Amarillo. E) A Lateral facie deposit that is sandy and with an immersed block. F) A Distal sand-rich deposit.



Figure 24. Photographs of deposits in the Rio Este flood plain. A) A Medial facie deposit with lots of blocks on the surface and immersed in a sandy matrix. B) A sandy Distal deposit complete flooded a field .Note the buried fence and the decrease in the proportion of mega blocks on the surface of the deposit..

Finally, the Distal Water-rich Facies are mainly erosive, so deposits are not abundant and are mostly composed of matrix boulders, blocks, and trunks within or on top of a poorly sorted matrix. The deposits are clast-supported, with evidence of intense erosion of both the bed and lateral walls of the older terrace that forms the terrain. Some road-cuts show incision of 2-3 m depths (Figure 25). A noticeable characteristic of this facies is that samples have very low percentage



(0.1—0.3%) of mud which is in dramatic contrast with distal facies in Rio Sin Nombre (Sandy distal facie) and distal facies in Rio Blanco.



Figure 25. Photographs of a Distal water rich deposit facie in the Rio Este. A) Photograph looking along the channel from the source. The flow has eroded through section of older volcanoclastic non-consolidated deposits, with a channel width of 40 m. B) A photograph of a road cut by the flow. The erosion depth is approximately 1.5 m. C) Flow marks left by the 2015 lahar on the older terrace wall. At this point the flow mark is 2.5 m above the bed.

The total area covered by lahars over the whole eruption was  $1.8 \times 10^6 \text{ m}^2$ , and the transported material left a deposit with a total subaerial volume of  $1.6 \times 10^6 \text{ m}^3$ . Assuming a mean solid concentration of 60% of the volume, which is a typical value for sediment concentration in the transition between debris and hypercontracted flow (Thouret et al, 2020), we obtain a total volume of flow to be around  $2.7 \times 10^6 \text{ m}^3$ . Nevertheless, the facies recognized in the deposits of this lahar suggest the occurrence of different flow types. Specifically, the proximal and middle facies show characteristics common to debris flows such as poor sorting, absence of laminations, normal and/or reverse gradations, randomly oriented clasts (except at flow margins), high degree of compaction (Costa 1988, Pierson et al., 2009), while the distal facies exhibit characteristics of hyperconcentrated flows such as parallel lamination, moderate sorting, lenses, among others (Costa 1988, Pierson et al. 2009). Therefore, it is reasonable to infer that some flow phases contain a proportion of solids in the range between 20 and 60 vol%, as proposed for hyperconcentrated flows (Thouret et a. 2020). For comparison, if we assume an average solids concentration for the entire flow of 40%, the volume of the flow is  $4 \times 10^6 \text{ m}^3$ .

#### 2.5.3.5 Rio Blanco – Correntoso fluvial system

Similar to the Rio Este-Amarillo, the Rio Blanco-Correntoso fluvial system is a basin fed by rainfall, snow and glacier melt that drains the volcano to the south. Rio Blanco discharges into Chapo lake whereas Rio Correntoso is a tributary of Rio Chamiza (see Figure 1Figure 26). The upper part of the basin is within the collapse amphitheater rim of the volcano and drains to the south where the amphitheater is open and a hanging glacier is emplaced (Figure 8). On the exterior border of the amphitheater, the valley is confined by a glacier circus morphology which extends and evolves to a ~1km wide, steep-walled, glacial valley filled by post-glacial volcanic deposits, with both lava flows and pyroclastic material. This volcanic sediment is an abundant source of material for lahars, in addition to large lava blocks from fractured lava fronts and pre-glacial lava flows on the valley walls. The main glacier morphology reaches 6 km downstream, where the valley opens to a large depositional area built by superposition of fluvial streams, alluvial fans and flood plains. In this distal area, approximately at 8 km from the volcano summit, the 2015 lahars overtopped the Rio Blanco channel and flowed into a paleo-channel that drains to the Rio Correntoso, whose source is at the western boundary of the valley, fed from groundwater (Figure 1, Figure 7A, Figure 8, Figure 26).

The pyroclastic flow in the Rio Blanco left an extraordinary lobate deposit that extends up to 4.3 km, covering an area of  $1.4 \text{ km}^2$  with a total volume estimated as  $1.8 \times 10^6 \text{ m}^3$ . The deposit exhibits a notable segregation of clasts on the surface and to the front and lateral borders and pronounced lobes with an enrichment of volcanic bombs (scorias) that show a clast supported arrangement and cauliflower morphology (Figure 27A and C). At location FFVC29, the core and main body of the deposit has a thickness between 2.5 – 3.5 m and is formed mostly by only one indistinct unit or facies which is poorly-sorted with an ash matrix (30% volume), mainly juvenile clasts with subangular to subrounded shapes and subangular lithics. There are two families of juveniles, one

with pumiceous appearance and light brown in colour up to ~1 cm size, and a second group with denser dark-grey scoria reaching ~ 30 cm in size. In this place and upstream the deposit contain lava blocks immerse in the surface. At FFVC31, near the deposit front, we recognize the thicker deposit in the area, with a thickness up to 5 m, in a deposit emplaced directly over an older lava flow (Figure 28D). A stratified deposit was recognized here, with at least 4 units, distinguished by the presence of bomb-rich levels, others with lapilli laminations and some changes in coloration (this outcrop was not described in detail given the scope of this work and access limitations). In this deposit, the prismatically jointed blocks recognized by Castruccio et al. (2016) in a basal unit (Unit C) of the pyroclastic flow deposit on the northeastern flank of the volcano were not recognized, and given some similarities, such as the presence of bombs with cauliflower morphologies, and a lobate roof it is likely that the pyroclastic deposits in the Blanco River can be correlated with Units D to I presented in Castruccio et al. (2016) for the northeastern deposit.

A lahar in the Blanco-Correntoso River system occurred during the second pulse and was likely triggered by mechanical collapse of the glacier that released water suddenly forming a flow that evolved to a lahar.

We measured 16 cross sections (Figure 26 and Table 4) from the proximal to distal depositional zones. At the source, in cross section P10, the peak discharge is estimated to be 4200 m<sup>3</sup>/s, and approximately 1 km downstream at cross section P13 the peak discharge along the flow was estimated as 12400 m<sup>3</sup>/s. This last value is anomalous in comparison with the measurement ~300 m upstream at P11 (6800 m<sup>3</sup>/s) and the measurement ~500 m downstream at P14 (5700 m<sup>3</sup>/s) and therefore the discharge at P13 is likely an overestimate. Nevertheless, flow marks and pre- and post-eruption images show clearly features that indicate that the flow is highly erosive in the source area in the vicinity of P10, and we cannot discount an extreme bulking process in this area that dramatically increases the discharge, followed by rapid deposition or arrest of material downstream. The flow dynamics in this region is likely to be significantly affected by a 200 m wide and 15--20 m high waterfall between P10 and P13, that is not only a substantial vertical drop in the topography, but also demarcates a transition between the highly erodible area upstream and the first large depositional zone for the lahar downstream of the waterfall. The discharge remains high for the first ~3 km of the lahar propagation from the source, and cross-sections in the proximal regions exhibit ratios of deposit area to flow area in the range 0.2-0.3, that indicate that the peak cross-sectional area of the flow passing through these sections is 3 to 5 times larger than the cross-sectional area of the deposits left by the flow.

The maximum depth of flow is reached in the overflow area where the lahar follows a stream from the Rio Blanco towards the Rio Correntoso. At the beginning of this secondary stream there is a topographic drop that could explain the high flow height at this distance from source. Along the Rio Blanco mainstream, the maximum height of flow is estimated to be in the range 5--7 m in the proximal area.



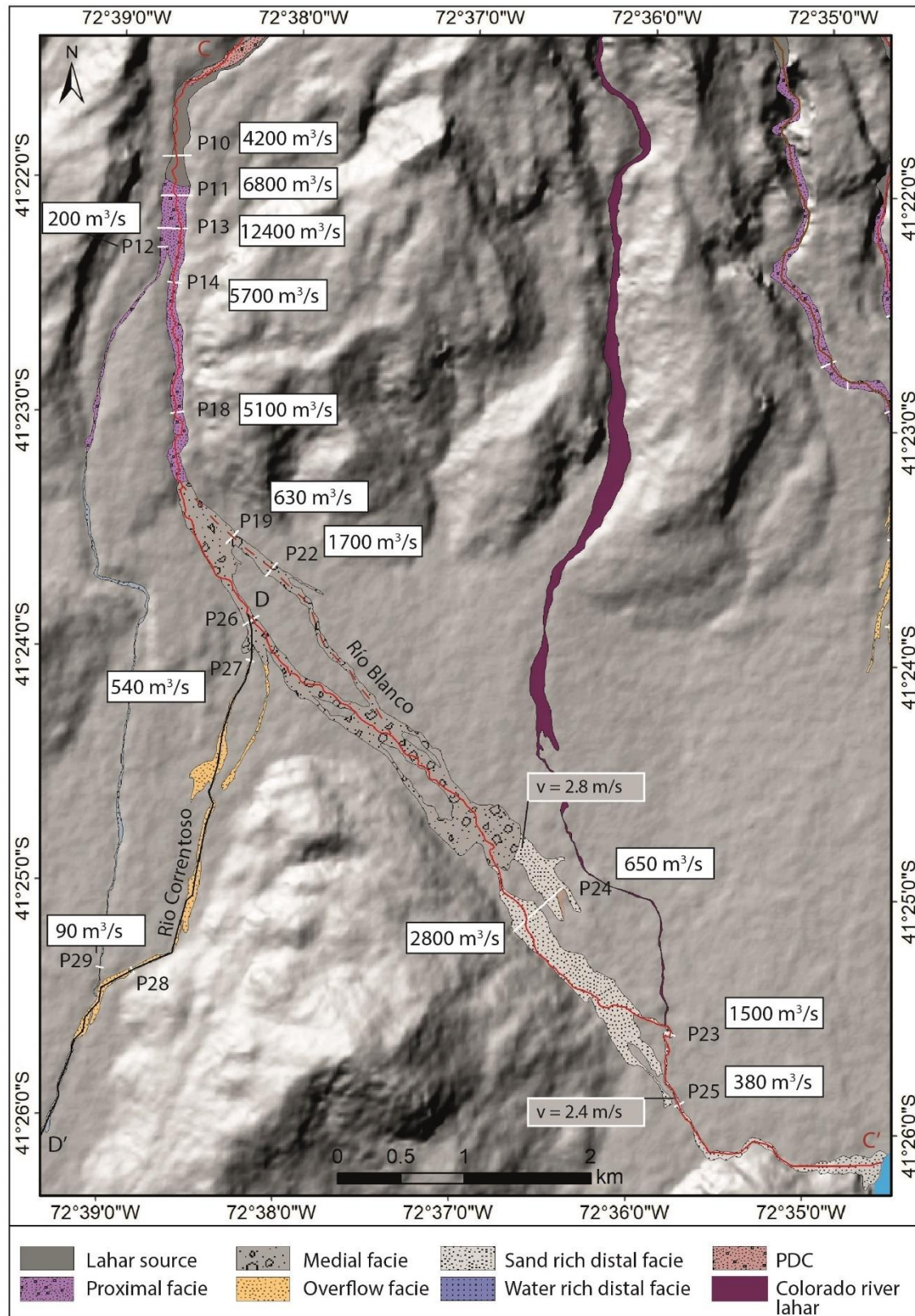


Figure 26. Map of facies of the lahar deposit in Rio Blanco – Correntoso and its source. Locations at which cross-sections are measured are indicated, along with estimates of the peak discharge and flow speeds at some locations.



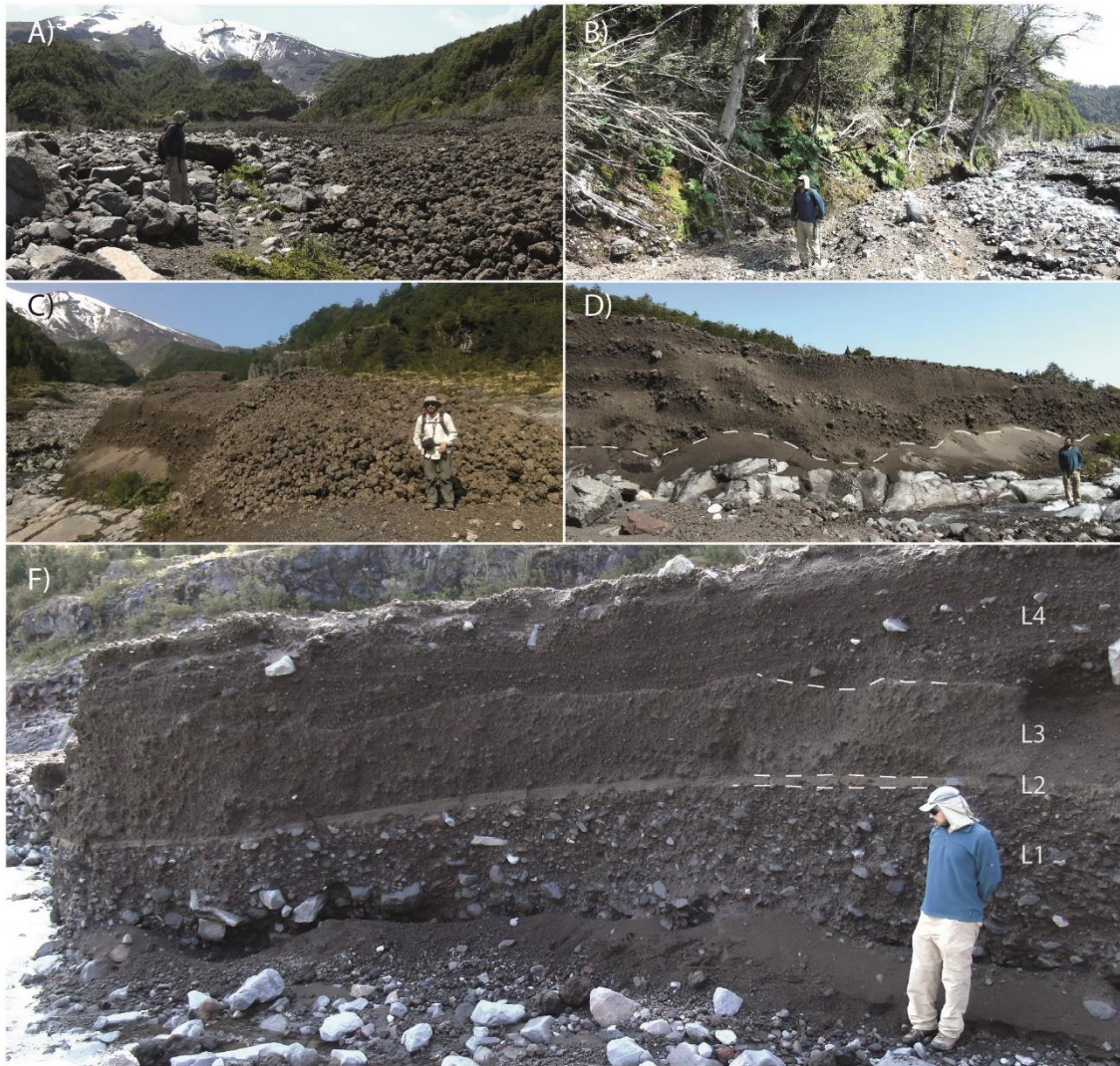


Figure 27. Photographs of the pyroclastic density currents and the lahar transition area. A) Contact of Pyroclastic flow deposit (to the right) and the bed of the Rio Blanco. B) Flow mark in a tree (white arrow) and branches oriented in the direction of flow. Flow mark reach 4 m from bed. C) Front of a clast-supported lobe rich in bombs. D) PDC deposit emplaced over a lava flow. E) Section of pyroclastic and volcanoclastic deposit in the PDC-lahar transition area.

Speeds were estimated at two distal points using the run-up equation (equation 2), with values of 2.8 m/s and 2.4 m/s. In addition, we used Manning's equation (equation 4) for speed calculations based on hydraulic radius measured at cross-sections., using a roughness coefficient that varies along the channel. We use a roughness coefficient of 0.08 in proximal areas where a high solid concentration is assumed and the lahar propagates over a smooth lava flow and the valley remains roughly straight. In distal areas we find a value of 0.15 is required to produce speeds that are comparable to those estimated using run-up., While the lahar is expected to be significantly diluted in the distal areas, as inferred from the deposits here, the flow also carries a high proportion of anthropogenic rubble and trunks, and the channel is within dense forest areas so

overbank flow is substantially retarded. Therefore, the high roughness coefficient is consistent with the ground cover and flow characteristics in the distal channel.

Grain sizes of lahar deposit samples follow a clear trend along the flow in the gravel-sand-mud (clay+silt) proportion (Figure 22), suggesting a unique main source of material. Almost all the samples taken in the source and proximal areas are in the muddy sandy gravel field in the gravel-sand-mud ternary plot (Figure 22), whereas distal samples are gravelly muddy sands and slightly gravelly muddy sand. A preliminary componentry analysis revealed an increase in lithic proportion from the source until the proximal – medial zone transition, and then a decrease in lithics and an enrichment in juvenile components from the medial to the distal zone, suggesting that source and proximal zones are in net terms erosive, while in medial and distal zones deposition is predominant.

On the basis of sedimentary and emplacement characteristics of deposits, including their thickness, appearance of sedimentary structures, the grain size distribution and planimetric geometry of deposit, we identify six different facies that evolve gradually from the source to distal depositional areas. We define these facies of flow as follow: (i) Source, (ii) Proximal, (iii) Medial, (iv) Overflow (v) Distal water rich and (vi) distal sediment rich (Figure 26Figure 28). Figure 26 illustrates some characteristics of the different facies and Figure 29 shows photographs of these from the field.

The source facie of the deposits in Rio Blanco exhibits isolated outcrops with few continuities, supporting the idea that this is an erosive area. In two sections it is possible to distinguish at least 3 different stratigraphic levels. The basal level is formed by a sandy-matrix “chaotic deposit”. The middle level is a juveniles- and bombs-rich deposit in a dark grey ash matrix. At the top there is a sand-rich deposit with some sedimentary flow structures such as parallel laminations and lenses. In an outcrop located a few tens of meters downstream of the front of the PDC deposit (Figure 27F) some noticeable characteristics are present. First, the contact between the basal “debris flow” type deposit (L1 in Figure 27F) and the “dense PDC” type deposit (L3 in Figure 27F) is a 8-10 cm layer of a well sorted deposit of fine ash and mud. Additionally, the contact between the central PDC deposit (L3) and the overtopping sandy deposit (L4) is irregular, but L4 does not seem incorporate material from L3, and the contact exhibits some convolute structures, like those observed in deposits of mixtures of two flows with different densities, such as turbidites (Gladston et al. 2017), and attributed to soft deformation (Douillet et al. 2015)

In other scattered outcrops downstream, the deposits are composed of one single stratigraphic unit with 1 to 1.5 m depth, that are poorly sorted, with polymictic component, sand matrix supported, and with roughly 20-30% of matrix by volume. Deposits have a few large blocks on their surface, up to ~50cm diameter, that are slightly inverse graded and occasionally exhibit parallel lamination by size and a lens of coarse granulometry.

After emplacement, the lahar covered an area of  $2.25 \times 10^6 \text{ m}^2$ , the transported material left a deposit with a total subaerial volume of  $2.6 \times 10^6 \text{ m}^3$  and subaqueous volume of  $0.4 \times 10^6 \text{ m}^3$ ,

which allows us to estimate a volume in the range between  $5.0 \times 10^6 \text{ m}^3$  and  $7.0 \times 10^6 \text{ m}^3$ , assuming an average solids concentration for the whole flow between 40 and 60 vol%, which is a typical value for the sediment concentration for hyperconcentrated flow and the transition between debris flow and hypercontracted flow regimes (Thouret et al. 2020), which are facies recognized in the deposits of this lahar.

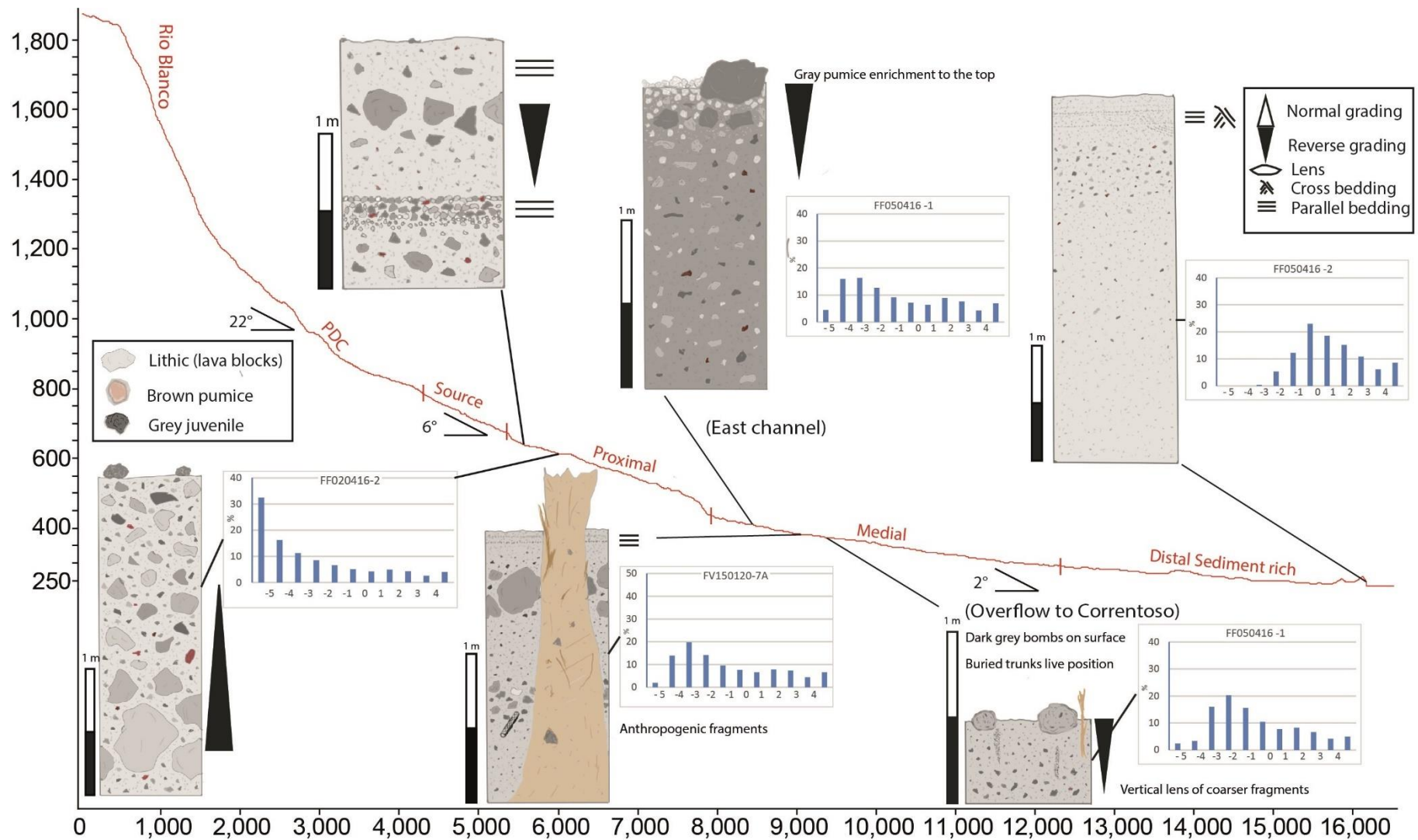


Figure 28. Summary of main sedimentary characteristics and grain sizes of the deposit along the lahar flowpath in rio Este-Amarillo valley





Figure 29. Photograph of the different areas of Rio Blanco – Correntoso lahar. White arrows on the photographs illustrate the flow direction. A) View of the PDC front and its transition to a lahar. B) and C) Medial facies diverge in two channels, cutting a forest area. D) Medial – Distal area where the flow loses confinement and floods Rio Blanco village. E) Overflow facies, with a large number of trunks in the flow. F) Fisheries facilities destroyed by the overflow facies of the flow



## 2.6 Discussion

### 2.6.1 Methods

In this study, we have made use of non-official sources of information (crowdsourced images or citizens monitoring) and have demonstrated that they are a useful tool to identify different stages of volcanic activity during the Calbuco eruption. As online platforms provide rapid and easy access to information of this kind, it may in some cases be a valuable source of information for eruption monitoring during a crisis. However, we strongly recommend that protocols are developed to provide a systematic approach to capturing in near real-time this information for use in crisis management. Without a systematic method to analyse data, a strong knowledge of the researcher about the study area — in geographic, cultural, and political dimensions — there is a strong possibility that misleading and imprecise information could be gathered that could lead to poor interpretation and potentially bad decision making.

We have gathered substantial quantitative data from our field studies and have used these together with geological characterization of deposits to develop an understanding of the initiation and development of volcanic flows during the 2015 eruption. Like all quantitative measurements, our data are subject to uncertainties. Our estimates of the physical characteristics of the lahars, such as flow volume, velocity, and flow rates (or discharges), have been based on indirect methods (e.g. Pierson 1985), which introduce epistemic uncertainties that are often difficult to quantify.

The cross-section surveys are one of the most important data sets used in our analysis, contributing to estimates of the volume, discharge, and speeds of the flows and the depth of the deposits. Therefore, estimates of the magnitude of measurement error for the cross-sections are necessary to assess errors in the derived quantities. These surveys were made one year after the eruption, which is sufficient time for the rivers to incise through the fresh deposits to provide access to the stratigraphy, but the deposits are still fresh enough to facilitate detail analysis and interpretation without e.g. the development of vegetation, weathering or other post-emplacement processes that alter the deposit structure. Most of the cross-sections were made using differential GPS with less than  $\pm 0.5$  m of error in both the vertical and horizontal. This uncertainty is considerably smaller than the uncertainty in wide-area digital elevation models, but we still have substantial measurement errors, estimated to be of the order of 20%. However, a greater source of error in the measurement of cross-sections is to be due to the epistemic uncertainty on the geometry of older terrace structures and the unexposed topography under the lahar deposit.

Regarding the volume estimation, as discussed by Muñoz-Salinas et al. (2009) it is not possible to obtain a high level of accuracy in the estimation of lahar deposits volume because of intrinsic instrumental errors (e.g., precisions of GNSS data) and the incomplete and imperfect identification of the deposit and its demarcation. In this study, these problems are noted in inferring the contact surface between older channel bed and fresh deposits when measuring cross sections, where the contact is only visible in channels incisions and at the deposit margins. Moreover, it is difficult to distinguish

between different events or pulses of flow in a very dynamic volcano-fluvial environment. Despite these challenges and considering that some of the cross-section surveys could be made only with basic hand tools, this method is a simple and low-cost technique to derive an estimate of the lahar volume, especially when appropriate pre- and post-eruption digital elevation models are not available from which to obtain deposit volumes by differencing (Williams 2012). The accuracy of this technique is directly related to the number of cross sections measured. It is important to collect sufficient cross-sections to capture the variation in the deposit footprint, which also requires a consideration of appropriate locations. In particular, at least two cross-sections should be taken for each domain or facie of the deposit.

Additionally, field observations also have an interpretative bias, e.g. a lahar deposit could be mistaken for a fluvial deposit (Orton, 1996), and at the same time, the exposure of the deposits and flow marks is limited, and they are exposed to erosion or reworking.

## 2.6.2 Lahar flow transport, triggering mechanisms and dynamics

Lahars in Rio Blanco and Rio Este were triggered by the melting of glacial ice in the catchment area of the basins due the interaction of the glacier and volcanic processes. Despite the similarities in the triggering mechanism and the geometry and major sedimentary features of the deposits of both lahars, there are differences in their dynamics and transport.

While both Rio Blanco-Correntoso and Rio Este-Amarillo, had their peak flow discharge during the second pulse of explosive activity, with the major collapse of the eruption column, the lahar in Rio Amarillo began earlier than those of Rio Este and Rio Blanco-Correntoso, during the early stage of the first explosive pulse. This early flow mobilized fresh pyroclasts and existing materials and produced new deposits along its path altering the topography of the channels and contributed material that could be remobilized by entrainment into the later lahars triggered during the peak pulse of activity.

The components in lahar deposits in all the valleys that we analysed are polymictic, but in Rio Blanco the deposit, in general, exhibits more lapilli juveniles (dark grey and light brown lapilli) and more bombs on the surface. This suggest the major importance of a primary source of sediment from PDCs in Rio Blanco, whereas in Rio Este, the contribution of eroded material, including fresh pyroclastic fall and flow deposits and pre-existing fluvial, glacial, and pyroclastic sediments, from riverbeds and the volcano slope is more relevant.

There are some field observations of deposits that could be interpreted as emplacement structures influenced by flow dynamics. However, we must be cautious in interpreting flow conditions from deposits, as the deposit captures information on depositional processes and the flow at the time of deposition. In particular, lenses of gravel could represent a water unsaturated media in the flow or in the other way, an excess of solids origin by Infiltration of water, vapour escape or mechanical sieving (Vallance, 2000), which suggest that a granular rheology and a water-saturated facie rheology coexist and are transitional.

Other interpretations associated with post-depositional processes could validly explain the occurrence of lenses in the deposits, such as a selective erosion of fine interstitial sediment or the entrainment of fine sediment by the escape of fluids from the base to the surface due to a positive pore pressure (Pacheco – Hoyos et al. 2020). However, on the basis of the geometry of the pores, which are generally elongated in the horizontal direction, their arrangement in the massive centre of the deposit rather than at the base or top of the deposit, and the absence of fine deposits that could correspond to the matrix removed in the gravel-rich lenses, we propose that these structures would have been formed from the transport conditions of the lahar.

A noticeable behaviour occurred in the paleo stream of Rio Este, in the distal zone (section 2.5.3.3, Figure 18 and Figure 20). Here, anomalously large amounts of erosion for this reach of the river opens a wide channel on the older volcanoclastic flood plain, taking material from the bed (basal erosion) and terrace (lateral erosion). There is a remarkable difference with the Sin Nombre stream, that is parallel to this channel and as a similar geomorphological context. One explanation for this extreme erosive behaviour could be the fall in the Chapo lake level over recent decades, when this channel was inactive and thus has not had persistent streamflow morphodynamic processes to equilibrate its thalweg to the new hydraulic gradient. Moreover, grain size samples in Rio Este reveal a heterogenous mud content that could suggest significant contributions of bed sediment to the solid mass rather than primary fragmented tephra. In contrast, the gravel-sand-mud proportion in Rio Blanco changes with a clear trend along the flow path, suggesting a unique main source of solid material in the flow (Figure 22).

### 2.6.3 Conceptual model of 2015 volcanic flows

Our observations show a complex interaction of processes during the 2015 eruption. By combining syn-eruptive observation and post-eruption field work, and our results allow us to propose a new conceptual model and chronology of the volcanic flows that occurred during the 2015 eruption in the Blanco-Correntoso and Rio Este-Amarillo basins. We identify five main stages (times in UTC):

**Stage 1** (21:06 – 22:00, 22 April): No anomalous activity in Rio Blanco drainage. Pyroclastic flow descends toward Rio Este and intensely interacts with the glacier triggering the first pulses of lahars.

**Stage 2** (22:00 – 22:30, 22 April): Pyroclastic material begins to be remobilised toward Rio Blanco due to intense deposition of ash and ballistic pyroclasts in the upper area of the basin, increasing the discharge and solid load in the active river. The flow remains confined to the channel, bridges remain intact, and no roads are cut. In Rio Este, PDCs continue to be emplaced in the catchment area of the watershed, generating melt water from the glacial ice and contributing sediment of primary pyroclastic origin into the river system (Figure 10).

**Stage 3** (~06:00, 23 April): A change in eruptive conditions triggers a its major column collapse, producing large pyroclastic flows that descend radially and cover the main valleys of Calbuco (section 2.5.3.1 and Figure 13 to 15). PDCs cover the glacier and cause collapses of the ice due to both thermal

and mechanical stresses by burying ice with hot pyroclastic material and filling crevasses and fractures on the glacial surface.

The large failure scar is at the head of Rio Este basin, and likely triggered by mixed avalanches (e.g. Breard et al. 2020) rich in water, which transport mega ice blocks that are deposited some tens of meters down the slope.

In Rio Blanco a similar mechanism is likely to have occurred. A major collapse of ice is likely to have triggered a mixed avalanche that flowed downslope and evolved into a debris. This formed a multiphase flow with some juveniles-rich phases (interpreted as PDCs) and different types of water-sediment mixed flows occurring simultaneously, as suggested by the sections of Figure 27F. This mixing is represented in the source facie of the lahar in Rio Blanco as described in section 2.5.3.5.

**Stage 4** (08:00 – 10:15, 23 April): The last stage of volcanic activity triggered a PDC that was emplaced over the previous flow which had not completed arrested and contained a high content of trapped water that could be released from a permeable phase to the surface and incorporated into the PDC by two mechanism: (1) evaporation and (2) increase of pore pressure due to the mechanical load of the overflowing late-stage PDC and by hydrodynamic pressure in the still moving material.

The hypothesis of vapour-water trapped under the PDC is supported by observations of the radially symmetric pipe in the PDC deposit (section 2.5.3.1), and the fine layer recognized between the basal debris flow type deposit and the PDC deposit (Figure 27F) that could be interpreted as fine sediment transport by an upward flow of water.

**Stage 5** (hours – days post eruption): This is a late stage of flow. Some late collapse of the column emplaced new PDCs on the upper basin of the Rio Blanco that formed a highly lobulated surface. These cover the previous deposit from the mixed avalanche, proximal lahar and prior PDCs.

In the distal Rio Este basin, the Rio Sin Nombre stream filled the channel and the water-rich tail of the lahar “jumped” to the paleo stream of Rio Este (Figure 20). This channel was prior to the eruption and the flow intensely eroded the terrace and opened a wide channel before reaching its outlet in the Chapo Lake, although this process likely began during the stage 3 or 4.

## 3 Modelling primary lahars from the 2015 eruption of Calbuco

### 3.1 Introduction: Modelling lahars

Understanding volcanic processes and their interactions requires the combined use of different approaches and techniques ranging from field observations and measurements, laboratory analysis, remote sensing, and the development and application of models. Each approach used separately has its limitation and weakness. For instance, volcanic flow deposits are not well preserved in active fluvial systems or under extreme climatic conditions, and drainage network are dynamic environments that are sensitive to volcanic eruptions (Pierson & Major, 2014). Therefore, mapping hazard zones only based on the recognition of past events and incomplete geological records could lead in a misinterpretation of the phenomena. Modelling volcanic flows can provide further insight into flow dynamics and their consequences and are therefore an essential complement to field studies (Fagents, Gregg & Lopes, 2013).

There are many types of models used in volcanology, including analogue or experimental models (Kavanagh, Engwell & Martin, 2018), empirical models (e.g., Iverson, Schilling & Vallance, 1998), statistical models (e.g., Rougier et al., 2018), and deterministic physical models (discussed further below). Despite the rapid improvements over the last decades in modelling volcanic processes, the link between models and well-documented real cases is essential, providing an opportunity to test model predictions, constrain their uncertainty, and validate their use in critical applications such as predicting volcanic hazards and informing mitigation measures, as well as contributing to the interpretation of volcanic events and their deposits. Thus, helped by the progress in computing routines and infrastructure for their implementation, as well as availability of necessary input data (e.g., more affordable acquisition of high-resolution Digital Elevation Model (DEM)), numerical simulations of volcanic hazard, such as pyroclastic flows, lava flows, lahars, and tephra fall, have become an indispensable tool in hazard assessment (Kavanagh, Engwell & Martin, 2018).

#### 3.1.1 Models of lahars

From a fluid mechanical perspective, lahars are commonly an unsteady, multiphase flow, which are triggered by a release of a water-sediment mixture from one or multiple sources (Manville, Major & Fagents, 2013; Vallance & Iverson, 2015; Thouret et al. 2020). Field observations indicate the highly non-uniform character of the sediment load in lahars, with large variation in solid concentration and evolving grains size distributions (Vallance & Iverson, 2015). In part, this variation on solids is due to segregation of material in the flows, which can develop distinctive front, body, tail and lateral zones (Manville, Major & Fagents, 2013). This wide variation in solids content suggests that flow dynamics cannot be described by a single fixed rheology (Iverson, 1997; Manville, Major & Fagents, 2013), and

thus modelling lahars is challenging and several models have been proposed (a brief summary of notable models is given below).

Likely the most widely used model for lahars is LAHARZ (Iverson, Schilling & Vallance, 1998) a semi-empirical model, which combines a scaling relationship calibrated using statistical analysis of field observations with a simple flow routing algorithm to predict the inundated area of a lahar. The model input is the total volume and, with a DEM to determine flow routing, LAHARZ does not require any other parameters. The model does not account for bulking explicitly (although this is implicitly included through the calibrated scaling relationship) or changes in topography. Additionally, the routing algorithm is a simple steepest descent model so flows are confined to unique streams given initiation points, and the lahar cannot overflow from one channel to another as is commonly observed in real cases. Thus, LAHARZ gives limited information, specifically a constant cross section along the thalweg and the planimetric inundation area of the lahar. Its advantages are that it is simple, fast and has been applied widely in different settings (e.g., Muñoz-Salinas et al. 2009; Huggel et al. 2008).

In contrast to the semi-empirical LAHARZ model, physics-based models attempt to describe the complex fluid dynamics of lahars. Physics-based models adopt equations for the conservation of mass and momentum of the constituents of the lahar, with constitutive relationships to close the model. Several physics-based models have been developed for surface mass flows, and some of these have been applied to model lahars.

Flo-2D is a hydraulic, single phase, shallow-layer model (O'Brien, 2007) developed for fluvial systems, which has been extended to include sediment transport. Flo-2D uses a hydrograph as the input of the flowing material and adopts a fixed depth-averaged rheology in which the shear stress has contributions from the mixture viscosity, a turbulent dissipative friction and a mixture yield strength, represented by several parameters in the model. Flo-2D has been used for lahars (e.g., Worni et al. 2012; Caballero & Capra, 2014; Charbonnier et al., 2018) with reasonable results, but the model uses either the kinematic or diffusive wave approximations of the conservation of momentum equation (O'Brien, 2007; Charbonnier et al., 2018), so there is an incomplete description of evolution of the flow. This could significantly affect the model predictions, particularly as unsteady processes such as erosion and deposition that alters the composition of the flow and changes the topography, result in changes in rheology of unsteady and non-uniform flows.

RAMMS (Christen, M., Kowalski, J. & Bartelt, P. 2010) is also a physics-based shallow-layer model for a single-phase fluid with constant density and solid concentration. Originally developed for dense snow avalanches, RAMMS has also been applied to lahars (e.g., Frimberger, 2021). The resistance to motion (drag) is modelled using the Voellmy-Salm equation, which include a fluid drag term and a Coulomb dry-granular friction term. The fluid drag is modelled as proportional to the square of the flow speed, while the Coulomb dry-granular drag is proportional to the flow thickness and independent of flow speed. These contributions to drag are not weighted by solid concentration. Instead, in the Voellmy-Salm model both fluid and dry-granular drag simply added together. This has some important consequences, as the Coulomb drag dominates when the flow is deep or is arresting, while the fluid



drag term dominates at high velocities. RAMMS includes an algorithm to model the bulking process by erosion as function of a critical shear stress at the base, where erodible material is incorporated to flow volume, but the model does not account for changes in topography that occur due to erosion and deposition of solid material.

DCLAW is a sophisticated depth-averaged model for highly concentrated debris flows (Iverson & George, 2014; George & Iverson, 2014), and is based on pore-pressure support of granular materials in a description based on fluid flow in a saturated porous media. High pore-fluid pressure within a deforming granular matrix leads to liquefaction of the mixture and greatly increased mobility. This is modelled in DCLAW through drag terms that depend on the local pore-pressure which itself evolves as the granular material dilates (Iverson & George, 2014; George & Iverson, 2014). This model formulation allows DCLAW to simulate flows initiated from the destabilisation of an area of the ground by elevated pore-pressure in the substrate, but the parameterization is limited to the debris flow regime where the mixture is sufficiently concentrated to form a granular matrix. Therefore, it is difficult to apply this description to lahars if there is a transition from debris flows to hyperconcentrated flows, e.g. due to bulking and debulking.

## 3.2 Overview of the LaharFlow model

In this study, we adopt the LaharFlow model (Woodhouse et al., In prep.), which is a shallow-layer model of lahars that can be applied on topography. Thus, LaharFlow has similarities to the Flo-2D, RAMMS and DCLAW models. However, LaharFlow differs in some of the model physics and parameterizations. Here we give a brief overview of the model.

### 3.2.1 Shallow-layer model of lahars as sediment concentrated flows

LaharFlow uses a depth-averaged framework to model the dynamics of lahars as a mixture of sediments and water. The very fine sediments, that remain in suspension for long times, are considered together with water as the fluid phase. The remaining coarser solid particles in the mixture can be deposited, and solid material can be entrained by erosion of the substrate. The evolution of the mixture composition in lahars effects the flow dynamics (Iverson, 1997), with a two-way coupling (Figure 30), and this is included in LaharFlow through parameterizations of physical processes which are functions of the solids concentration.

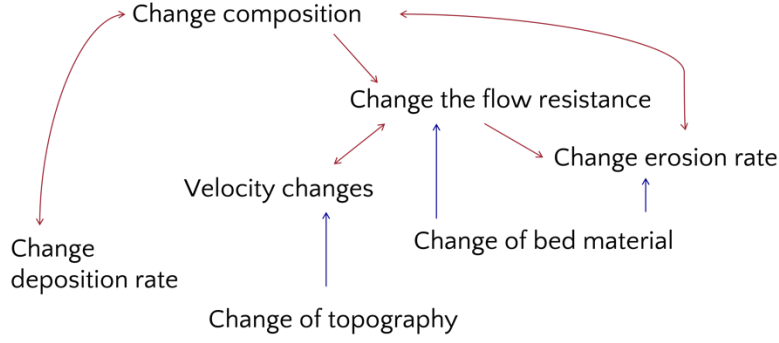


Figure 30. A simplified process diagram illustrating the coupling of physical processes in the LaharFlow model. Red arrows link processes internal to the flow. Blue arrows indicate external forcings acting on the flowing layer.

Figure 30 presents a simplified diagram of the main physical processes that are described in LaharFlow. As the lahar propagates, changes to the composition of the layer in space and time can result in changes to the resistance to motion. This causes local accelerations, but also alters the stresses acting on the substrate, changing the rate of entrainment of solid material and thus feeding back on the composition of the flow. Additionally, compositional changes affect the rate of deposition of material. These internal processes are also affected by external forcings, and two prominent forcings are highlighted in Figure 30. Changes in topography directly alter the gravitational forcing experienced by the flowing layer, leading to local accelerations. There could also be changes of bed material, which will affect the flow resistance and rate of erosion of bed material.

The details of the dependencies of the physical processes are encoded in mathematical equations of motion, derived from conservation laws. By invoking the shallowness of the flow in comparison to the lateral length scales, the equations of motion of the fluid mixture can be reduced to two-dimensional, time-dependent equations for the conservation of the bulk mass,

$$\frac{\partial}{\partial t}(\bar{\rho}h) + \frac{\partial}{\partial x}(\bar{\rho}h\bar{u}) + \frac{\partial}{\partial y}(\bar{\rho}h\bar{v}) = \rho_b \frac{E-D}{\psi_b}, \quad (8)$$

conservation of the solid mass,

$$\frac{\partial}{\partial t}(\bar{\rho}h\bar{c}) + \frac{\partial}{\partial x}(\bar{\rho}h\bar{u}\bar{c}) + \frac{\partial}{\partial y}(\bar{\rho}h\bar{v}\bar{c}) = \psi_b \rho_s (E - D), \quad (9)$$

and the conservation of momentum,

$$\begin{aligned} \frac{\partial}{\partial t}(\bar{\rho}h\bar{u}) + \frac{\partial}{\partial x}\left(\bar{\rho}h\bar{u}^2 + \frac{1}{2}\bar{\rho}gh^2\right) + \frac{\partial}{\partial y}(\bar{\rho}h\bar{u}\bar{v}) &= -\bar{\rho}gh\frac{\partial b}{\partial x} - \tau_{bx} + u_b\rho_b\frac{E-D}{\psi_b}, \\ \frac{\partial}{\partial t}(\bar{\rho}h\bar{v}) + \frac{\partial}{\partial x}(\bar{\rho}h\bar{u}\bar{v}) + \frac{\partial}{\partial y}\left(\bar{\rho}h\bar{v}^2 + \frac{1}{2}\bar{\rho}gh^2\right) &= -\bar{\rho}gh\frac{\partial b}{\partial y} - \tau_{by} + v_b\rho_b\frac{E-D}{\psi_b}. \end{aligned} \quad (10)$$

Here  $\bar{\rho}$  is the depth-averaged lahar density,  $h$  is the lahar depth,  $\bar{c}$  is the depth-averaged solids mass concentration, and  $\bar{\mathbf{u}} = (\bar{u}, \bar{v})$  is the lateral velocity with components in the  $x$  and  $y$  directions,

respectively. The bed density is denoted by  $\rho_b$ , with  $\psi_b$  denoting the volume fraction of particles in the bed, and  $\rho_s$  is the density of solid particles (assumed constant). The topographic elevation is given by  $b(x, y, t)$ . The rate of erosion of bed material is denoted by  $E$ , while  $D$  denotes the deposition rate of material from the flowing layer onto the bed. We note that the erosion and deposition occur in the direction normal to the bed, and therefore processes such as bank erosion are not modelled. The bed shear stresses are given by  $\tau_{bx}$  and  $\tau_{by}$ , with  $u_b$  and  $v_b$  denoting the velocity of the flowing layer at the bed. The gravitational acceleration is given by  $g$  and the time by  $t$ .

The term on the right-hand-side of (1) gives the net rate of change of mass due to erosion and deposition, and the corresponding term in (2), specifying the rate of change of solid mass. The forcing terms on the right-hand-side of the momentum conservation equations (3) are, respectively, the gravitational forcing due to topographic slopes, basal shear stresses that resist the motion (often referred to as the drag terms), and momentum exchange terms due to entrainment and deposition of material.

Erosion and deposition of material alter the topography over which the lahar propagates, and this effect can be substantial where large quantities of bed material are mobilized and relocated. To capture this process, LaharFlow includes an equation for the ‘*morphodynamic link*’ (Woodhouse et al., In prep.),

$$\frac{\partial b}{\partial t} = \rho_b \frac{D-E}{\psi_b}, \quad (11)$$

which simply states that the topographic elevation at each point falls if erosion exceeds deposition, and rises if deposition is dominant. As the erosion occurs normal to the bed slope, if the topography is represented at sufficiently high resolution, the channel banks can be eroded. However, DEMs of sufficiently high resolution to resolve the channel banks are rarely available over large areas. Additionally, this model does not account for collapse of banks that are undercut by bank erosion, which can substantially alter the topography of the channel.

### 3.2.2 Novel parameterizations in LaharFlow

The equations of motion in LaharFlow, as presented above, are common to shallow-layer models of sediment carrying flows. In order to simulate lahars, closure relationships are given proposed by Woodhouse et al., (In prep.) that aim to capture essential features of lahar dynamics.

#### 3.2.2.1 Flow resistance

In LaharFlow, drag terms are proposed which model the variation of flow resistance as the solids concentration varies. As lahars can span a wide range of solids concentration, from dilute flows with low concentration, through hyperconcentrated flows, to highly concentrated debris flows, the drag must capture pronounced changes in the resistance to motion.

In contrast to RAMMS, the drag in LaharFlow is modelled as weighted contributions of fluid-like drag (at low concentration) and granular drag (at high concentration),

$$\tau_{bx} = \left( C_d |\bar{\mathbf{u}}|^2 [1 - f(\bar{\psi})] + \mu(I) gh f(\bar{\psi}) \right) \bar{\rho} \bar{\mathbf{u}} / |\bar{\mathbf{u}}|, \quad (12)$$

and similarly, for  $\tau_{by}$ . This form is a generalization of Voellmy drag (Voellmy, 1955). Here  $f(\bar{\psi})$  is a switching function (which we refer to as the Voellmy switching function), depending on the depth-averaged solids volume fraction  $\bar{\psi}$ , with

$$f(\bar{\psi}) = \frac{1}{2} \left[ 1 + \tanh \left( \lambda (\bar{\psi} - \psi_0) \right) \right]. \quad (13)$$

This form of the switching function is a smooth function with  $f(0) = 0$  and  $f(\bar{\psi}) \rightarrow 1$  as  $\bar{\psi} \rightarrow \psi^*$  where  $\psi^* \approx 0.6$  is the volume concentration at maximum packing. We refer to the parameter  $\lambda$  as the ‘Voellmy switch rate’, as it controls how rapidly the drag changes from fluid-like to granular. The parameter  $\psi_0$  determines the volume fraction at which the transition occurs and is referred to as the ‘Voellmy switch value’. As this is a phenomenological parameterization, and not derived from theoretical analysis, the model parameters  $\lambda$  and  $\psi_0$  must be determined by model calibration.

Therefore, in the dilute limit  $\bar{\psi} \rightarrow 0$  we have  $\tau_{bx} \sim \bar{\rho} C_d |\bar{\mathbf{u}}|^2$ , which is the Chezy form of drag used to model turbulent water flows. The dimensionless parameter  $C_d$  is the Chezy drag parameter.

In contrast, in the concentrated limit  $\bar{\psi} \rightarrow \psi^*$  we have  $\tau_{bx} \sim \bar{\rho} \mu(I) gh$ , which is a Coulomb-like drag model for granular flows. Note, in LaharFlow the Coulomb coefficient is not constant, but is modelled using Pouliquen’s parameterization (see e.g. Forterre & Pouliquen, 2008), with

$$\mu(I) = \mu_1 + \frac{\mu_2 - \mu_1}{I_0 / I + 1}, \quad (14)$$

where  $I = |\bar{\mathbf{u}}| d / h \sqrt{hg \cos \alpha}$  is the dimensionless ‘Inertial number’ with  $d$  denoting the grain diameter and  $\alpha$  the local slope inclination angle. The parameters  $\mu_1$ ,  $\mu_2$  and  $I_0$  are material parameters, and in LaharFlow  $I_0 = 0.136$  is fixed (Forterre & Pouliquen, 2008).

### 3.2.2.2 Bulking through entrainment by erosion

The erosional entrainment of material is modelled in LaharFlow using a parameterization adopted from hydraulics of streamflows. This assumes that mobilization of bed material is due to a competition between destabilization of sediments by shear stresses and the stabilizing effect of particle weight, which is classically quantified through the dimensionless ‘Shields number’ (e.g. Raudkivi, 1976),

$$\theta = \frac{|\tau_b|}{(\rho_s - \rho_f)gd}, \quad (15)$$

where  $|\tau_b|$  is the magnitude of the shear stresses acting on the bed and  $(\rho_s - \rho_f)gd$  gives the submerged weight of a bed grain of diameter  $d$ . If  $\theta \ll 1$  the shear stress is insufficient to overcome the weight of the grain, and there is no erosion. In contrast, if  $\theta \gg 1$  the shear stress mobilizes the

grain which is entrained into the flow. Numerous experiments (see Raudkivi, 1976) find that erosion occurs when the Shields stress exceeds a critical value,  $\theta > \theta_c$ , and that  $\theta_c$  is a weak function of the particle Reynold's number  $Re_p = \sqrt{gd^3}/\nu$ , where  $\nu$  is the viscosity of water.

In LaharFlow, if the local Shields number exceeds the critical value, erosion occurs and material is entrained into the flow. A classical hydraulics model of erosion (e.g. Raudkivi, 1976) gives the erosion rate as a function of the excess Shields number, with a linear function sufficient to capture observed trends.

As LaharFlow considers both fluid and granular stresses, the hydraulics erosion model is amended. In particular, static granular material imparts a non-zero shear stress on the bed, but no erosion would be expected. In the granular limit, following Trinh et al. 2017, the critical Shields number is replaced by a 'neutral friction coefficient',  $\mu_N$ , and erosion occurs if the Pouliquen friction exceeds the neutral value. Then, in similarity with the basal stress representation, the erosion rate in LaharFlow is modelled as

$$E/\sqrt{gd} = \epsilon_f[1 - f(\bar{\psi})](\theta - \theta_c) + \epsilon_g f(\bar{\psi})(\mu - \mu_N), \quad (16)$$

where  $\epsilon_f$  is a dimensionless erosion rate in the dilute limit, and  $\epsilon_g$  is a dimensionless erosion rate in the dense granular flow limit.

When material is eroded, it is immediately entrained into the flowing mixture. The neglect of entrainment of material from bank collapse could have a substantial effect on the flow predictions, particularly where vigorous bank erosion occurs for highly erosive hyperconcentrated flows on loose volcanoclastic deposits (Procter et al. 2010) and where inerodible beds promote bank undercutting (Doyle et al. 2011). We are not aware of quantification of bank erosion and collapse by lahars that allow parameterization of entrainment. In the depth-averaged framework, the material that is entrained is assumed to be rapidly mixed, so that the flow is modelled as a well-mixed layer. This neglects the development of concentrated bed-load layers, but significantly simplifies the model.

### 3.2.2.3 Debulking through deposition by sedimentation

Deposition of solid material from the lahar occurs as solid grains settle out of the flow under gravity. In the LaharFlow model, it is assumed that the bulk flow is well-mixed, but material can still settle from the boundary layer to be deposited on the bed. The depositional flux to the bed is given by

$$D = \bar{\psi}w_s, \quad (17)$$

where  $w_s$  is the settling speed of a grain in the flow.

LaharFlow uses an empirical model of particle settling that can be applied over a wide range of solids concentration as it includes hindered settling effects (Spearman and Manning, 2017). This gives the settling speed as



$$w_s = w_{s,0}(1 - \bar{\psi})^{2.7-0.15n}(1 - \bar{\psi}/\bar{\psi}^*)^{0.62n-1.46}, \quad (18)$$

where

$$n = \frac{4.7+0.41Re_p^{3/4}}{1+0.175Re_p^{3/4}}, \quad (19)$$

and  $w_{s,0}$  is the settling speed of an isolated particle, given by Soulsby (1997) as

$$w_{s,0} = \frac{\nu}{d} \sqrt{10.36^2 + 1.048R^3} - 10.36, \quad (20)$$

with  $R = d(g'/\nu^2)^{1/3}$  being a scaled grain size.

### 3.2.3 Model parameters

The LaharFlow model contains parameterizations that are novel and phenomenological, and others that have been verified only in end-member cases. Therefore, there are several parameters whose values are unknown. Table 5 summarizes the parameters in LaharFlow and indicates where values may be measurable, where values from literature could be used, and where parameters are novel.

Table 5. Parameters in the LaharFlow model

Physical process	Parameter	Symbol	Comment	Value or range for calibration
General dynamics	Solid density	$\rho_s$	Measurable	1700 kg m <sup>-3</sup>
	Fluid density	$\rho_f$	Measurable, in principle, but as fluid includes fine grains, may vary in practice.	1000 kg m <sup>-3</sup>
	Fluid viscosity	$\nu$		$1.2 \times 10^{-6}$ m <sup>2</sup> s <sup>-1</sup>
	Bed porosity	$\psi_b$	Measurable, but may vary spatially.	0.35
Drag	Chezy drag	$C_d$	Estimated values for water flows	0.01 – 0.1
	Pouliquen minimum coefficient	$\mu_1$	Material parameters that are measurable, in principle, for monodisperse dry granular flows. Unclear if suitable for saturated and polydisperse flows.	0.1 – 0.2
	Pouliquen maximum coefficient	$\mu_2$		0.25 – 0.5
Drag & Erosion	Voellmy switch value	$\psi_0$	Novel parameters in LaharFlow.	0.2 – 0.6
	Voellmy switch rate	$\lambda$		3 – 10
Erosion	Fluid erosion rate	$\epsilon_f$	Estimated values for water flows	$10^{-4} - 10^{-3}$
	Granular erosion rate	$\epsilon_g$	Novel parameter in LaharFlow	$10^{-2} - 10^{-1}$
Drag, erosion, deposition	Particle diameter	$d$	Representative particle diameter, influences granular drag, erosion and deposition rate. In principle measurable, but not clear how to account for polydispersity.	1 mm

We have chosen to fix the particle diameter in the model, despite there being substantial variation in the clast characteristics in the flows (Figure 22). This is because of the role of the particle diameter parameter in the model, which predominantly controls the rates of erosion and deposition, but also affects the granular drag. LaharFlow represents the particle size as a single parameter. However, lahars carry particles spanning a large range of shapes and sizes, with both primary volcanic material and entrained debris, and there is considerable spatial variation in the characteristics of the solid material (Vallance & Iverson, 2015). This is challenging to capture in models, for several reasons.

Firstly, there would need to be separate mass conservation equations for each grain class. While, in principle, this is straight-forward, it would likely increase the computational time. Secondly, the contributions of each grain class to the bulk mixture dynamics would need to be parameterized. For example, the contributions of each grain class to the bulk drag would need to be specified. We are not aware of parameterizations for spatially and temporally evolving polydisperse mixtures that could be used. Thirdly, the numerical solution of a multicomponent system would require appropriate initial and boundary conditions. This would mean the initial grain-size distribution of the lahar at the source would be needed, along with specification of the grain-size distribution of the substrate across the flow domain. These are likely to be difficult to constrain, and highly uncertain.

By simplifying to a single representative particle diameter, the model removes these complexities and additional uncertain parameters. However, the assumption adds significantly to the *structural uncertainty* (Kennedy & O'Hagan, 2001) of the model, which is the implicit uncertainty due to idealization, approximation, and missing physics in the model. Characterizing structural uncertainty is difficult, as it requires intercomparison of model predictions with a more sophisticated model that includes the additional complexities.

Our choice of a fixed solid diameter of 1 mm is guided by preliminary simulations that determined that this particle size is appropriate to obtain reasonable, order-of-magnitude appropriate predictions of the volume and distribution of erosion and deposition. Grain sizes of 1 cm and larger produce model predictions of very limited erosion, as large grains require larger shear-stress to erode than small grains in the erosion parameterization. Grains smaller than 0.1 mm produce predictions with very widespread erosion and little deposition, as these grains are eroded with relatively low shear-stress and have long deposition times.

### 3.2.4 Source parameterization as hydrograph

We model the release of material with a hydrograph (i.e., a time series of the flux of a mixture of water and solids). In LaharFlow, the material is released from a circular area at a specified location. This is a modelling choice to represent the source area. Locally, there is a radial flow from the source area, but topographic slopes result in a routing of the released material downstream. However, in the region proximal to the source there can be significant upslope and cross-slope flows. Additionally, the near source flows can erode and deposit material. This erosion can be useful for generating a concentrated flow without needing to specify the source concentration. Therefore, the near-source region should not

be considered an accurate representation of the flow but is a modelling convenience for introducing material.

The specification of the hydrograph is a critical element of the model application. Typically, there is insufficient information to prescribe the hydrograph in detail, and simple timeseries are then preferred to limit the number of free parameters used to model the source (Figure 31).

Field measurements, such as total volume of deposit, cross section area in the source region and estimates of flow speed, are useful to constrain the source hydrograph. The hydrograph shape could be directly related to the chronology of volcanic activity, water availability and its rate of release, the bed slope and erosion potential, and hydrological conditions. Thus, three end member hydrographs could be simplified for multiple scenarios of flows (Figure 31): (1) a sudden water collapse and release for lahar, like those triggered by lake break, glacier mechanical collapse or trapped subglacial lake failure; (2) a sustainable multi peak flow, similar to those triggered by incorporation of water into pyroclastic material produced by continuous partial collapse of a column or spatter avalanche under continuous unstable accumulation in high slope terrains (e.g., the flows that occurred at Villarrica in 2015, and in the Rio Este valley at Calbuco in 2015); and (3) a long duration (hours—days) hydrograph, with a quasi-steady regime of aggradation flows where there are no distinctive peaks of flow, suitable for flow triggered by rainfall as occurred in the Rio Blanco-Hueñu Hueñu during the Calbuco eruption or in the Chaitén town in Chaitén eruption 2008 (Pierson et al., 2013). More complex hydrographs could occur due simultaneous processes and could be parametrized by combining the generic forms illustrated in Figure 31.

While parameters specifying the hydrograph could be measured in the field, from the monitoring of the eruption (that could be instrumental, or documented by media, local communities, and authorities), or extracted from analogue cases, in many cases there are few observations that constrain the source. When accurate measurements are not available, it is appropriate to use simple descriptions of the hydrograph, such as one of the generic cases illustrated in Figure 31, with relatively few parameters. We may then attempt to calibrate the source parameters alongside model parameters, and to quantify the effect of uncertainties in the source specification, including the total volume released, duration and peak flux.

In some cases, field observations give a constraint on the total volume released at the source. This may be from estimates of the volume drained from a crater lake, rainfall totals over a catchment using meteorological measurement, or water volume derived from glacial melt determined from pre- and post-event mapping of glacial extent. A total volume estimate can be used to constrain parameters in the hydrograph model, but we note that the volume estimate is likely to be uncertain and this should be considered when specifying source parameters.

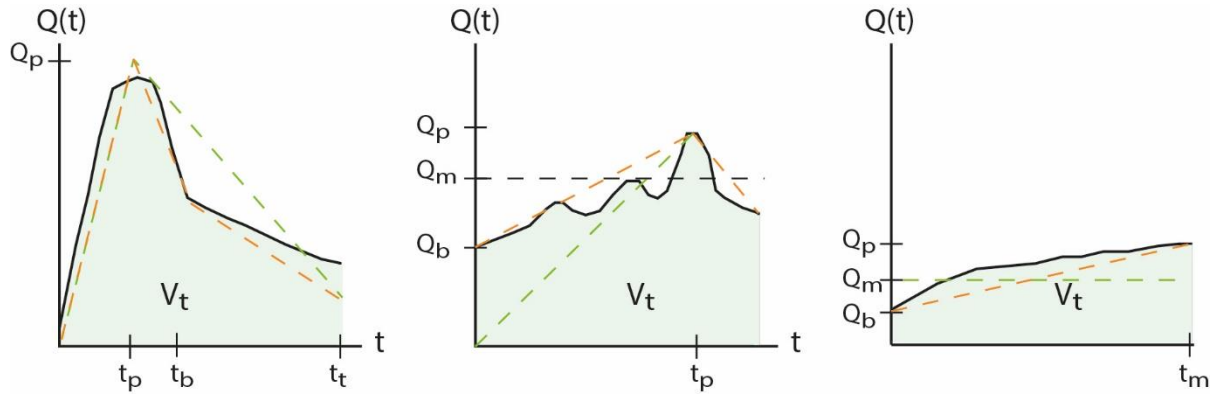


Figure 31. Idealized hydrographs for the different types of lahar, giving the volumetric discharge  $Q$  as a function of time  $t$ . The total volume released,  $V_t$ , is the integral of the discharge over time (i.e., the area under the hydrograph). The left-hand panel represents a sudden water release flow, with a rapid increase in the flux to peak discharge  $Q_p$  at time  $t_p$ , before the flux decreases. The middle panel illustrates a sustained water release, with a gradually increasing but fluctuating discharge, with mean value  $Q_m$ . The right-hand panel shows a quasi-steady discharge.  $Q_b$  denotes the base discharge that occurs before the lahar initiation,  $t_p$  denotes the time of peak discharge, and  $t_t$  the time of dilution.

### 3.3 Model calibration

As lahars are complex multiphase flows, there is insufficient theoretical knowledge to develop models that are completely specified, and instead models adopt empiricisms and contain parameters whose values are unknown or uncertain. In order to apply such models to natural flows, it is necessary to calibrate model parameters. Model calibration relies on (i) observational data with which to compare model simulations, (ii) appropriate model forcing data (e.g., DEM that is an adequate representation of topography at the time of the event), and (iii) ensembles of model simulations. There are two main approaches to model calibration: optimization (Aster et al. 2013) and Bayesian calibration (Kennedy & O'Hagan, 2001).

#### 3.3.1 Calibration as optimization

In an optimization approach, a 'cost' function (also known as an 'objective' function) is proposed that measures the mismatch between the model predictions of quantities of interest and the measured values. For example, a common cost function is the *sum of square residuals* (Aster et al. 2013) which combines each quantity of interest, and it is possible to weight quantities of interest to give increased importance to outputs of particular interest. The model parameters are systematically varied to seek the minimum value of the cost function; this is an optimization problem and there are several numerical techniques that can be used to locate the minimum. The parameters that produce the minimum value of the cost function are then considered the calibrated model parameters.

Calibration through optimization can be an efficient method and can be automated. However, there are some challenges that can make optimization ineffective. For models with more than a few parameters, optimization can be computationally expensive, and algorithms may not converge to global minimum

values. Additionally, for multivariable cost functions, there may be several local minima of comparable magnitude, each given ‘*acceptable*’ matches of model predictions to observations. In these cases, taking the global minimum (or smallest of those found) results in *overfitting* (e.g., Hawkins, 2004) with the result that predictions of events that differ from the calibration data are poor.

As an example, consider a model with three parameters, denoted  $a$ ,  $b$ , and  $c$ , with a cost function  $F(a, b, c)$  that we minimize. It is possible that distinct values that produce similar values of the cost function,  $F(a_1, b_1, c_1) \approx F(a_2, b_2, c_2)$ . Additionally, we may find that we can produce small values of the cost function for any value of one of the parameters:  $F(a_1, b_1, c_1) \approx F(a_1, b_1, c_2) \approx \dots \approx F(a_1, b_1, c_n)$ . In this case, the parameter  $c$  can take any value and a match of predictions to observations obtained, so  $c$  is referred to as an *inactive parameter*, while parameters  $a$  and  $b$  are *active parameters*. Note, this does not mean that the model in general is insensitive to inactive parameters, but instead that model predictions of observed quantities are not sensitive to inactive parameters. The emergence of inactive parameters then depends on the form of the cost function, and non-uniform weighting of observations may be necessary.

### 3.3.2 Bayesian framework for calibration

Optimization methods for calibration are also not straight-forward to apply when accounting for observational and model uncertainties. Measurements of natural features are always subject to uncertainty, and the Bayesian statistical framework is a powerful approach to rationalising, quantifying, and communicating these uncertainties and their consequences on model predictions (Bolstad & Curran 2016).

Model uncertainties arise due to finite resolution of numerical algorithms, approximations in model equations, application of empiricisms, the use of imprecise data (e.g., DEMs are rarely acquired with temporal proximity to an event), and lack of knowledge of model parameters. These are epistemic uncertainties that, in principle, can be reduced by improving the model, numerical resolution, and data.

Additionally, observations are uncertain, with both epistemic and aleatory components. Taking as an example the depth of a flow, it is difficult to determine an accurate and precise value without a direct measurement at the moment of a flow. Field measurements made after events are subject to interpretation. Flow markings on trees or buildings could be attributable to multiple pulses and variation in channel morphology between pulses would make determination of the flow depth difficult. For example, an early pulse may leave deposits around a structure, so that a peak depth mark from a later pulse could appear to be deeper, relative to the pre-event topography, than occurred. If subsequent pulses, or ordinary streamflows, rework and remove deposits from around structures then unravelling the sequence of events and correctly interpreting the depth marking could be extremely difficult.

Among the parameters of a lahar model (including LaharFlow), only few are precise physical properties (e.g. density/viscosity of water) and, in contrast, most are simplified representations of more complex physical processes than are not fully modelled (e.g., drag as representation of fluid—solid interacts at



a rough boundary). While the material parameters are, in principle, measurable, it is unlikely the process parameters have a single value, but instead there is a distribution of plausible values. In calibrating the processes parameters our aim is to determine the distribution of values. Bayesian statistics relates the distribution to our degree-of-belief in a particular value for a parameter. If the distribution for a parameter has a high variance, then the parameter is uncertain, whereas low-variance distributions indicate that a parameter value is known with greater confidence (Bolstad & Curran 2016). Inactive parameters are identified as those with near-uniform distributions (i.e., no value is preferred).

To include measurement uncertainty in calibration of parameters, we treat the numerical simulator as a function  $f$  mapping model parameters  $\theta$  (including source conditions) to a model outputs  $y$ , and include an error term  $\epsilon$  accounting for aleatoric measurement uncertainty and non-systematic variation in model outputs,

$$y = f(\theta) + \epsilon.$$

Additionally, a model has limited ability to reproduce observable quantities precisely (known as model discrepancy; Kennedy & O'Hagan, 2001), due to idealizations, approximations and missing physics in the model as well as inaccuracies in forcing data (e.g, DEM). These model discrepancies may vary systematically the flow state and with parameters and depend on the model output of interest. Including these epistemic uncertainties in the model discrepancy,  $m(\theta)$ , results a system of the form

$$y = f(\theta) + m(\theta) + \epsilon.$$

In a full Bayesian calibration (Kennedy & O'Hagan, 2001) a probability distribution is specified for the error  $\epsilon$  and the model discrepancy  $m(\theta)$  is parameterized. Prior distributions are prescribed for the model parameters  $\theta$  and observations are used in a likelihood function to infer posterior distributions for the model parameters using Bayes' law. Such an approach typically utilises Markov-Chain Monte Carlo methods and is extremely challenging for complex models (Vernon, Goldstein & Bower, 2010) and often utilizes model emulation (Kennedy & O'Hagan, 2001; Navarro et al., 2018).

A simplified approach, which maintains the philosophy of Bayesian calibration but without the need for full inference computation is the '*history matching*' method proposed by Vernon, Goldstein & Bower (2010) (see also, Woodhouse et al. 2015). Here, the parameter calibration is performed through an ensemble of simulations, and each model run is evaluated using a model implausibility measure (Vernon, Goldstein & Bower, 2010),

$$I(\theta) = \frac{(y_{obs} - f(\theta))^2}{(var(m(\theta)) + var(\epsilon))}. \quad (21)$$

The implausibility measures the difference between model predictions and observed values of a quantity of interest, normalized by the uncertainty quantified as the sum of the variance in the model discrepancy (epistemic uncertainty) and the random error (aleatoric uncertainty). High values of  $I(\theta)$  indicate that the parameter set  $\theta$  does not produce a plausible model prediction even accounting for

uncertainty, while low values of the implausibility correspond to acceptable model predictions. An appropriate threshold to distinguish plausible from implausible parameter values must be specified. Note, to apply the implausibility measure in this form requires knowledge of the statistical distributions of the error (often taken to be a Normal distribution, but some measurements may have asymmetric distributions) and the model discrepancy. At this stage of our work, these distributions are not known, so we estimate values based on knowledge of the field measurements and preliminary exploration of model outputs. Note, each model output will have different values of these variances. Further work could estimate the variances from the model simulations.

## 3.4 Objectives

In this study we will calibrate the LaharFlow model using observations of lahars from the 2015 eruption of Calbuco. Specifically:

- we perform an exploration of the parameter space for the LaharFlow model, including both model and source parameters, using an ensemble of simulations;
- we examine the correlation of a range of model outputs to the parameters to identify the active parameters of the model;
- using the observations of the lahars and knowledge of the initiation mechanism, as described in Chapter 1, we perform an initial calibration of LaharFlow, identifying plausible ranges of model parameters and focussing on the active parameters;
- we determine which field observations (type and location) are most valuable in calibration of LaharFlow;
- we produce a lahar inundation map for Calbuco for the 2015 eruption conditions from plausible model simulations.

## 3.5 Methods

### 3.5.1 Observational data

High quality observational data is an essential component of model calibration. In this study we use observations of the lahar in the Rio Blanco that occurred during the 2015 eruption of Calbuco (Chapter 2). While lahars also occurred in other channels draining Calbuco, the flows in the Rio Blanco are

particularly useful for an initial calibration study as the lahars were likely to have been generated by melting of glacial ice disrupted during the eruption (Chapter 2). This provides a constraint on the volume of water available that can be used in specifying the source parameters.

The field observations in the Rio Blanco include punctual flow depth measurements (Figure 32), measurements of the deposit thickness (Figure 33), cross-sections (Figure 34), and the outline of the inundated area (Figure 35).

Twenty-five punctual flow depth measurements span the length of the main flow in the Rio Blanco, from the near source zone to near-to Chapo lake (Figure 32). There is also a single measurement on the Rio Correntoso to the west of Rio Blanco. The flow depths show a complicate variation in response to the changing topography. Generally, depths near to the channel in the proximal region are relatively deep, in excess of 4 m. The flow thins on the flatter topography, but we note that there are some points on the plain where the flow deepens significantly. Indeed, the deepest flow (of nearly 8 m) occurs on the flatter topography.

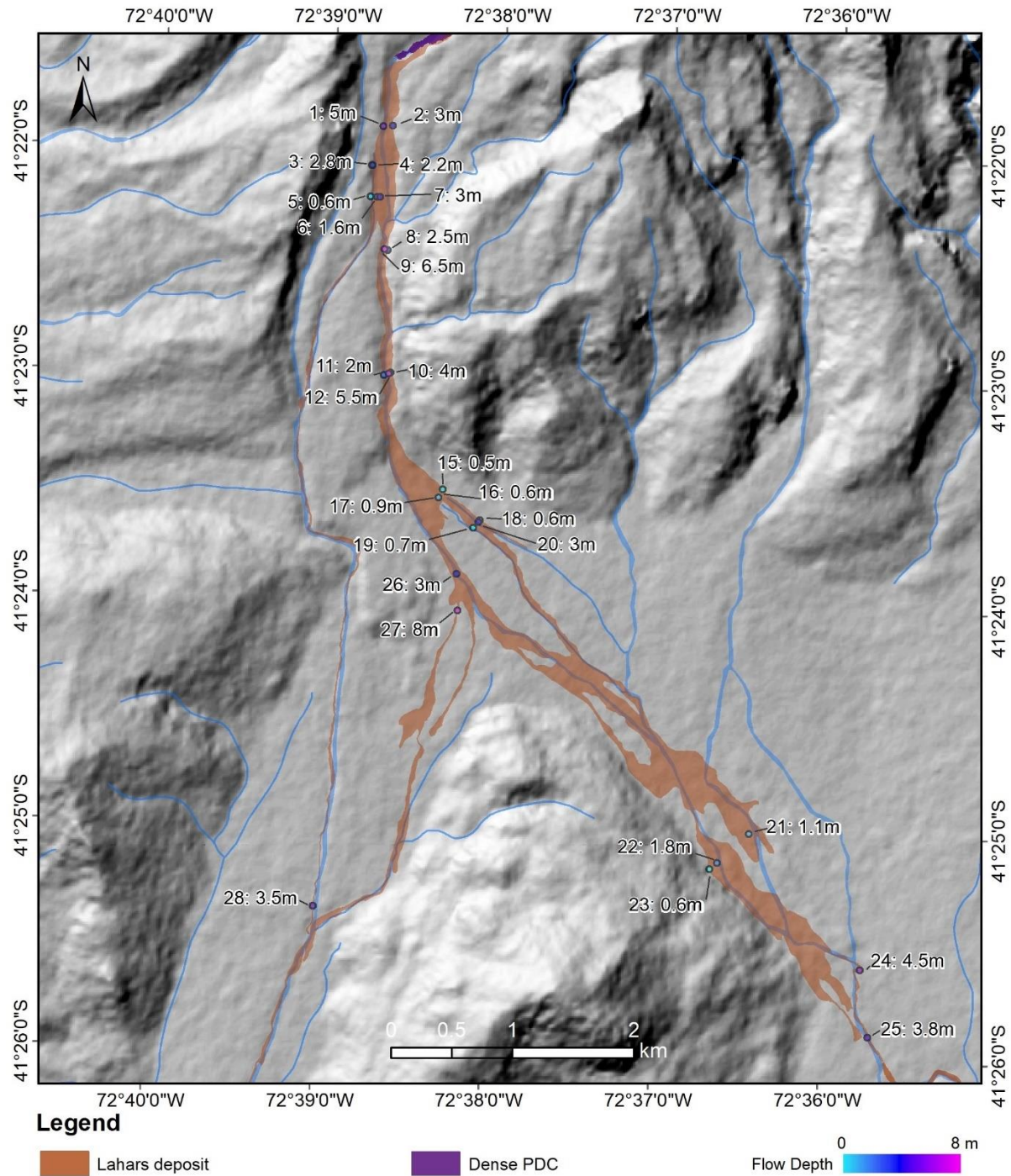


Figure 32. Flow depth measurements in the Rio Blanco catchment at Calbuco volcano. Colours indicate the estimated flow depth. Numbers label the point measurements. The approximate extent of the image is 14 km x 16 km.

Deposit measurements were made at 28 locations along Rio Blanco (Figure 33) and thickness up to 3.5 m were recorded. As for the flow depth, the deposit thickness does not show a simple trend, and there are rapid variations over small distances. For example, deposit sample 12 has a depth of 3.5 m, whereas the nearby samples 10 and 11 have thicknesses of 1.0 and 1.3 m, respectively.



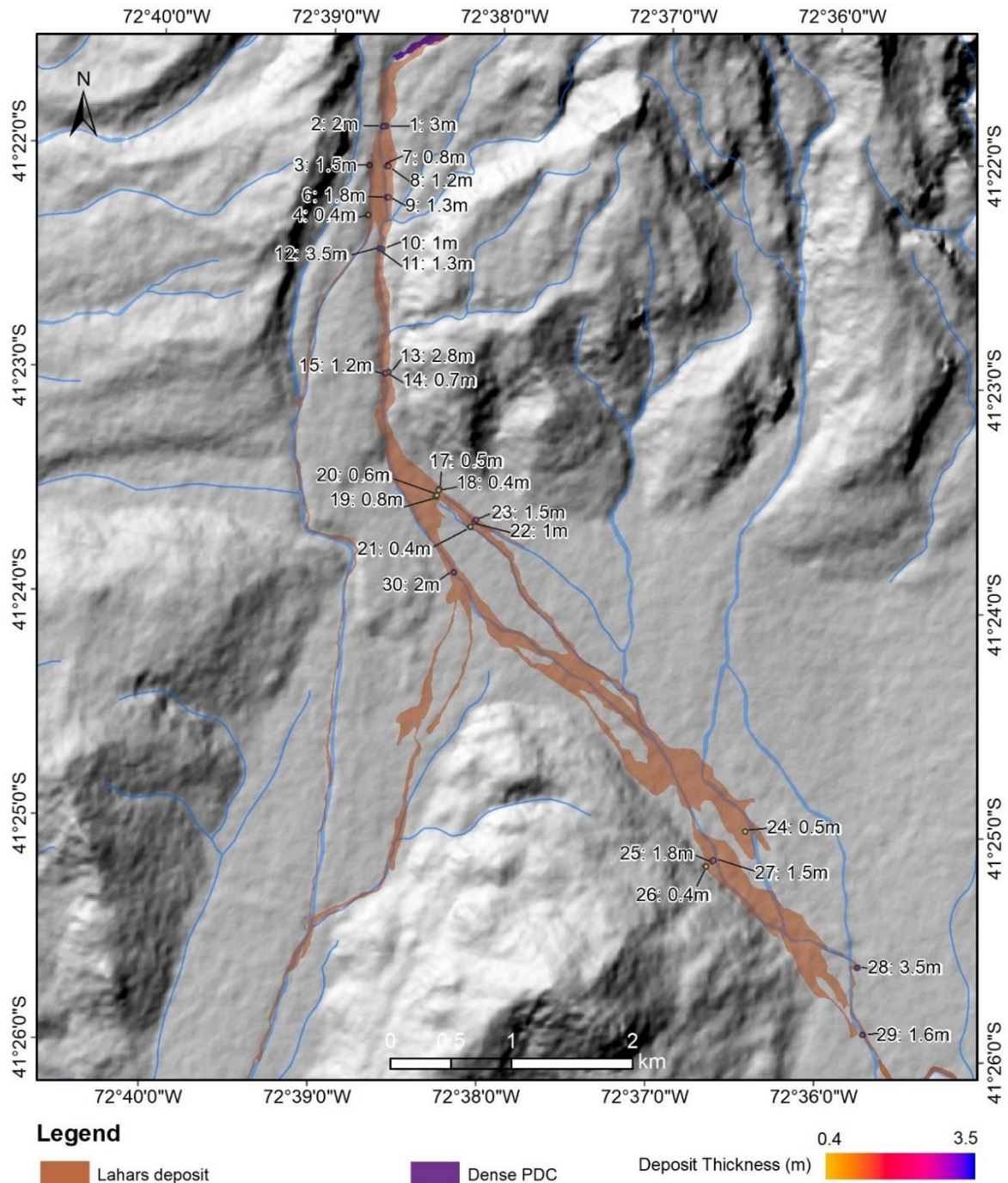


Figure 33. Deposit thickness measurements in the Rio Blanco catchment at Calbuco volcano. Colours indicate the measured deposit thickness. Numbers label the point measurements. The approximate extent of the image is 14 km x 16 km.

Fourteen cross-sections are mapped along the flow path (Figure 34). The cross-section surveys give an estimate of the wetted perimeter at each location, and the approximate flow depth across these transects from the elevation of flow marks at the margins. The length of the cross section varies in response to the topography and the flow extent.



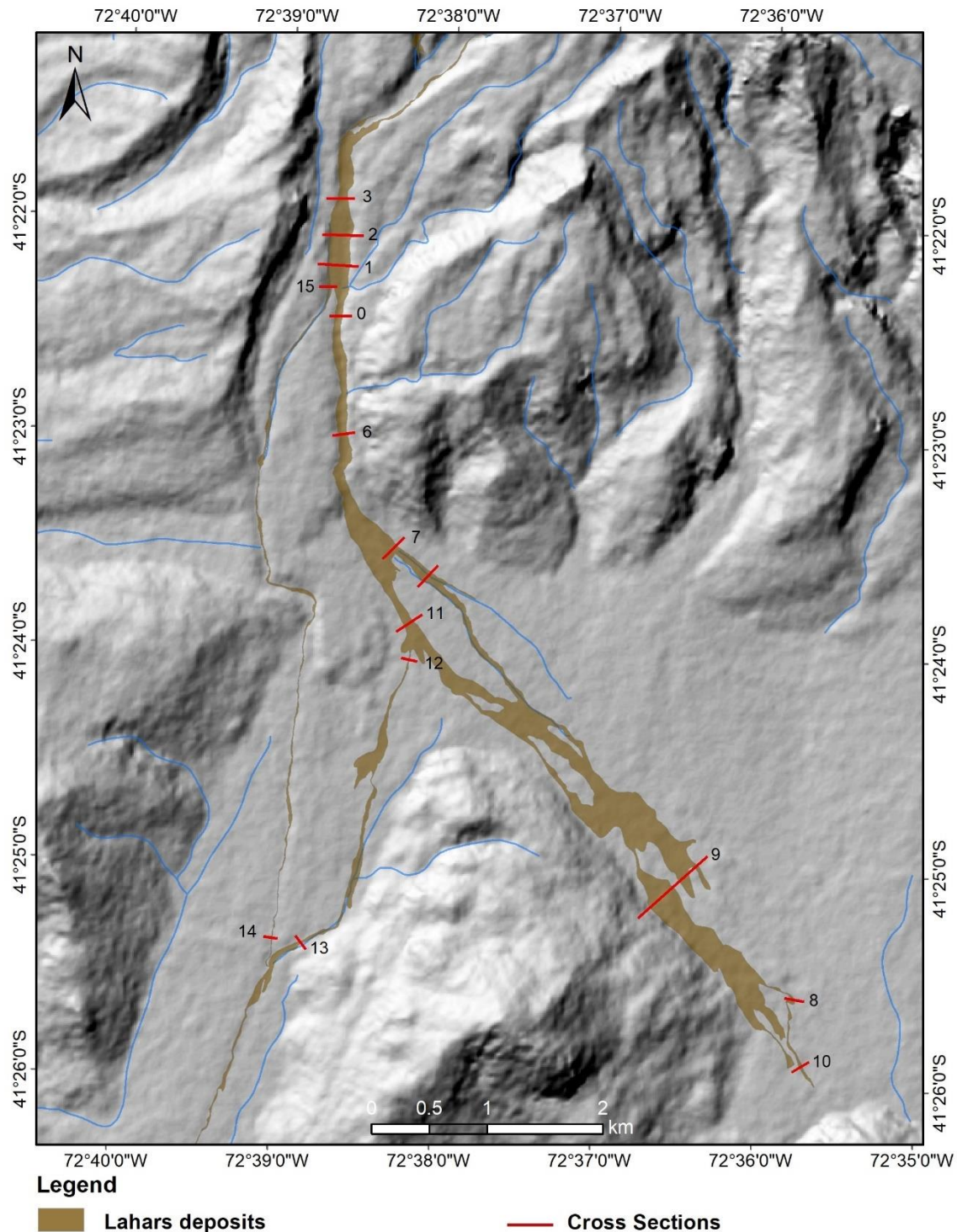


Figure 34. Locations of cross-section surveys at Calbuco. Numbers label the sample locations. The approximate extent of the image is 14 km × 16 km.

The approximate inundated area of the flow is shown in Figure 35. The flow is topographically confined and channel filling in the source proximal zone, but there is substantial overbanking on the flatter topography, particularly in the Rio Blanco. There are at least two bifurcations of flow from the main channel, feeding flows in the Rio Correntoso, one on the steep slopes of the source proximal zone and

the other on the flat plain. Flows in the Rio Correntoso are predominantly channel confined, in contrast to those in the distal part of the Rio Blanco.

In addition to the point measurements, field observations also provide constraints aggregated aspects of the flow dynamics. In particular, we can combine field observations of the flow deposits to estimate the total volume of the deposited material, which we assess to be approximately  $3 \times 10^6 \text{ m}^3$  (Chapter 2) and estimate an uncertainty of  $\pm 20\%$  similar to the uncertainty calculated for our field measurements (section 2.4.2.2). Additionally, we can divide the deposit volume into source-proximal and distal parts. Here we define the proximal zone to be within 3 km of the approximate initiation point of the flow, which contains the steep slopes of the volcanic edifice for the flows in Rio Blanco. We estimate the source-proximal zone to comprise approximately  $5 \times 10^5 \pm 20\% \text{ m}^3$ .

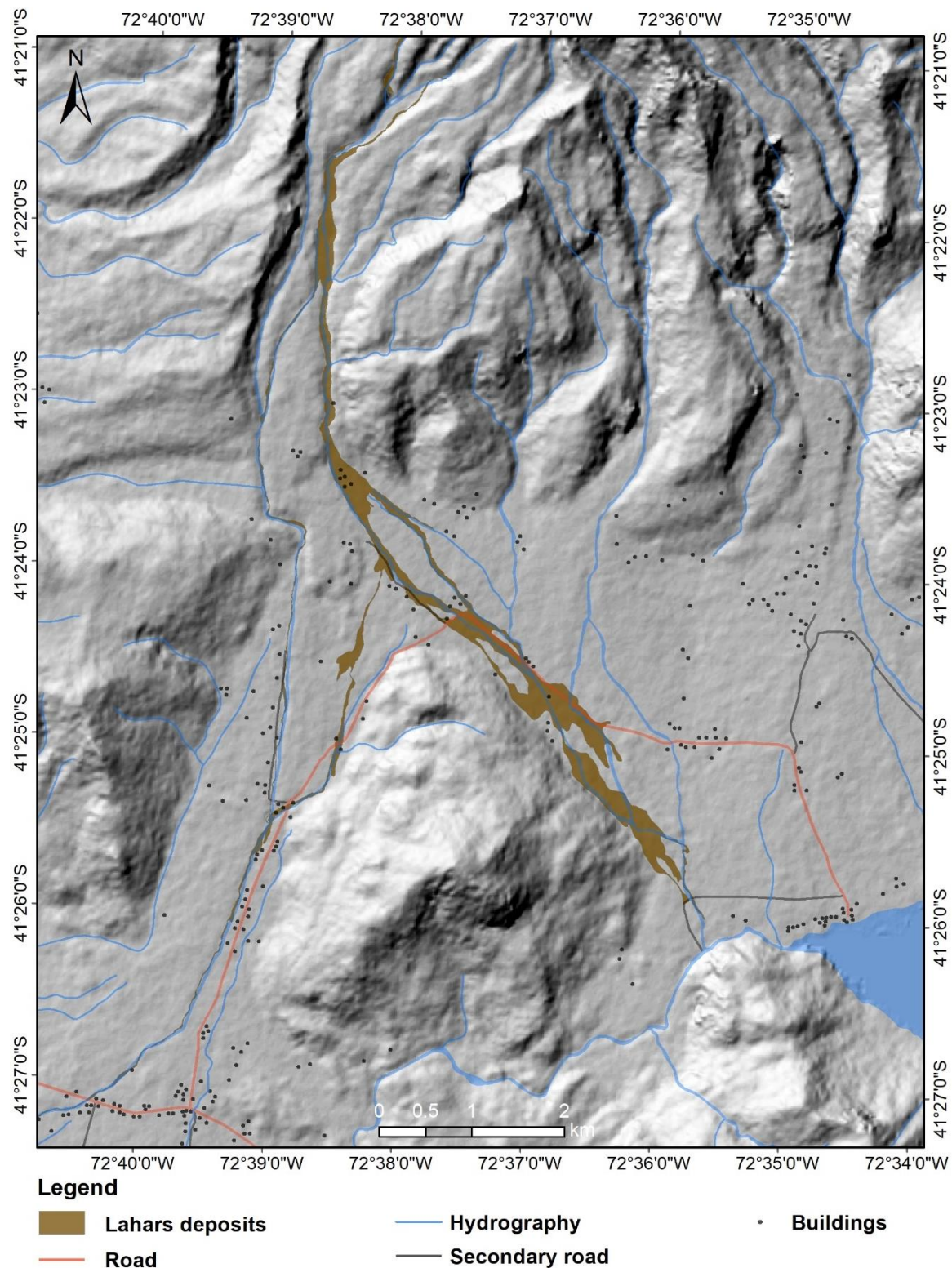


Figure 35. Approximate inundated area of lahars in the Rio Blanco and Rio Correntoso at Calbuco volcano. The approximate extent of the image is 14 km × 16 km.

The measurements of water level at Lake Chapo (Chapter 2) provide a constraint on the arrival time of the lahar at the lake. While the water level measurements are frequent and accurate, there is nevertheless considerable uncertainty in the arrival time as the precise instant of onset of the lahar is

not known. On the basis of the observations described in Chapter 2 we estimate an arrival time at Lake Chapo in the interval 70 – 240 minutes.

### 3.5.2 Preliminary simulations and parameter screening

An initial phase of simulations was performed to determine appropriate ranges for parameter variation. This was undertaken in an unstructured way with manual variation of parameters, and was intended to exclude clearly unphysical parameter values while maintaining large ranges so as to not exclude plausible values.

Additionally, the preliminary simulations were used in as a ‘parameter screening’ to identify parameters that can be fixed on the basis of field observations and other knowledge (Muleta & Nicklow, 2005). We find that fluid and solids densities can be fixed. Furthermore, as discussed above, for this preliminary analysis we have fixed the solid diameter at a representative value. Further work should explore the calibration with a varying solid diameter.

The value of fixed parameters and the range of varying parameters is given in Table 5.

### 3.5.3 Sampling design

To calibrate LaharFlow without introducing unintended biases, we must sample randomly from the prescribed prior distributions. However, we are limited in the size of the ensemble we can generate due to the model run time. We therefore must efficiently sample parameter space, ensuring the sampling is space-filling, and do this using a Latin Hypercube Design (McKay, Beckman & Conover, 2000; Viana, 2016).

Of the seven model parameters, the fluid and granular erosion rates are sampled in a log-uniform distribution, with the remaining five parameters ( $C_d, \mu_1, \mu_2, \psi_0, \lambda$ ) sampled from uniform distributions.

There are more complex dependencies for parameters in the source description, as described further below.

Our Latin hypercube random sampling is performed with a ‘*maximin*’ criterion with five iterations (i.e., five sampling designs are computed and the design that maximizes the minimum distance between sample points is selected). This helps to ensure an efficient space-filling sampling of the parameter space.

We generate a random ensemble with 512 members, with a total of 12 parameters (seven model parameters and five source parameters).

### 3.5.4 Parameterization of the source

To specify the source, we adopt a relatively simple four-point hydrograph (Figure 31) with a steep rising limb to the peak flux, a rapid decline from the peak flux to a lower ‘tail’ flux, with a more gradual decline to zero. This gives five parameters that must be specified in the hydrograph: (i) the peak flux  $Q_p$ , (ii) the time of the peak flux  $t_p$ , (iii) the ‘tail’ flux  $Q_t$ , (iv) the time of the tail flux  $t_t$ , (v) the total duration of the release  $t_d$ .

We impose a constraint of a specified total volume for the release. Our field-based estimate suggests a volume of 6 million  $\text{m}^3$ , but this is subject to considerable uncertainty. We therefore randomly sample the total volume  $V$  of the source from a uniform distribution with a range of 4—8 million  $\text{m}^3$ .

When randomly sampling parameters for the source hydrograph, we must ensure that  $Q_t < Q_p$ ,  $t_p < t_t < t_d$ , and that the area under the hydrograph corresponds to the specified (sampled) volume. To achieve this, we first specify plausible values for the time parameters in the hydrograph, as well as uncertainty estimates, taking  $t_p = 900 \pm 300$  s,  $t_e = 5400 \pm 1800$  s, and

$$t_t = \left( t_p + \frac{t_e - t_p}{4} \right) \pm \frac{t_e - t_p}{300},$$

chosen to ensure that the shape of the hydrograph is appropriate, and based on preliminary exploratory analysis. We sample randomly (using the Latin hypercube design) within the ranges using a uniform distribution, and also sample for the ratio  $Q_t/Q_p$  with

$$Q_t/Q_p = 0.25 \times (1 \pm 0.15).$$

Finally, the peak flux and tail flux can be determined by scaling using the total volume, so that

$$Q_p = 2V / [t_p + (1 + Q_t/Q_p)(t_t - t_p) + Q_t(t_e - t_t)],$$

And

$$Q_t = Q_p \times [Q_t/Q_p].$$

While it is possible to release solids at the source, we choose to specify that there are no solids released at the source. As described above, this is a modelling convenience, and the flow erodes material proximal to the source to become concentrated. If solids are released and the flow is not in morphodynamic equilibrium, there can be rapid deposition due to low flow velocities as the flow accelerates away from the source. This can lead to large near-source deposits that dam the flow. Our preliminary simulations show that releasing only fluid at the source typically results in rapid erosion, bulking up the flow until morphodynamic equilibrium is reached. This is more convenient, and also means that we do not require a parameterization of the solids volume flux at the source. However, it means that the source region is not likely to be a good representation of the flow. For this reason, and to allow the topographic slopes to direct the flow near to the radial source, we place the source upstream by a small distance from the initiation point indicated in the field.



### 3.5.5 Identifying active parameters

To determine the active and inactive parameters for the outputs of interest, we compute correlations coefficients for each model parameter and each output. Where the model outputs are strongly correlated with model parameters, this indicates that the parameter is *active*, with variations in the parameter strongly influencing the predicted value. In contrast, where there is a weak correlation, the output is insensitive to the parameter value, and thus the parameter is *inactive* for the considered output quantity.

In this study we use the Pearson rank correlation coefficient, denoted here by  $r$ . This is a linear measure of correlation so the interpretation can be problematic if there are non-monotonic dependencies of outputs on parameters. However, we have performed manual checks of the correlations using scatter plots and are confident that the correlation coefficient is representative.

To discriminate active and inactive parameters using correlation coefficients, we need to impose thresholds. Here we define ‘*strong*’ ( $|r| \geq 0.75$ ) and ‘*weak*’ ( $0.6 \leq |r| < 0.75$ ) correlations, with correlation coefficients  $|r| < 0.6$  being very weakly or uncorrelated. These are subjective categorizations.

### 3.5.6 Scoring criteria for parameter selection

To assess model simulations, we develop ‘*scoring criteria*’ that compare model predictions of quantities to observed values. Our scoring metrics are based on the implausibility measures of Vernon, Goldstein & Bower (2010) to account for uncertainty in observations and model discrepancies. In this preliminary application, we do not have sufficient knowledge of the model discrepancies to specify their dependencies or statistical distributions. We therefore simplify the implausibility measure given in equation (14), and apply a form

$$I = \frac{(y_{model} - y_{obs})}{(\epsilon_{obs} + \epsilon_{mod})}, \quad (22)$$

where  $y_{model}$  and  $y_{obs}$  denote the modelled and observed values of a quantity  $y$ ,  $\epsilon_{obs}$  is the observation uncertainty (absolute error) associated with  $y_{obs}$ , and  $\epsilon_{mod}$  is an estimate of the model discrepancy associated with  $y_{model}$  expressed as an absolute error. Note, in equation 15, we do not take the square of the residual to identify under- and over-prediction of quantities in the model.

The scoring metric  $I$  identifies model parameter sets that adequately reproduce observations accounting for uncertainty, with ‘*plausible*’ parameters producing scores in the range  $|I| \leq 1$ .

As the model discrepancy cannot be estimated in advance, since it includes the structural uncertainties arising from missing physics, the model discrepancy term is estimated for each quantity of interest by manually adjusting the value to achieve appropriate values of  $I$  while comparing model outputs to observations. This is equivalent to imposing the condition that the model must produce plausible

matches to the observations for some parameter values, so if calibrating model parameters that may differ from measured values for these quantities if they were available.

#### 3.5.6.1 Flow depths

For punctual flow depth observations, we can straightforwardly apply (15) by extracting model outputs at the appropriate points. We use a cubic interpolation to approximate values at the points of interest from the gridded numerical results.

While each measurement will have its own uncertainty and model discrepancy, which could be incorporated into the analysis, for simplicity we apply a uniform observation uncertainty of  $\pm 20\%$  and estimate the model discrepancy to be 1 m. While the model discrepancy may appear to be quite high, we note that predictions of flow depths are likely to be sensitive to errors in the topographic data. Thus, the model discrepancy incorporates topographic uncertainty as well as limitations in the numerical solution (e.g., finite resolution) and physical representation of the model.

#### 3.5.6.2 Flow cross sections

The flow cross sections give the approximate area of the flow in a vertical 2d plane. An analogous quantity is determined from the model simulations by determining maximum flow depths along the transect of the field observations. As the modelled flows may extend beyond the observed extent of the flow, we allow the transect to extend beyond the field cross section until modelled flow depths fall below 1 cm. We then compute the modelled cross-sectional area and compare to the observed value using equation (15).

As for flow depths, we apply a uniform relative error to the cross-section area observations of  $\pm 20\%$ . The model discrepancy is likely to be large for the modelled cross-section, as errors in topography are combined. We estimate a model discrepancy in the flow cross-sectional area of  $\pm 50 \text{ m}^2$ .

#### 3.5.6.3 Total deposit volume

The deposited volume predicted by the model is computed by determining the thickness of the deposit at the final computed time step. Importantly, to correspond with the field observation, the thickness of the deposit must be taken above the minimum topographic elevation and not above the initial topography. Therefore, in the numerical simulation we track the local maximum reduction in the topographic elevation and compute the local deposit depth from these. We then integrate the deposit thickness over the area of the flow.

The observation deposit volume uncertainty is taken to be  $6 \times 10^5 \text{ m}^3$ . It is difficult to assess the model discrepancy. Our analysis shows that we can achieve matches between observations and model

predictions with no model discrepancy, suggesting that the observational uncertainty in the total deposit volume dominates over the model discrepancy.

### 3.5.6.4 Arrival time

The observation of the arrival time, using water level at Lake Chapo, gives an asymmetric observational error, with a best estimate of 90 minutes, a lower estimate of 70 minutes and an upper estimate of 240 minutes. To account for this in the scoring metric, we apply different observational uncertainty values depending on whether the modelled arrival time is earlier than 90 minutes ( $\epsilon_{obs} = 20$  minutes) or later than 90 minutes ( $\epsilon_{obs} = 150$  minutes).

### 3.5.6.5 Inundated area

To compare model simulations to observations of the inundated area, we employ the Jaccard coefficient (see e.g., Charbonnier et al., 2018) which computes

$$J = \frac{|A_{obs} \cap A_{model}|}{|A_{obs} \cup A_{model}|},$$

where  $A_{obs}$  and  $A_{model}$  are polygons of the observed and modelled inundated area. This the Jaccard coefficient compares the overlapping area to the combined area covered by observations and model. The Jaccard coefficient takes values in the range  $0 \leq J \leq 1$ , with  $J = 0$  if there is no overlap of the modelled and observed area, and  $J = 1$  if there is perfect agreement.

The Jaccard coefficient differs from the implausibility score as it does not account for uncertainty. To cast the Jaccard coefficient in a form similar to the implausibility score, we compute the ensemble maximum value of  $J$  and the standard deviation of the ensemble values, and compute

$$I_J = \frac{\max(J) - J_i}{\text{std}(J)},$$

so that  $I_J < 1$  corresponds to relatively high values of the Jaccard coefficient (i.e., good prediction of the observed inundation). Here the standard deviation of the distribution of Jaccard coefficient values in the ensemble is used to quantify the uncertainty, which is likely to be dominated by the model discrepancy.

As with the deposit volume, we can separate the observed inundated area into source-proximal and distal portions. This allows us to assess the ability of the model to predict inundation in channel confined regions and on flatter topography. Here we compute Jaccard-coefficient based scores for the source-proximal region and over the full domain.

### 3.5.6.6 Summary quantities

As an additional criteria to assess the model, and in particular to identify parameters resulting in unphysical flows, we compute scores for the modelled maximum flow depth and maximum speed. While we do not have direct measurements to compare these too, we can use the implausibility based scoring metric to assess the predicted values of these quantities based on physically plausible limits. We incorporate model discrepancy by taking conservative limits of these plausible values, to allow isolated points or small regions in the numerical solution to have unphysical values which are unlikely to lead to problems over the whole computational domain.

For the modelled maximum flow depth, we expect this should not exceed 20 m, as there is no field evidence for flows of such depth. Indeed, our maximum value observed in the field is approximately 8 m, so if predictions reached as high as 20 m at any location we would be unlikely to find the simulation useful. We therefore compute, for each ensemble member,

$$I_{\text{max depth}} = \begin{cases} 0, & \text{if max depth} < 20 \\ 2, & \text{otherwise} \end{cases}$$

Similarly, we can impose a plausible range for the maximum speed. We expect that flow speeds should not exceed 100 ms<sup>-1</sup> (even accounting for model discrepancies) and that a maximum flow speed less than 5 ms<sup>-1</sup> is implausible given the observations. Therefore, we compute a maximum speed score for each simulation in the ensemble as

$$I_{\text{max speed}} = \begin{cases} 0, & \text{if } 5 < \text{max speed} < 20 \\ 2, & \text{otherwise} \end{cases}$$

### 3.5.6.7 Determination of plausible parameter ranges

Each model output has an implausibility score, which we can use to distinguish parameter values as being plausible or implausible. From the ensemble simulations, we determine the distribution of plausible parameter values for each output. These may constrain the input parameter range for active parameters, while the range of inactive parameters are unlikely to be altered.

The implausibility scores could be combined to give an overall score. However, there is value in examining the individual implausibility scores for each output, as it enables us to determine which observations are effective in constraining parameters.

Where the plausible parameter ranges for different outputs overlap, we can then further constrain the parameter range. However, it is possible that the plausible parameter ranges for different model outputs are disjoint, and here it is not possible to determine a simple distribution for a model parameter.

## 3.5.7 Combined inundation map

The implausibility scores distinguish ‘*plausible*’ simulation output in the ensemble from ‘*implausible*’ runs. However, in the simple approach it is not possible to prefer any simulation within the plausible

subset over others. The plausible subset of simulations can nevertheless be combined to produce an inundation map that incorporates uncertainty.

To produce a combined inundation map, we impose a threshold on the flow depth at each point in the flow domain, create binary maps (i.e., value equals unity where flow depth exceeds threshold, and value equals zero below the threshold) for each simulation, and sum these pointwise. The value of the sum at each point can be interpreted as a degree-of-confidence that this point is inundated.

## 3.6 Results

### 3.6.1 Example simulation results

An example of a LaharFlow simulation is shown in Figure 36, which presents a map of predicted maximum flow depth that occurs during the flow. Flow depths up to 20 m are predicted in this simulation at some localized points, with typical depths below 10 m. This result is one of the better performing simulations in the ensemble (run 323).

Figure 36 shows the flow is channel confined and relatively deep on the upper slopes and thins rapidly on the gentle lower slopes where the flow overbanks and floods laterally. The flow in the Rio Correntoso in this simulation is sourced from a small breakout on the upper slopes and a more substantial bifurcation of flows on the flat topography. The flow in the Rio Blanco deepens substantially in the region near to Lake Chapo, which may result from topographic depressions in the DEM.

The flow shown in Figure 36 is morphodynamically active and has an interesting structure of erosion and deposition, as illustrated in Figure 37. There is extensive erosion on the upper slopes, producing a reduction in the topographic elevation by 10 m within the channel centre. These deep incisions are flanked by deposits of up to 3 m in height, forming lateral terraces the further confine the flow. When the flat topography is reached there is a rapid deposition of material and large deposits are formed, reaching up to 8 m in depth. Further downstream, the pattern of erosion and deposition changes, and a cyclic pattern of lower profile bedforms is found, with elevation changes of up to  $\pm 3$  m.



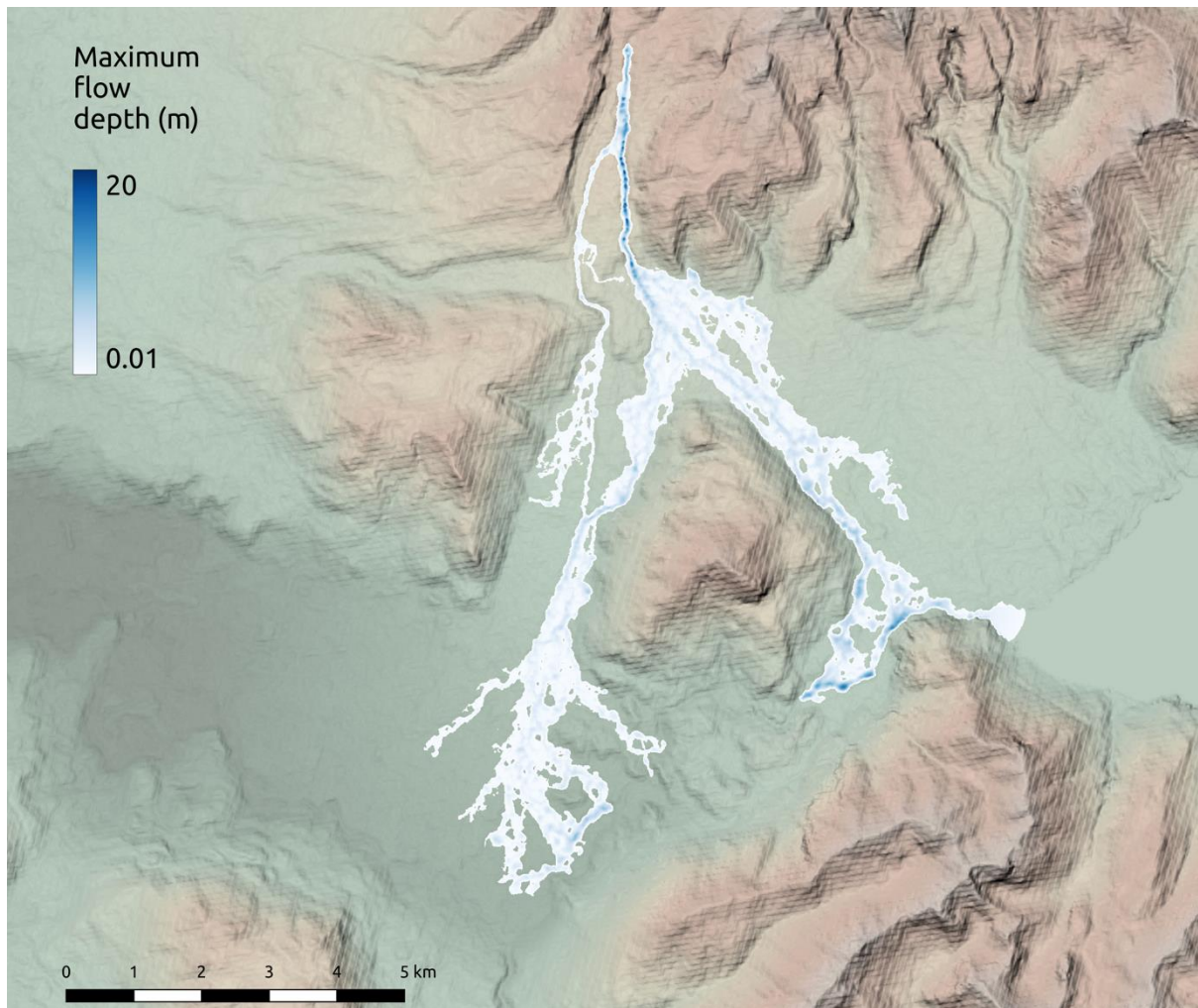


*Figure 36. An example of a prediction of the maximum flow depth for a lahar in Rio Blanco and Rio Correntoso produced by LaharFlow.*

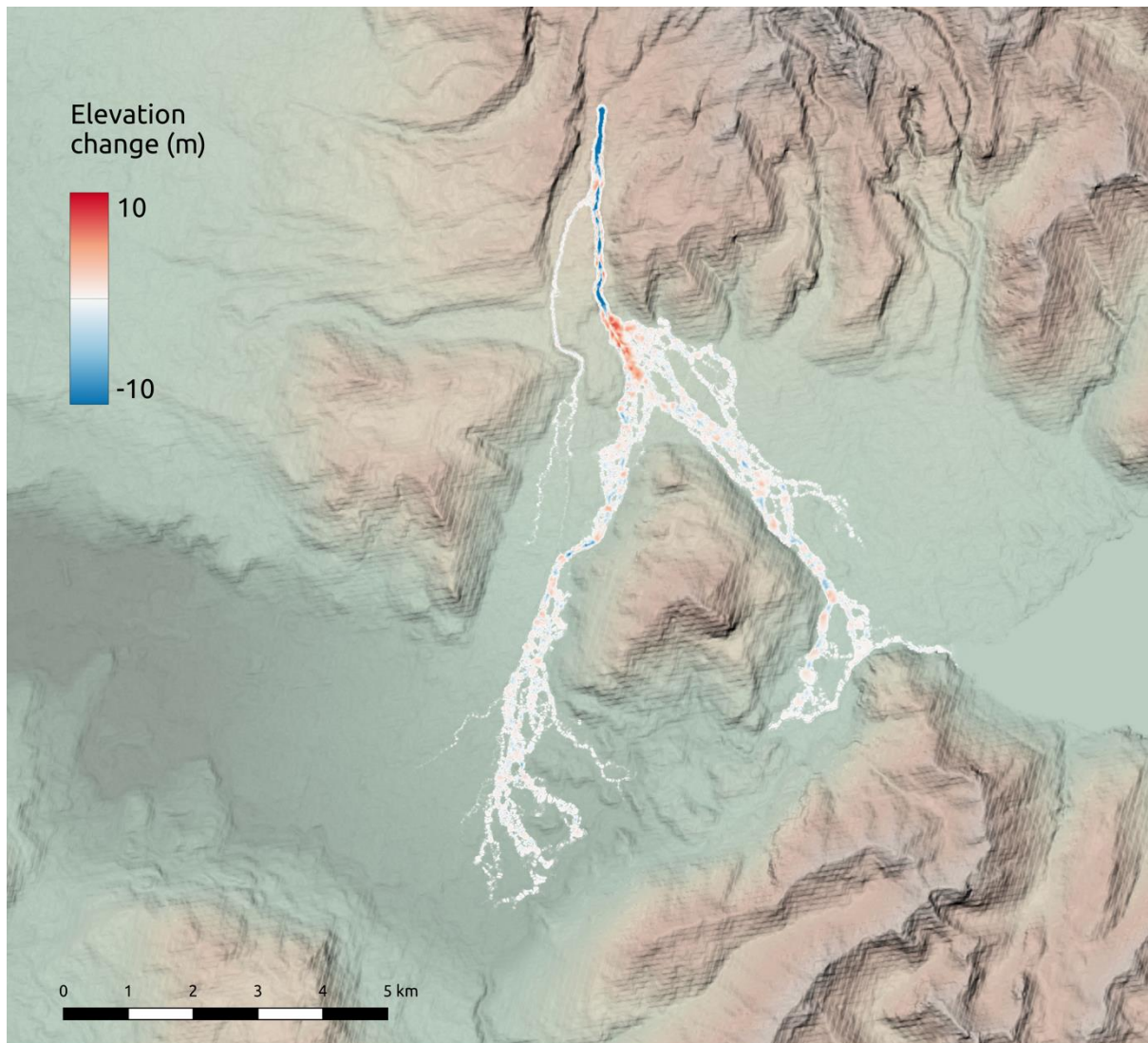


Figure 37. An example of a prediction of the elevation change produced by a lahar in Rio Blanco and Rio Correntoso simulated by LaharFlow.

### 3.6.2 Identification of active model parameters

In Figure 38 we show the correlation coefficients between the model and source parameters and the aggregated and summary model outputs (specifically, the maximum flow depth and speed, Jaccard coefficients for the proximal zone and full domain, the deposit volume in the proximal zone and full domain, and the arrival time of the flow at Lake Chapo). Note the Jaccard coefficient is used here rather than the modelled inundated area, so these outputs include observations, whereas the others are simply model predictions.

For these aggregated and summary model outputs there are few active parameters. Two strong correlations are identified Figure 38, with the deposit volume in the full domain and the maximum flow depth both strongly dependent on the fluid erosion rate. This is in line with our expectation based on

the model physics, as the fluid erosion rate influences the bulking of the flow. Increased erosion results in deeper flows with more sediment available for creating deposits. However, the deposit volume in the proximal zone has a very weak negative correlation with the fluid erosion rate. This may be due to the high erosion rates on the steep channels of the proximal zone, so deposited material can be re-eroded by late-stage flows, with larger volumes removed as the fluid erosion rate increases, and decreasing the deposit volume in the proximal zone.

Figure 38 also shows there is one weak correlation between the arrival time and the Chezy coefficient. This positive correlation can also be understood from the model physics: increasing the Chezy coefficient results in increased drag, slowing flows and resulting in a longer duration.

In Figure 39 we illustrate the correlation coefficients that are computed for the flow depth at the locations of the corresponding observations (Figure 32). In this case we do not find any strong correlations, but there are several weaker correlations and systematic dependencies. For example, the flow depths at all locations are positively correlated with the fluid erosion rate, Chezy coefficient, peak flux, tail flux and source volume. (Although the Pouliquen coefficients are also positively correlated, the correlations are extremely weak, particularly for  $\mu_2$ ). These dependencies can also be rationalized by the model physics. Larger Chezy coefficients slow flows, which therefore must deepen to ensure conservation of mass. A larger source volume, delivered with higher peak fluxes, provides more material into the channel and therefore deeper flows. (Note also there are very weak negative correlations of the flow depths with the duration of the source.) Increases in fluid erosion rate will lead to increased bulking and therefore deeper flows. However, interestingly, the granular erosion rate has weak (and negative) correlation with the flow depths; this is not expected and may indicate that the fluid erosion always dominates the granular erosion term in the erosion parameterization, which could occur if the flows simulated have not become sufficiently concentrated in solids.

The correlation coefficients for the cross-section measurements are illustrated in Figure 40. As for the flow depths, the strongest correlations occur for the fluid erosion rate, Chezy coefficient, peak flux, tail flux and source volume, and there are systematic dependencies, but the strength of the correlations change with each location.

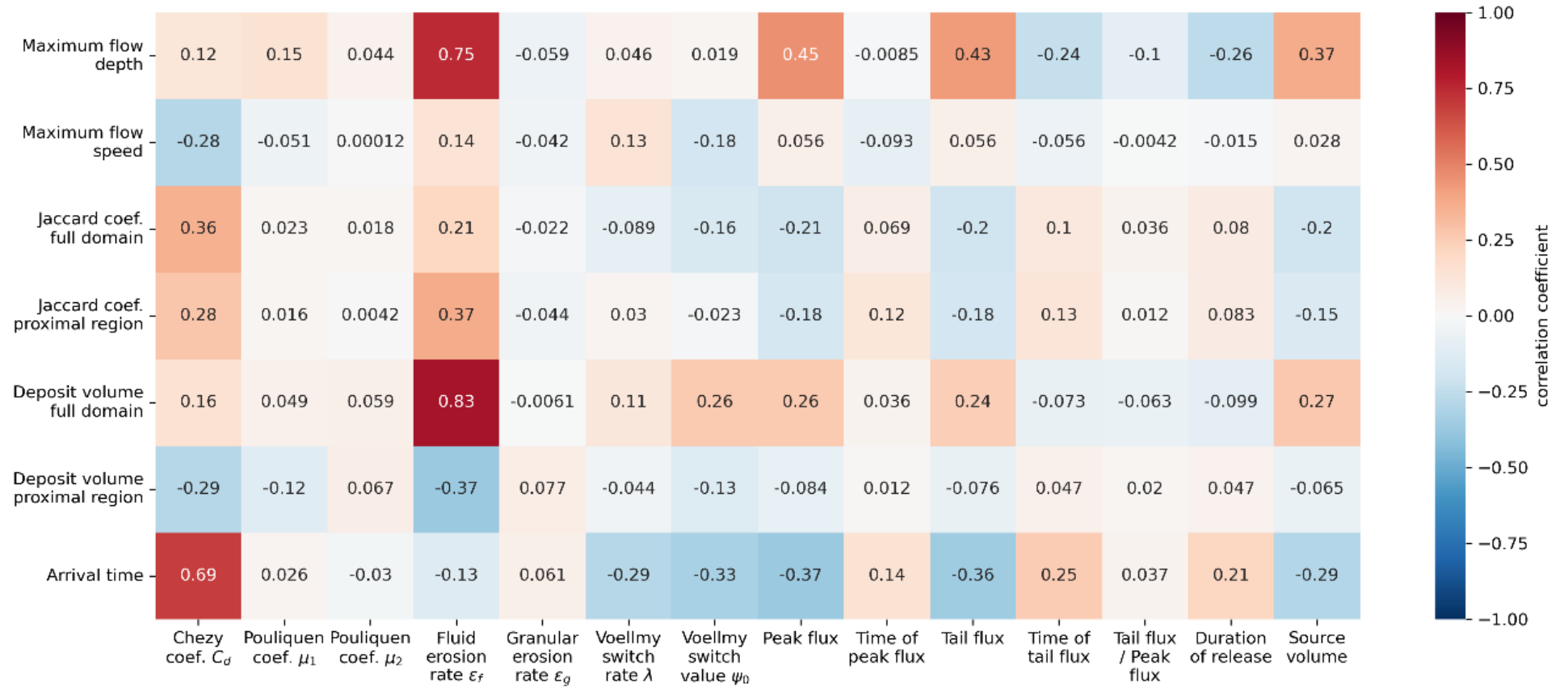


Figure 38. Correlation coefficients for aggregated and summary model outputs for each model and source parameter. Colour saturation denotes the strength of the correlation, with red and blue shades corresponding to positive and negative correlations respectively.



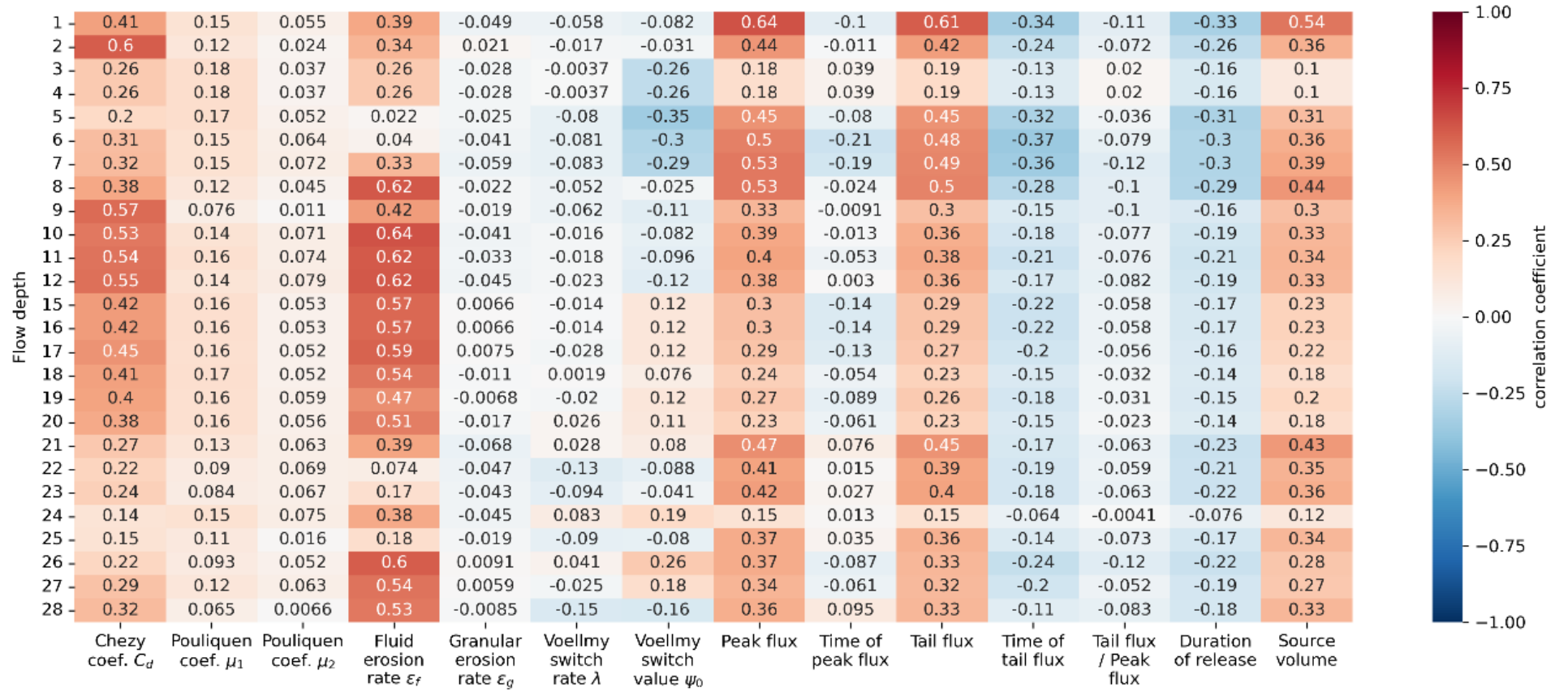


Figure 39. Correlation coefficients for punctual flow depth outputs at each observation point for each model and source parameter. Colour saturation denotes the strength of the correlation, with red and blue shades corresponding to positive and negative correlations respectively. Flow depth points are labelled as for the observations, as shown on Figure 32.



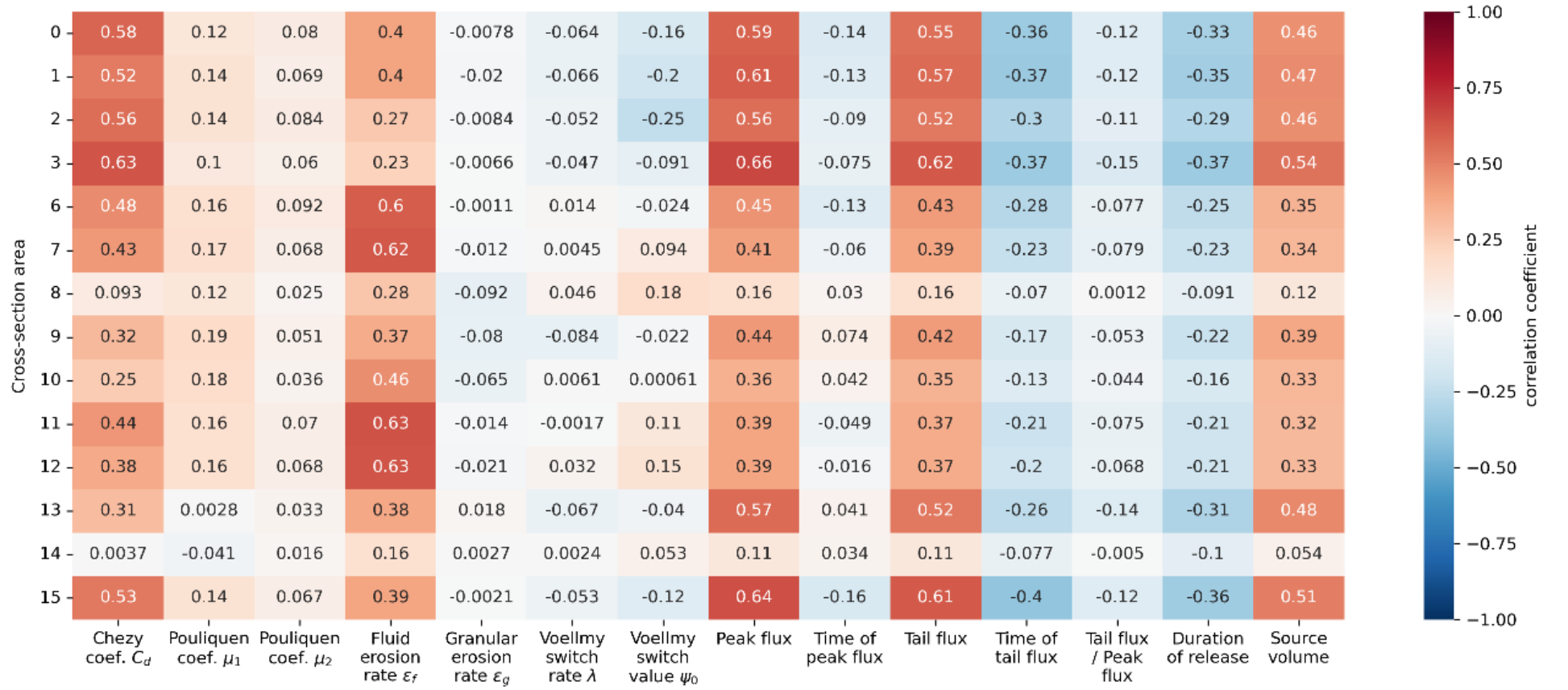


Figure 40. Correlation coefficients for punctual flow depth outputs at each observation point for each model and source parameter. Colour saturation denotes the strength of the correlation, with red and blue shades corresponding to positive and negative correlations respectively. Flow depth points are labelled as for the observations, as shown on Figure 33.

### 3.6.3 Determination of plausible parameter distributions

The implausibility scores for each ensemble member are computed for each model output and are used to identify and constrain ranges of parameters. An example is shown in Figure 41 as scatter plot for the implausibility score for the deposit volume in the full domain as a function of the fluid erosion rate. When looking at a single parameter and single output, we expect that there should be many plausible matches, as we have taken a cut through the dimension-12 hypercube of parameters. A small number of matches would indicate that a precise set of parameters is needed to produce a plausible simulation, which is very unlikely.

In Figure 41 there is a strong positive correlation, although scatter in the ensemble increases with the fluid erosion rate. The band of plausible scores contains many more parameter sets with relatively low values of the fluid erosion rate, although there remain a few plausible simulations with high values of this parameter. This indicates that, if the fluid erosion rate is constrained to low values, then the deposit observation can be reproduced by the model with relatively broad ranges of other parameters. In contrast, when large values of the fluid erosion rate are imposed, then a match to the deposit volume estimate can only be found with specific values of other parameters.

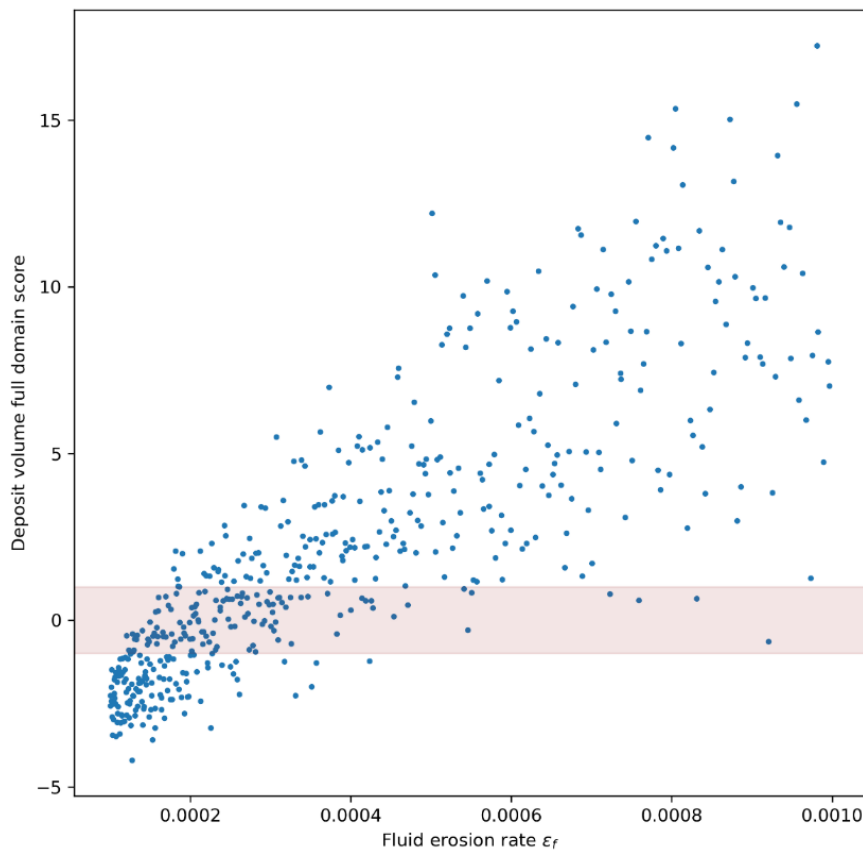


Figure 41. Scatter plot of the implausibility score for the deposit volume in the full domain as a function of the fluid erosion rate. The shaded band between  $\pm 1$  indicate the plausible range of the implausibility score.

An example is shown in Figure 42 where implausibility scores for the flow depth at measurement location 1 (Figure 32) and two source parameters (peak flux and tail flux). While the correlation of the model output is apparent, the implausibility score does not greatly constrain the range of the source parameter, with only modest increases in the lower bounds.

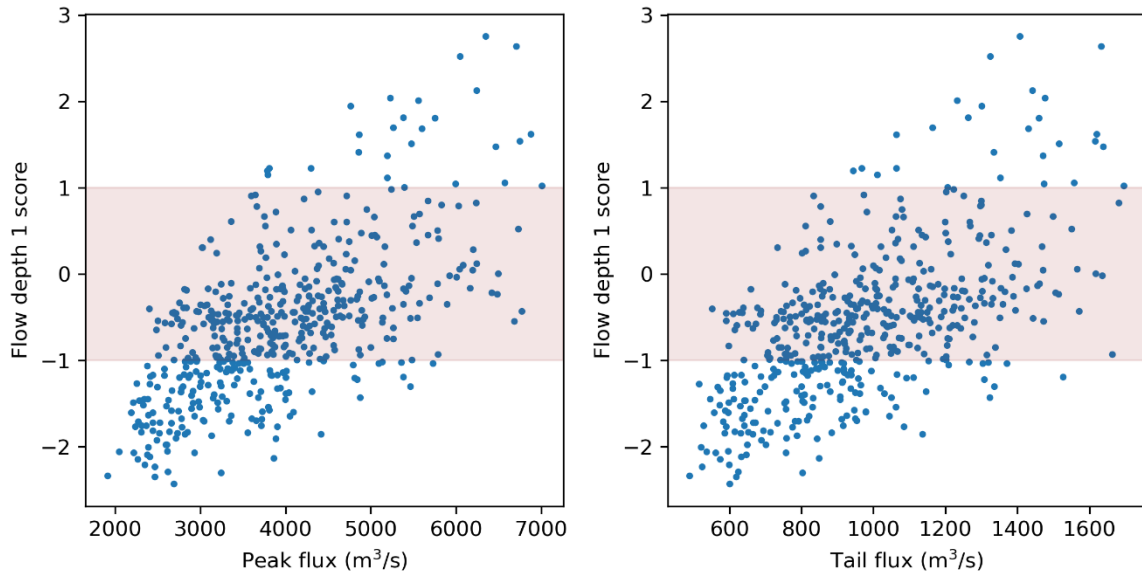


Figure 42. Scatter plots of the implausibility scores for flow depth measurement at location 1 for the peak flux and tail flux parameters. The shaded band between  $\pm 1$  indicate the plausible range of the implausibility score.

Figure 43 presents an interesting example, with the implausibility score for the flow depth at measurement location 2 as a function of the Chezy coefficient. Although the band of plausible outputs spans almost the prior range, a change in dependence of the parameters is apparent. For lower value of the Chezy coefficient, the model outputs collapse onto a curve, whereas at higher values there is considerable scatter in the data. The collapse of the data onto a curve at low values of the Chezy coefficient indicates that this parameter has dominant control on the flow depth at this location. The scatter that emerges for higher values of the Chezy coefficient indicate that other parameters (and therefore other physical processes) become influential in the modelled flow depth.

If we consider the implausibility measure for each output as a function of a single parameter, we can derive histograms of the parameter value that produce plausible matches. When plotted together, we can determine a constrained ranges for the parameter. An example is shown in Figure 44 for the fluid erosion rate, which we have identified as an active parameter for several model outputs.

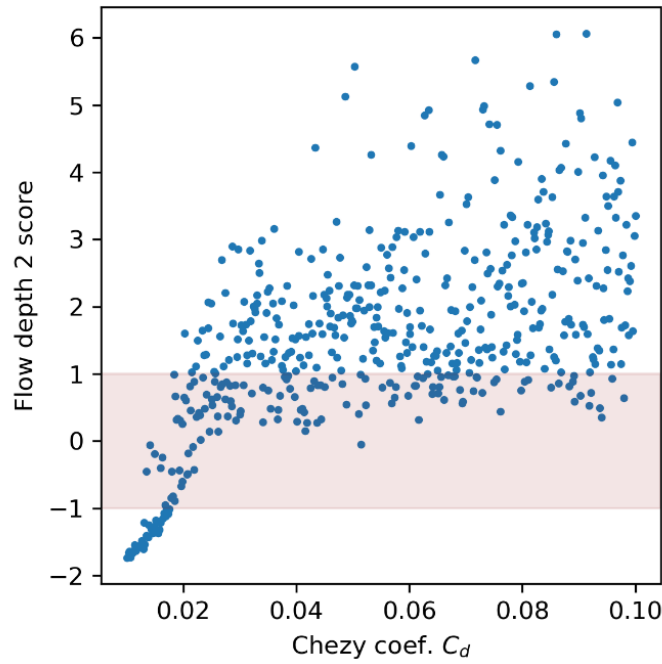


Figure 43. Scatter plot of the implausibility score for the flow depth as a function of the Chezy coefficient. The shaded band between  $\pm 1$  indicate the plausible range of the implausibility score.

In Figure 44 the distribution of values of the fluid erosion rate that give a plausible output are summarised using the minimum and maximum, and the 1<sup>st</sup>, 5<sup>th</sup>, 10<sup>th</sup>, 25<sup>th</sup>, 50<sup>th</sup> (median), 75<sup>th</sup>, 90<sup>th</sup>, 95<sup>th</sup>, and 99<sup>th</sup> percentiles. The plot therefore shows the range of plausible values for the fluid erosion rate for each output, as well as indicating the variance and skewness of the distribution. The number of plausible simulations in the ensemble varies for each output and this is indicated with the colour scale. While complicated, Figure 44 is useful as it encapsulates essential information on the distributions of plausible range of values for the input parameter (here fluid erosion rate) across all model outputs, allowing us to compare these distributions and determine ranges for the parameter that produce plausible matches to many of the observations.

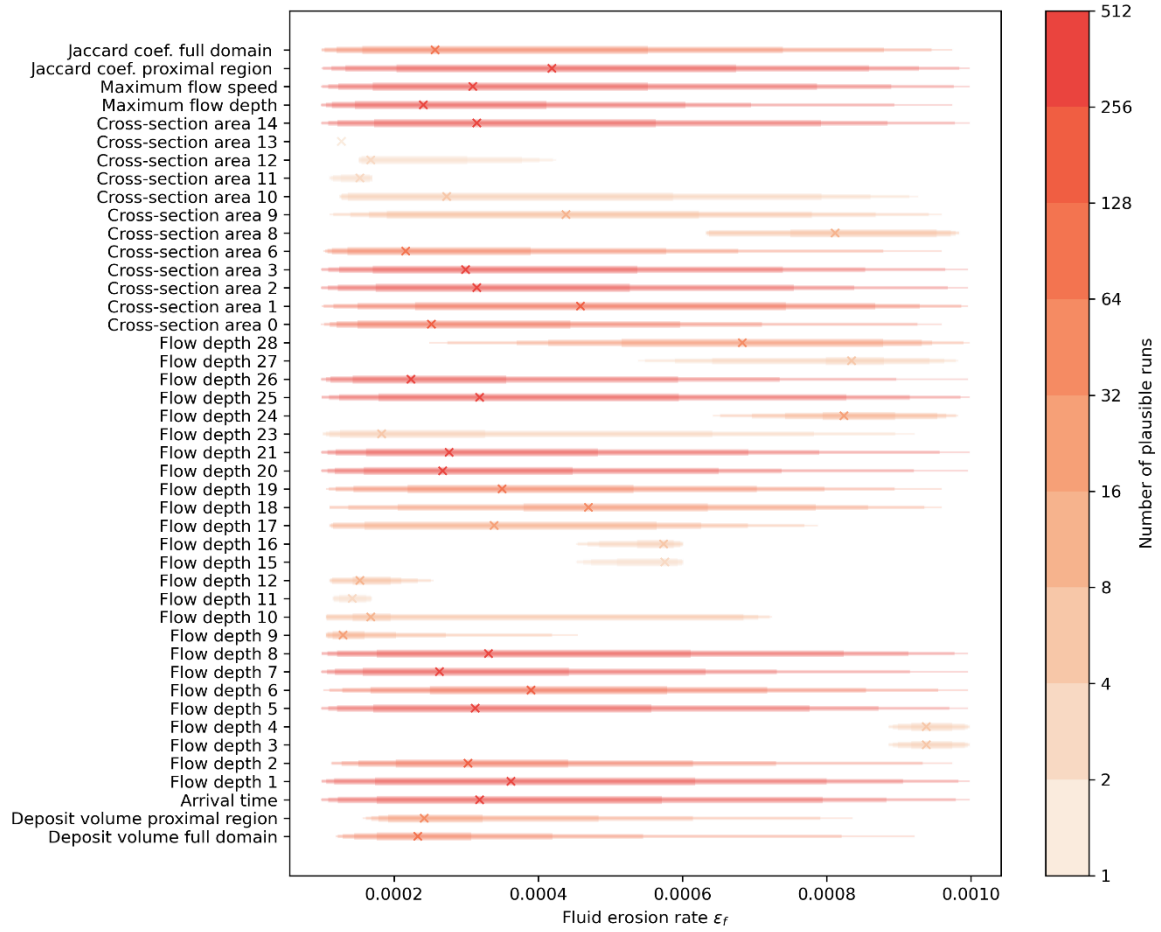


Figure 44. Distributions of the fluid erosion rate determined from the set of plausible matches to each of the observed quantities. The colour indicates the number of runs in the ensemble that produce a plausible match (and outputs with no plausible matches are excluded). The thickness of line indicates percentiles of the distribution, (with 1%, 5%, 10%, 25%, 75%, 90%, 95%, 99% taken, in addition to the minimum and maximum) and the cross indicates the median of the distribution.

Figure 44 shows that for several model outputs, the distribution of plausible values of the fluid erosion rate is skewed to relatively low values. While in many cases the range extends almost to the bounds of the prior distribution, the many outputs have median values close to the lower bound. We note that the prior distribution is uniform, and the Latin hypercube sampling is space filling. Therefore, we can conclude that several observations invoke a preference for lower values of the fluid erosion rate, and a range of  $1 \times 10^{-4}$ — $4 \times 10^{-4}$  is likely to provide model simulations that match many of the observations.

We can also see in Figure 44 some disjoint parameter ranges. For example, the flow depths at location 3 and 4 can only be reproduced in simulations with relatively high values of the fluid erosion rate, whereas the flow depths at locations 11 and 12 require low values. We note, however, that there are very few simulations in the ensemble that are able to predict these observations. This suggests that the model discrepancy in the implausibility measure for these outputs should be increased, and may correspond to errors in the DEM.



If we consider the granular erosion rate (Figure 45), we find a consistent preference for lower values of this parameter in order to reproduce a wide range of observations. However, we have previously identified that this is an inactive parameter for most outputs, and this has the consequence that the distribution of plausible values spans the prior range in most cases. Nevertheless, the skewing of the distribution to lower values suggests that constraining the range to 0.02–0.04 would be appropriate for further analysis.

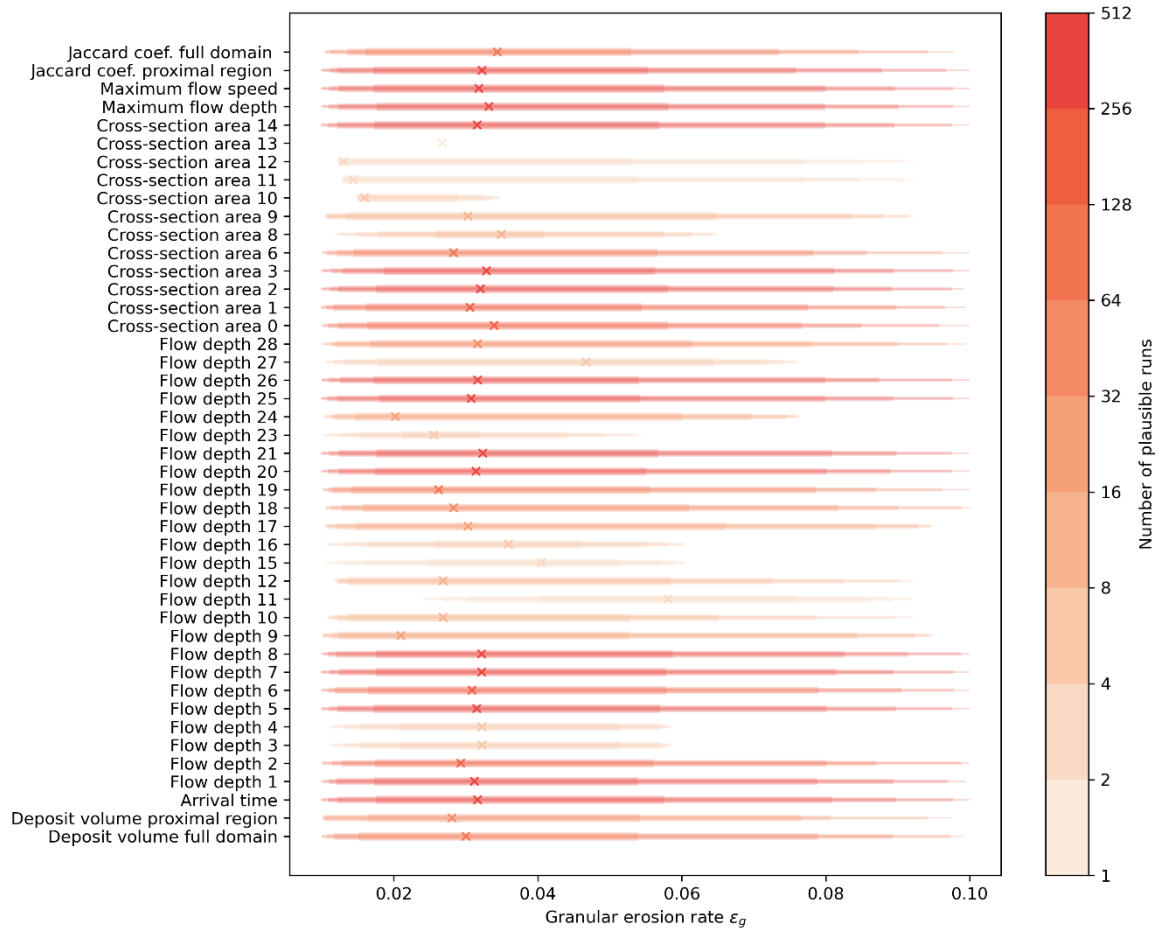


Figure 45. Distributions of the granular erosion rate determined from the set of plausible matches to each of the observed quantities. The colour indicates the number of runs in the ensemble that produce a plausible match (and outputs with no plausible matches are excluded). The thickness of line indicates percentiles of the distribution, (with 1%, 5%, 10%, 25%, 75%, 90%, 95%, 99% taken, in addition to the minimum and maximum) and the cross indicates the median of the distribution.

We have identified the Chezy coefficient as an active parameter for several outputs, and this results in a reduction of the parameter range when assessing against a single observation. However, when all outputs are considered together, there is not a clear pattern, as shown in Figure 46. This indicates that the Chezy coefficient cannot be usefully calibrated using the current ensemble.

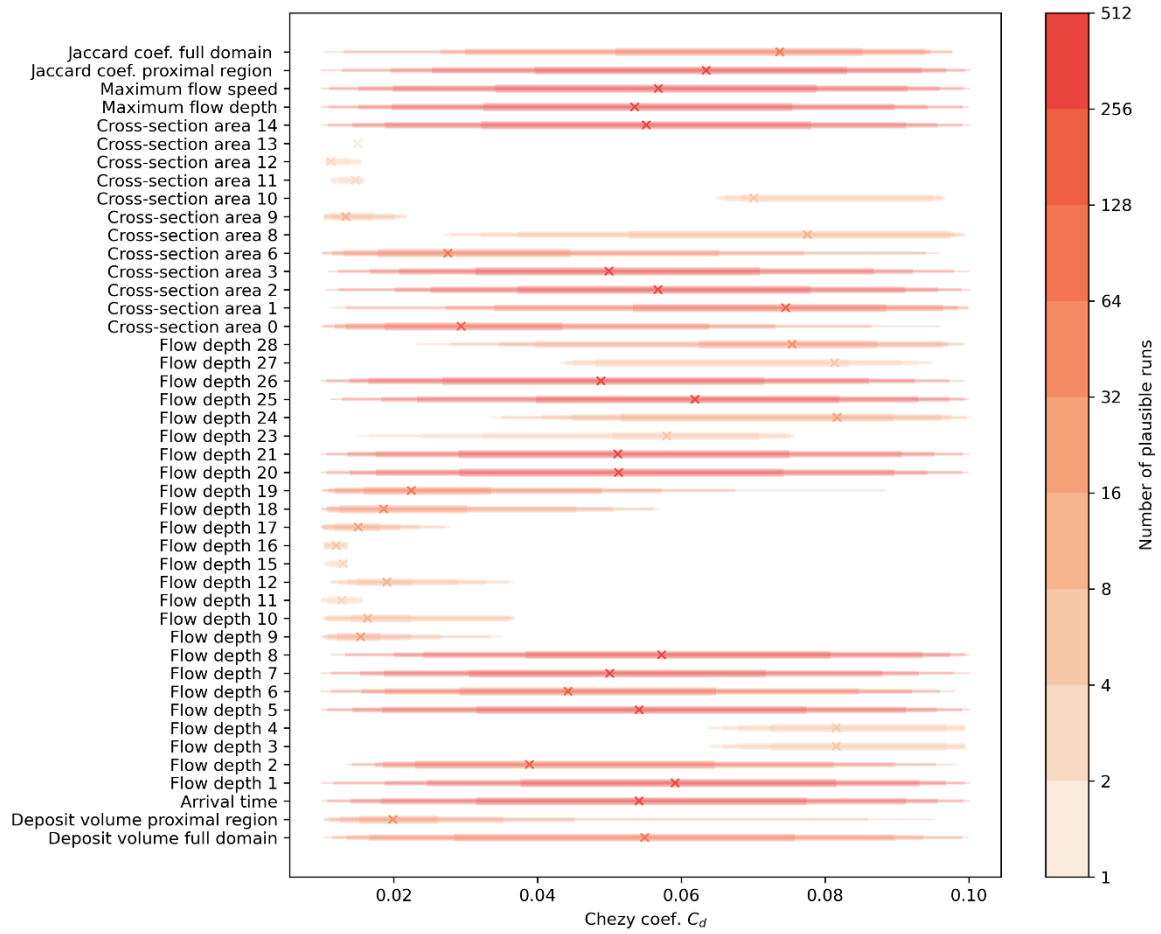


Figure 46. Distributions of the Chezy coefficient determined from the set of plausible matches to each of the observed quantities. The colour indicates the number of runs in the ensemble that produce a plausible match (and outputs with no plausible matches are excluded). The thickness of line indicates percentiles of the distribution, (with 1%, 5%, 10%, 25%, 75%, 90%, 95%, 99% taken, in addition to the minimum and maximum) and the cross indicates the median of the distribution.

Considering next the source parameters, the peak flux has some notable correlations with several outputs, and when considering the implausibility scores, the range of inputs is constrained (Figure 47). This suggests that the peak flux takes values in the range 3000—5000 m<sup>3</sup>s<sup>-1</sup>, although values outside this range cannot be precluded.

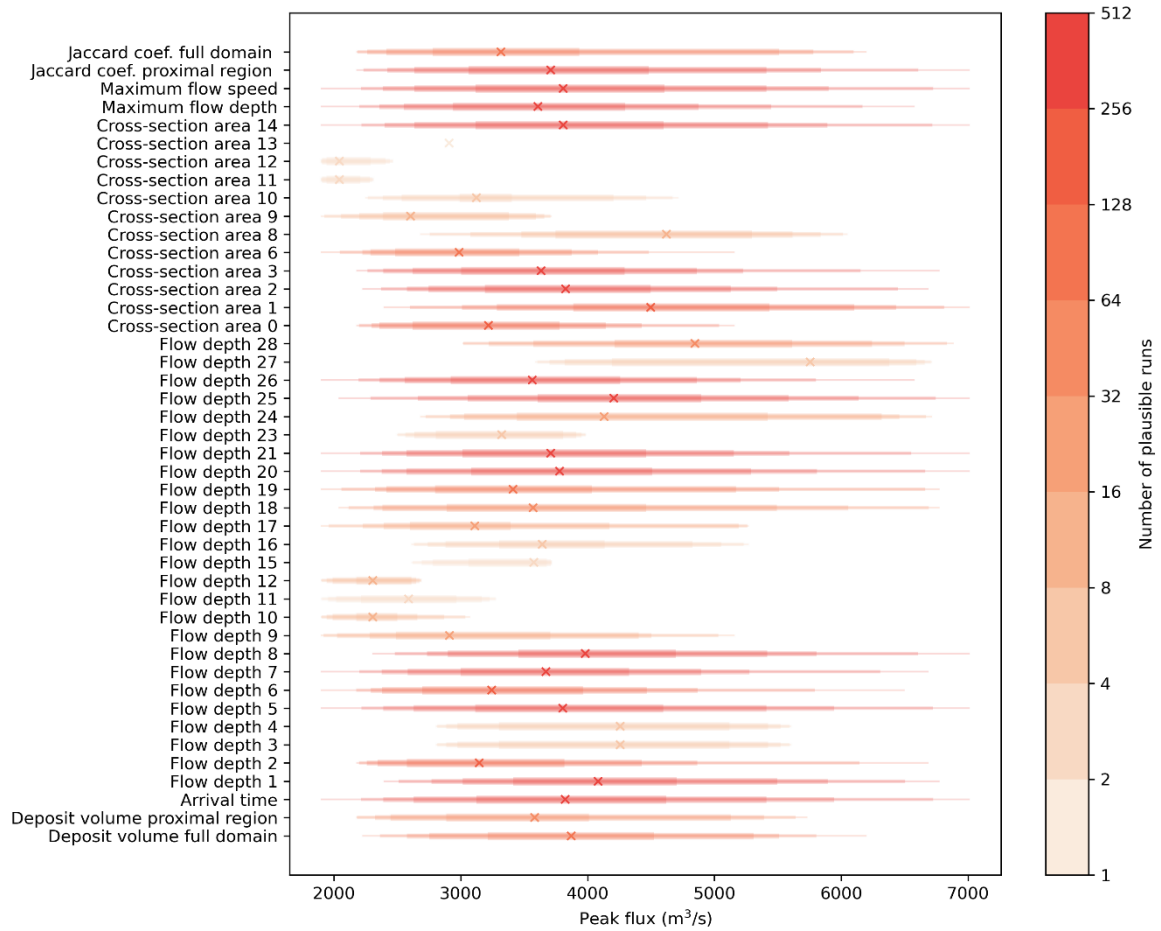


Figure 47. Distributions of the peak flux determined from the set of plausible matches to each of the observed quantities. The colour indicates the number of runs in the ensemble that produce a plausible match (and outputs with no plausible matches are excluded). The thickness of line indicates percentiles of the distribution, (with 1%, 5%, 10%, 25%, 75%, 90%, 95%, 99% taken, in addition to the minimum and maximum) and the cross indicates the median of the distribution.

### 3.6.4 Combined inundation map

From the subset of plausible simulations in the ensemble, we construct aggregated inundation maps. We consider two approaches to selecting plausible simulations from the ensemble. We could combine the *best* simulations from the ensemble, with some subjective criteria for selection. Alternatively, we could choose a particular model output of interest and combine those simulations from the ensemble that plausibly match this observation.

We first develop a subset of simulation that are best matches to observations in the sense that they are able to reproduce the most observations. We therefore take the 26 simulations from the 512 (i.e., 5% of the ensemble) that have the most plausible matches across all of the observations. This results in the combined map shown in Figure 48. The dominant flow routing appears clearly in the Rio Blanco and Rio Correntoso. There is less confidence in the extent of

the margins of the flow, particularly in the Rio Correntoso. It is also notable that the breakout flow in the source-proximal region occurs in only a small number of simulations in this subset.

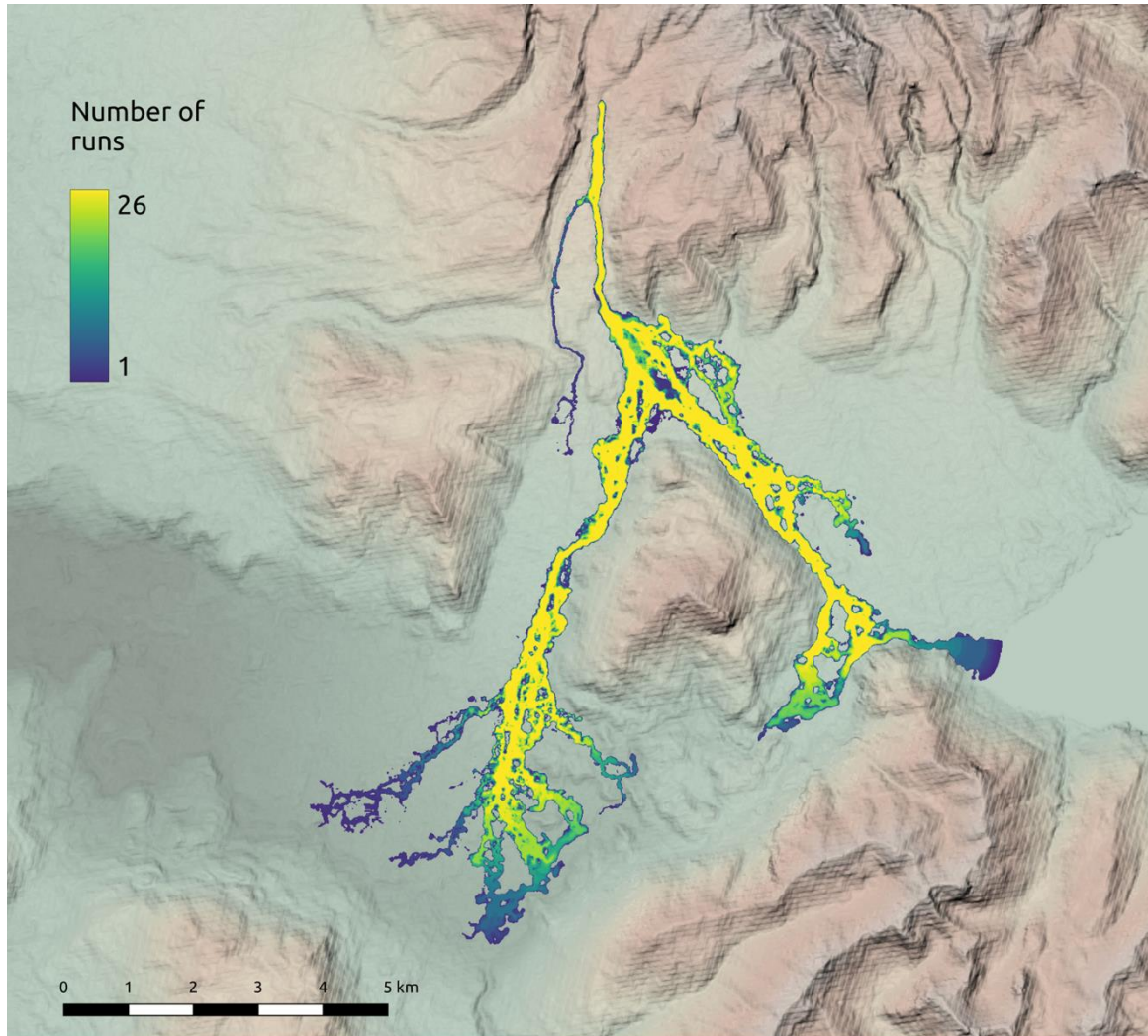


Figure 48. Combined inundation map from the 26 simulations that have the most plausible matches across all observations. The inundation is taken to be flow depths exceeding 10 cm. Colours represent the number of simulations that produce inundation at each location.

As a contrast, we consider the subset of the ensemble that give plausible matches only to the total deposit volume. We recall that the total deposit volume was strongly correlated with the fluid erosion rate (Figure 38) and is effective in constraining this parameter (Figure 44). The resulting combined inundation map is shown in Figure 48. Similarly to Figure 47, the prominent routing is selected, but there are subtle and important differences. In this case, the upper channel breakout occurs more frequently in the simulations. Additionally, there is generally a greater consistency in the routing, as more of the simulations in the subset overlap.



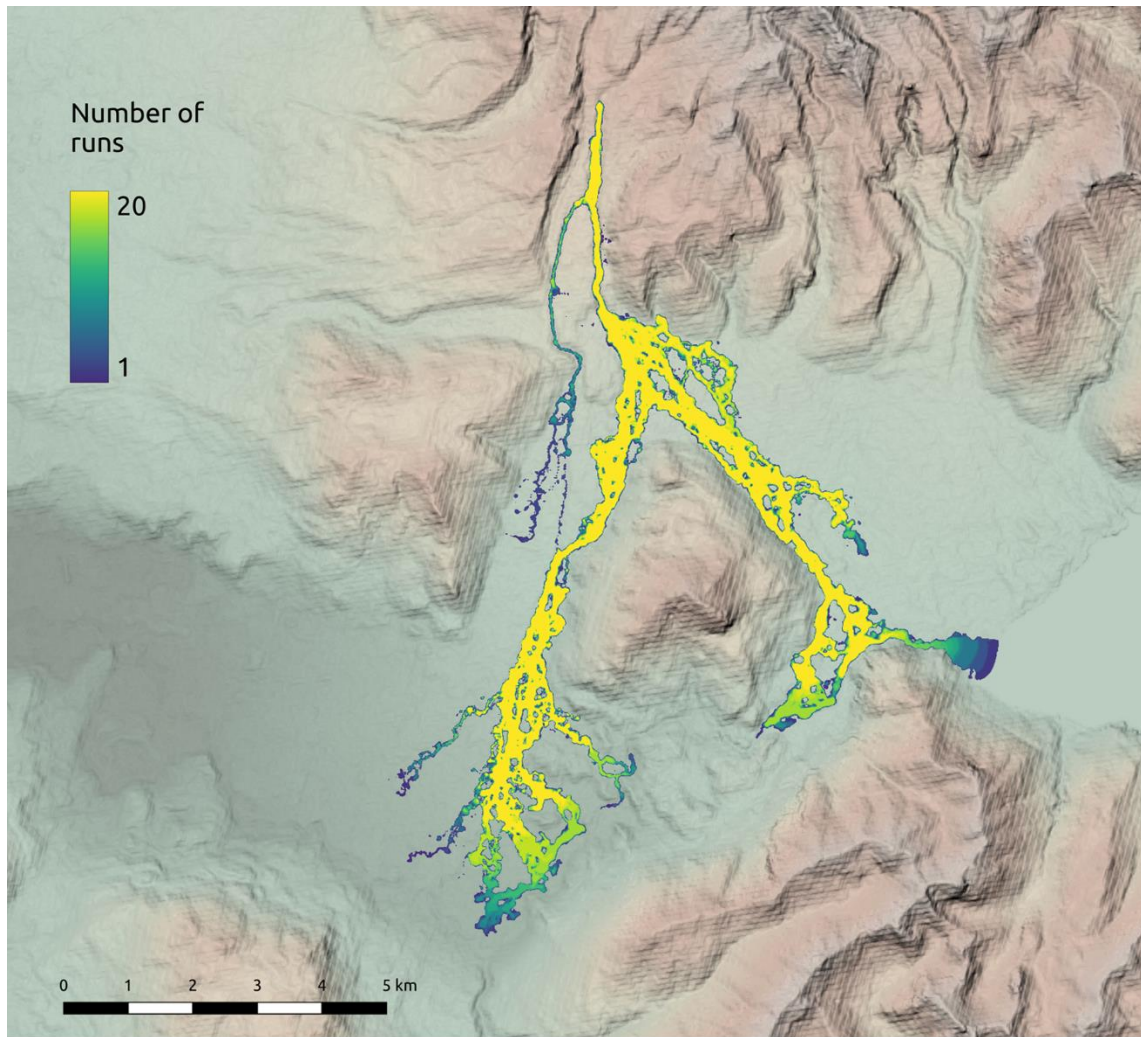


Figure 49. Combined inundation map from the 20 simulations that produce plausible matches to the total deposit volume. The inundation is taken to be flow depths exceeding 10 cm. Colours represent the number of simulations that produce inundation at each location.



## 3.7 Discussion

We have conducted a preliminary calibration of LaharFlow using a method that incorporates epistemic uncertainties in both the observations and the numerical model. As lahars are complex multiphase flows, mathematical models incorporate several linked physical processes that must be parameterized. As there is incomplete theoretical knowledge to provide model closures, LaharFlow adopts empirical relationships and parameters to represent physical processes. There are seven model parameters that must be specified in LaharFlow. In addition, the model source is an imperfect representation of the complex processes that lead to lahar flow initiation. Despite having constraints on the source of material that produced the lahars during the Calbuco eruption, the model source is highly uncertain, and the parameters of the source must also be calibrated. Here we have used a relatively simple source model, but this still leads five source parameters to be specified.

We therefore have a high-dimensional parameter space to explore. Even with 512 simulations, there is a very sparse exploration of parameter space. It is therefore unlikely that we could produce a well-calibrated model without a substantially larger ensemble. However, this preliminary analysis provides important insights into the model, the calibration data (and how it could be expanded), and the application of uncertain models for hazard assessment.

### 3.7.1 Calibration Data

Effective model calibration relies on appropriate observational data that can be compared directly with model predictions. In this study we have used our new field observations of the lahars generated by the Calbuco eruption to calibrate the LaharFlow model. The spatial extent of our observational data allows us to explore the evolution of the lahar from the proximal to the distal regions. Our observations (Chapter 2) show there are substantial changes in the lahar dynamics during the flow, and it is essential to capture these within a dynamic model.

Our analysis shows that using observational data of different types, and with good coverage over the flow areas, is beneficial in the model calibration process. Here we have used flow depth measurements at 28 locations, from proximal areas to the distal flood plain. We have used inundation extents from twelve field surveys of channel cross-sections, also spanning the flow path, including channel bifurcations. These data have been supplemented with data for the arrival time of the lahar at Chapo lake, and with aggregated data on the inundated area. Additionally, we have used an estimate of the volume of the deposits.

The different types of data are important as there are nonlinear couplings between processes in the model. These couplings mean that variations in one parameter can impact on several model predictions in a nonlinear manner. For example, changes to the drag parameters directly alter

the flow speed which, by mass conservation, alters the flows depth. Therefore, the flow depth measurements are an important constraint on the drag parameters. Additionally, the drag determines the basal stresses in the model, so affects the erosion and bulking of the flow. The eroded solid material is transported to regions where deposition dominates and produces deposits. Therefore, the drag parameters also effect the overall deposit volume predicted by the model. We might then expect that the flow depth measurements and deposit volume estimate would provide a comprehensive set of calibration data. However, there are other processes and parameters that affect each of the flow depth, speed and morphodynamic, resulting in a complex high-dimensional parameter space that is not easily calibrated.

Adding further observations would likely provide extremely valuable constraints. For example, building on the example above, if flow speed measurements were available at the locations where flow depths or cross-sections are measured, then these data would likely be powerful constraints on the model. While our field observations include discharge and velocity estimations, we made a choice not to include these data in the calibration. The estimated velocities are indirect measurements, derived from models that are not well-tested for lahars. The discharge data rely on the indirect velocity measurement. Indeed, there is a scarcity of direct dynamic information, given the limited availability of temporal data, only the arrival time of the lahar is known at a point ca. 14 km from the source of the lahar and with a relatively high range of error, specifically in the range of approximately 1 to 3 hours.

The source specification also plays a critical role in calibration but is often difficult to constrain. Our observations provide a total flow volume between  $4 \times 10^6 \text{ m}^3$  and  $8 \times 10^6 \text{ m}^3$ , derived from the volume of the glacier, which according to our analysis (Chapter 2) is the only source of water for lahar formation. However, this neglects addition of water during the flow, e.g. from tributaries of the main river channels.

We also note that the calibration approach can, and arguably should, be designed on the basis of the intended use of the model, and this has an important role in determining which data is most important for calibrating the model. For example, if we sought to use the model to design engineered mitigation structures, the dynamic variables such as momentum, dynamic and hydrostatic pressure, and bed stresses are likely to be essential outputs of the model. We would then seek measurements of these quantities or determine the processes in the model that most strongly effect these variables.

Alternatively, if the hazard model is intended to be used primarily to assess which areas are susceptible to inundation, then we would place a high weight on data such as the observed inundated areas (here seeking a Jaccard coefficient close to 1). However, we note in this case that the quality of the DEM is an essential component, as the topographic forcing often has a dominant effect on flow routing. Thus, uncertainties in the DEM, here considered a structural uncertainty in the model and included in our analysis through the model discrepancy, should be carefully quantified.

### 3.7.2 Uncertainties

The complexity of lahar dynamics means that there are many epistemic uncertainties in both the observational data used for calibration, and in the model formulation and application.

The uncertainties in directly observed and measured data, such as deposit and flow depths, are the ones that we might expect to best be most easily controlled and quantified, as naively, they derive from the limited accuracy of the instrument (usually a measuring tape with an accuracy of  $\pm 0.05$  cm). However, field observations can have interpretation bias and introduce uncertainties that are difficult to quantify. Orton (1996) cites numerous reasons why volcanic deposits are difficult to identify and interpret, such as (1) the existence of a wide variety of both eruptive and non-eruptive depositional processes that produce deposits of similar characteristics; (2) depositional processes commonly evolve over small periods and short distances, producing deposits with different characteristics that spatially overlap and grade into each other, showing great heterogeneity; (3) deposits are highly erodible and may be reworked relatively easily; (4) deposits are vulnerable to disturbance and burial by subsequent volcanic activity or other processes. Additionally, those deposits emplaced by secondary volcano-hydrological processes (debris avalanches, lahars and mudflows), or those emplaced by mountain glaciers on the slopes of volcanoes, can appear similar in outcrops (Pierson et al., 2017). This is relevant in the geological context of Calbuco, which is heavily influenced not only by volcanic processes, but also by glacial, fluvial and landslide processes (Selles & Moreno, 2011).

In addition, outcrops are restricted to discrete points in the terrain, usually at the side of fluvial incises or road cuts, so that thickness measurements are restricted to small samples of the deposit. For this reason, it is important to consider the geomorphology in the area of deposit emplacement to determine the valley or channel geometries in order to infer the contact of the deposits with the pre-settlement topography. In our study area, three types of valley or channel geometries could be identified: (1) semi-confined terraced channel (debris flow); (2) confined U-shaped channel; (3) unconfined floodplain channel.

Another important point for thickness measurements is the correct identification of the limits of the deposit (base and roof). In general, for the 2015 lahars at Calbuco volcano, it has been possible to identify the roof of the deposits with the occurrence of lateral levee-type morphologies and enrichment in pumice and blocks. Similarly, the bases are sometimes distinguished by vegetation, roots, by changes in the colour of the deposit, by a guiding component (e.g. anthropic debris), and sometimes by being in contact with lava or fluvial conglomerates (rounded and clastic supported).

Each of these challenges of field observation of a simple quantity such as depth of flow or deposit introduces uncertainty into the measurement. However, these uncertainties are difficult to quantify, and often rely on subjective decisions made by the observer. This indicates the importance of careful field work by experienced geologists in model calibration studies, to provide

insights into uncertainties of data than are not simply quantified. Additionally, there is an importance on incorporating unquantified uncertainties in the calibration process. This further supports the use of a model discrepancy term in a metric for assessing the model's predictive ability.

In contrast, medium to large scale observables such as maximum cross-sectional area of the flow, reservoir volume and inundated area can be measured with relatively good accuracy, which, considering the order of magnitude of their results, is sufficient to assume a relatively low error (see 2.4.2.2.).

Finally, another important source of uncertainty is the quality and resolution of the DEM, which determines how well the morphology of the valleys and channels is represented. Regarding the DEM used, it corresponds to Alos Palsar, which acquires the data through a Synthetic Aperture Radar (SAR) processed to obtain a corrected terrain model of 12.5 m resolution. Several studies have analysed the sensitivity of models for lahar hazard assessment in relation to the quality of elevation models (e.g., Stevens et al., 2002; Hubbard et al., 2007; Huggel et al., 2007; Muñoz - Salinas et al., 2009b) with results showing significant variations in flood areas when using different DEMs. This highlights the strong control by the topographic forcing in the model. For dense flows (such as lahars) the gravitational terms in the equations of motion often play a strong role in the dynamics. It is not possible to alter flow routing by changing model parameters if the topography is dominant in constraining the motion. Additionally, a DEM may not correctly represent the valley shape, which determines the filling or flooding capacity (Hubbard et al., 2007). Therefore, a good DEM quality (i.e. as accurate and precise as possible) at adequate resolution is essential to achieve an accurate model prediction. The appropriate DEM resolution depends on the scale of the channel, and on the shape of the valley through which the flow is to be modelled. A low-resolution DEM will not adequately represent the real channel or valley cross sections, overestimating the width of the flood zone, which could lead to an underestimation of the extent of the lahar (Muñoz - Salinas et al., 2009b).

Artefacts in DEMs can also have a limiting impact on the flow simulations. The Alos Pulsar DEM suffers from a periodic 'striping' artefact in the elevation data that, while of low amplitude so that flow routing is not noticeably affected, is sufficient to introduce topographic variations that are likely to influence the flow dynamics. This may be through altering erosion and deposition zones, for example. We again must consider these as contributing to an overall model discrepancy, limiting the predictive capability of the flow model.

The calibration of model is therefore conditional on the DEM used. We cannot expect to determine 'universal' parameters from a calibration on the Alos Pulsar DEM that can be used on a different topographic map.

### 3.7.3 Results of simulations

Despite the challenges of calibration, we have demonstrated that LaharFlow is a useful model to simulate the lahars of the 2015 eruption of the Calbuco volcano. In particular, the model can, for example, represent in a general way, the main areas of deposition and erosion observed on the ground (Figure 37). Also, the predicted inundation areas provide a reasonable match to observations, considering that the limitations of the DEM that we use. The model discrepancy could be reduced by using a better-quality digital elevation model, which can more accurately represent the dimensions of the channels. However, this should be tensioned with the additional computational time require to simulate at high-resolution on a fine-scale DEM, which may make application of the model for hazard assessment during a crisis challenging.

The model also provides an estimation of the peak discharge and volume of the flow. In the case of peak discharge, the modelling suggests a source value in the range 3000—5000 m<sup>3</sup> s<sup>-1</sup>. This is consistent with the values estimated from the field work cross-sections (Table 4 and Figure 26). We note the discharge measurements are based on the area-velocity method, and in most cases the velocity has been estimated with the Manning equation, with a roughness coefficient estimated by comparison with velocities measured in other locations with alternative methods (see 2.4.2.2). Therefore, the discharge data are highly uncertain and should be considered order-of-magnitude estimates to determine the trends along the flow.

Finally, the results observed for other variables such as solid concentration show some inconsistency with respect to what is inferred from the facies observed in the deposits, while the velocity is generally lower than expected in comparison to other lahars in the world (e.g. Pierson, 1995; Worni et al. 2012; Johnson & Palma, 2015).

### 3.7.4 Model limitations and implementation

As with all physical models, LaharFlow is a simplified representation of the complex flow. There are numerous approximations and modelling decisions used to produce a tractable model. These together contribute to the structural uncertainty in the model, which are not easily quantified.

Our model is implemented with a circular release area, which is not a good representation of a natural flow. However, as previously discussed, this mainly affects the source area so care should be taken to locate the source area upstream of the area of interest to avoid the effects in locations of interest. There are several alternative source specifications that could be implement in a future development of the model, for example releases as a line source. However, given the complex lahar initiation conditions that we have proposed (Chapter 2), it may be necessary to integrate multiple models to capture the pyroclastic density currents, glacial collapse, and transitional flows that develop into lahars.

Another implementation that could be tested in future modelling and simulation exercises is the definition of simulation domains with spatially varying flow parameters to model changes in terrain



and geology such as bedrock characteristics. For example, in the case of Calbuco, two domains are clearly distinguishable: the volcanic edifice zone, where numerous lava flows outcrop and valleys tend to be confined with moderate to high slope channels, and the zone outside the volcanic edifice where the characteristics are strongly influenced by the hydrology and fluvial systems of the wide flood plains. These zones have marked differences in lithology and geomorphology that could affect permeability, erodible layer depth and erosion rates, as well as different land cover that will affect the drag characteristics of the flow.

It is important to emphasize that the calibration is likely to be strongly case-specific. A calibrated lahar model cannot necessarily be applied directly to any lahar at any volcano, and caution should be applied in the interpretation of results for a model used away from its calibration conditions. The fundamental reason is the wide variety of existing volcanic and sedimentary environments, so some criteria for discriminating lahars that can be considered analogous should be considered. Vallance (2000) proposes a classification between cohesive and non-cohesive lahars according to the proportion of fines. A similar distinction has been presented by Castruccio et al. (2009) when comparing lahars from the Calbuco volcano in the Tepu river in 1961 with those at Villarrica volcano in the Chaillupén valley in 1971. Therefore, suitable criteria to discriminate cohesive or non-cohesive lahars without knowing in detail the fines content, could be useful to compare the factors that influence the fines content. Here we propose four factors:

- (1) the composition, volatile content and physical properties of the erupted magmas could have some influence on magmatic fragmentation and the consequent formation of fine to very fine ash (Cashman & Scheu, 2015);
- (2) the presence of glaciers and/or hydrothermal alteration that could favour the formation of clays (Pierson, 1995, Vallance & Iverson, 2015);
- (3) climate, latitude and eruptive frequency, as factors influencing weathering and soil formation;
- (4) the lithology of the lahar emplacement area.

Moreover, geomorphology and lithology could influence parameters such as permeability and erosion rate, as well as the type and size-distribution of sediment available for eroding, for example, when moraines are present or the morphologies of channels. Another factor that we consider important to assess the transferable application of a model is the eruptive style and hydrological conditions as they may control the mechanism of lahar generation.

### 3.7.5 Use the model as a tool for hazard assessment.

In the last decade, several studies have attempted to standardise the principles of volcanic hazard assessment (e.g. Bignami et al. 2013; Calder et al. 2015), which has traditionally relied heavily on geological mapping (Clive et al. 2017; Ogburn et al., 2023). Taking as an example, the case

of hazard map produced in Chile, as published by Sernageomin (e.g. Bertin et al., 2022) the hazard assessment comprises three elements: (1) determining the areas or location of the process or hazard; (2) understanding how intense or severe the hazard is; and (3) knowing how often the process or hazard occurs.

Element (1) can be understood as the spatial susceptibility (Bignami et al. 2013) and refers to "where" the process will occur for a given scenario. The application of the lahar model for this purpose is straightforward, as the model predicts an inundated area. However, taking a single, fixed parameter set is not appropriate, as this does not incorporate the many epistemic uncertainties that are implicit in a calibrated model. We suggest instead to use ensemble simulation with ranges of values at least for the active parameters and for variations in source conditions to capture some of the aleatoric uncertainties in the modelled scenario. We have demonstrated this approach using our ensemble simulations, that produce useful predictions (Figures 48 and 49). This is similar to a probabilistic modelling approach, which is more challenging as it requires specification of probability distributions on uncertain inputs. The ensemble modelling must be complemented with geological mapping of past deposits and local knowledge as multiple situations or conditions, complex to model, may occur, such as the interaction of the flow with forests and the incorporation of logs that could form dams. Similarly, we recommend the use of high resolution digital terrain models ( $< 5\text{m}$ ), and where this is not possible, to establish some method to incorporate the uncertainty in the topography, such as simulating over multiple DTMs.

The model also contributes to the understanding of how severe or intense the hazard is (element 2) which attempts to answer the question of "how" the hazard is experienced. A concept that has started to be used in recent hazard assessment literature (Bignami et al. 2013; Wilson et al. 2017) distinguishes the hazard between processes that may have equal recurrence but different impact, e.g. a pyroclastic flow is capable of burning, but a lahar typically is not. This concept is mainly based on the physical variables that are relevant for the exposed elements, such as temperature, burial capacity (density), velocity, among others. Here, Laharflow could for example be implemented to determine velocity and momentum at exposed locations under different scenarios. Additionally, with a good calibration including dynamic (temporal) data, for example, lahar arrival time curves could be established, which would contribute relevant information for emergency response or evacuation plans.

Finally, on element (3), related to the recurrence of the process and the question of "when" it will occur. This is a variable that is outside the scope of a physical flow model, and instead relies on geological knowledge of the volcano and its deposits. In hazard assessments it is common to establish magnitude-frequency matrices or tables where processes of a certain magnitude are grouped together, e.g. lahars of  $1\text{-}5 \times 10^6 \text{ m}^3$ , lahars of  $> 10^6 \text{ m}^3$  and assigned a frequency factor determined by the eruptive chronology or the observed statistics of their deposits. These magnitude-frequency relationships should be derived in the modelling scenarios that the models simulate.

## 4 Conclusion

The Calbuco volcanic eruption of 2015 was a complex event, characterized by two explosive phases with partial and major column collapses. The resulting pyroclastic density currents propagated over fractured and unstable glaciers, that collapsed and provided a large source of water which mixed with the pyroclastic materials. This triggered lahars in many of the channels on the flanks of the volcano. Multiple large lahar flows descended the southern flank of the volcano, causing damage and destruction in populated areas around the volcano, though thankfully no deaths.

Using a multi parameter data set, including social media, reports of authoritative institutions, instrumental monitoring data and published scientific reports, we have determined a detailed chronology of the eruption and the resulting volcanic flows, with a focus on the primary lahars in the southern valleys. We have shown that lahars in the Amarillo river began during the first phase of the eruption due to the sustained emplacement of pyroclastic flows in its catchment. In contrast, our observations suggest that the lahars in the Blanco – Correntoso river system and the Este river were likely to have been triggered by a sudden mechanical collapse of the glacier that triggered mixed avalanches which transitioned into lahars as they propagated downstream.

Extensive post eruption field surveys in the Blanco – Correntoso and Este – Amarillo river systems have gathered data which we have analysed to characterize the dynamics of the lahars produced during the eruption. These observations include inundation cross-sections, estimates of flow speeds, and characterization of the morphology and componentry of flow facies, and complement existing observation data sets such as instrumental records from gauge stations along the channels. Our analysis shows evidence of transitions in flow rheology and composition, as well as the changing erosional and depositional character of the flow.

We have used the observational dataset we have compiled to perform a first phase calibration of a LaharFlow, dynamic, physics-based model of lahar dynamics. We have modelled flows in the Blanco – Correntoso river system and explored the influence of the model parameters on flow predictions in an ensemble of simulations. Our calibration process accounts for the substantial epistemic uncertainties in our observations and the model formulation, including a model discrepancy term that encapsulates structural uncertainties that are difficult to quantify individually. We determine plausible ranges for the model parameters, including those representing the lahar source. While our ensemble is too small to confidently prescribe parameter values, our approach highlights those parameters in the model that have a dominant effect on the predictive capability of the simulations. The result indicate that further development of the model source would be useful to improve model predictions and show that additional observations of dynamic quantities would be valuable further constrains on calibration. Despite the limitations of the calibration, we have illustrated that an ensemble approach based on assessing plausibility of the simulations using observations can provide important hazard information. By combining

plausible simulation results, we have produced combined flow inundation maps that encompass the combined uncertainties in our calibration. This approach may have value in situations where detailed calibration data is not available, or during a crisis where a comprehensive calibration study is impractical.

## 5 References

- @carlitadegaby (2015), April 23<sup>rd</sup>. Available: <https://twitter.com/carlitadegaby/status/591296624162373634> (Accessed 27/04/2022).
- @GobiernodeChile (2015), April 22<sup>nd</sup>. Available: [https://twitter.com/GobiernodeChile/status/591012729974083584?ref\\_src=twsrc%5Etfw%7Ctwcamp%5Etweetembed%7Ctwterm%5E591012729974083584%7Ctwgr%5E%7Ctwcon%5Es1&ref\\_url=https%3A%2F%2Fcooperativa.cl%2Fnoticias%2Fpais%2Fdesastres-naturales%2Ferupciones-volcanicas%2Fla-erupcion-del-volcan-calbuco%2F2015-04-22%2F183646.html](https://twitter.com/GobiernodeChile/status/591012729974083584?ref_src=twsrc%5Etfw%7Ctwcamp%5Etweetembed%7Ctwterm%5E591012729974083584%7Ctwgr%5E%7Ctwcon%5Es1&ref_url=https%3A%2F%2Fcooperativa.cl%2Fnoticias%2Fpais%2Fdesastres-naturales%2Ferupciones-volcanicas%2Fla-erupcion-del-volcan-calbuco%2F2015-04-22%2F183646.html) (Accessed 26/04/2022).
- @grandepatagonia (2015), April 23<sup>rd</sup>. Available: <https://twitter.com/grandepatagonia/status/591273429065662465>. (Accessed 27/04/2022).
- @latercera (2015), April 23<sup>rd</sup>. Available: <https://twitter.com/latercera/status/591271468195000320>. (Accessed 27/04/2022).
- @mop\_chile (2015a), April 23<sup>rd</sup>. Available: [https://twitter.com/mop\\_chile/status/591225249926144000](https://twitter.com/mop_chile/status/591225249926144000) (Accessed 27/04/2022).
- @mop\_chile (2015b), April 23<sup>rd</sup>. Available: [https://twitter.com/mop\\_chile/status/591246538170638336](https://twitter.com/mop_chile/status/591246538170638336) (Accessed 27/04/2022).
- @mop\_chile (2015c), April 23<sup>rd</sup>. Available: [https://twitter.com/mop\\_chile/status/591366462801108992](https://twitter.com/mop_chile/status/591366462801108992) (Accessed 27/04/2022).
- @munipuertomontt (2015), April 22<sup>nd</sup>. Available: <https://twitter.com/munipuertomontt/status/591024389640052736> (Accessed 26/04/2022).
- @CBPMO (2015), April 22<sup>nd</sup>. Available at: <https://twitter.com/CBPMO/status/591063306464600065> (Accessed 26/04/2022).
- @ptomontt\_histor (2015), April 23<sup>rd</sup>. Available at: [https://twitter.com/ptomontt\\_histor/status/591305377033117698](https://twitter.com/ptomontt_histor/status/591305377033117698) (Accessed 27/04/2022).
- @vdj\_ivan\_beroiz (2015), April 23<sup>rd</sup>. Available at: [https://twitter.com/vdj\\_ivan\\_beroiz/status/591215207717986305](https://twitter.com/vdj_ivan_beroiz/status/591215207717986305) (Accessed 27/04/2022).
- 24horas.cl (2015). 24 Horas Central - miércoles 22 de abril | 24 Horas TVN Chile. Available from: <https://www.youtube.com/watch?v=QI8CabSyy00&t=3103s> (Accessed 18/04/2022).
- Alletto75 (2015) April 22<sup>nd</sup>. Available at: <https://twitter.com/aletto75/status/591038155408695296>



- (Accessed 26/04/2022).
- Almonacid, Darío (2015). 2 Timelapse Calbuco Chile 2015 HD / Erupción volcán / Eruption volcano / Извержение вулкана / 火山噴發. Available from: <https://www.youtube.com/watch?v=ljrDn3Gel4M> (Accessed 14/06/2021).
- Andaru, R., Rau, J.Y., Kamil Syahbana, D., Setya Prayoga, A., Desi Purnamasari, H. (2021). The use of UAV remote sensing for observing lava dome emplacement and areas of potential lahar hazards: An example from the 2017–2019 eruption crisis at Mount Agung in Bali. *Journal of Volcanology and Geothermal Research*. V. 415, 107255.
- Arcement, G J. & Schneider, V.R. (1989). Guide for selecting Manning's roughness coefficients for natural channels and flood plains. Water-supply paper 2339. United States Geological Survey, 1989.
- Arel Silva, Egon (2015) April 15th. Available at: <https://twitter.com/ArelEgon/status/588327515581767680> (Accessed 19/03/2022).
- Arzilli, Fabio & Morgavi, Daniele & Petrelli, Maurizio & Polacci, Margherita & Burton, Mike & Di Genova, Danilo & Spina, Laura & La Spina, Giuseppe & Hartley, Margaret & Romero, Jorge & Fellowes, Jonathan & Díaz Alvarado, Juan & Perugini, Diego. (2019). The unexpected explosive sub-Plinian eruption of Calbuco volcano (22–23 April 2015; southern Chile): Triggering mechanism implications. *Journal of Volcanology and Geothermal Research*. 378. 35-50. 10.1016/j.jvolgeores.2019.04.006.
- Aster, Richard & Borchers, Brian & Thurber, Clifford. (2013). Parameter Estimation and Inverse Problems. 10.1016/C2009-0-61134-X.
- Auker, M. R., Sparks, R. S. J., Siebert, L., Crosweller, H. S., & Ewert, J. (2013). A statistical analysis of the global historical volcanic fatalities record. *Journal of Applied Volcanology*, 2(1), 1-24.
- Bacigalupe, G., Velasco, J., Rosenberg, A., & Berrios, P. (2016). Medios sociales en la emergencia: Evidencia y recomendaciones para la gestión de desastres. Santiago, Chile: Centro de Investigación para la Gestión Integrada del Riesgo de Desastres (CIGIDEN). ISBN: 978-0-9984579-0-1
- Benet, Damià & Costa, Fidel & Pedreros, Gabriela & Cardona, Carlos. (2021). The volcanic ash record of shallow magma intrusion and dome emplacement at Nevados de Chillán Volcanic complex, Chile. *Journal of Volcanology and Geothermal Research*. 417. 107308. 10.1016/j.jvolgeores.2021.107308.
- Bertin, L.; Jara, G.; Toloza, V. 2022. Peligros del volcán Parinacota, región de Arica y Parinacota. Servicio Nacional de Geología y Minería, Carta Geológica de Chile, Serie Geología Ambiental 40: 76 p., 1 mapa escala 1:50.000. Santiago.

- Bignami, Christian & Bosi, Vittorio & Costantini, Licia & Cristiani, Chiara & Lavigne, Franck & Thierry, Pierre. (2013). Handbook for Volcanic Risk Management: an outcome from MIAVITA project. 10709-.
- Biobiochile.cl (2015). FOTOS: Carabineros sobrevuela cercanías del cráter del volcán Calbuco. Available from: <https://www.biobiochile.cl/noticias/2015/04/22/carabineros-sobrevuela-volcan-calbuco-para-monitorear-la-zona-afectada.shtml> (Accessed 15/06/2021).
- Bonadonna C, R. Genco, M. Gouhier, M. Pistolesi, R. Cioni, F. Alfano, A. Hoskuldsson, M. Ripepe. (2011) Tephra sedimentation during the 2010 Eyjafjallajökull eruption (Iceland) from deposit, radar, and satellite observations. J. Geophys. Res. Solid Earth. 2011;116:B12202. doi: 10.1029/2011JB008462
- Breard, Eric & Calder, Eliza & Ruth, Dawn. (2020). The interaction between concentrated pyroclastic density currents and snow: a case study from the 2008 mixed-avalanche from Volcán Llaima (Chile). Bulletin of Volcanology. 82. 10.1007/s00445-020-01413-4.
- Bravo, Jael (2015). Primeros minutos de la erupción del Volcán Calbuco HD. Available from: <https://www.youtube.com/watch?v=poszhxeYyrM> (Accessed 15/06/2021)
- Brown, S.K., Jenkins, S.F., Sparks, R.S.J., Odbert, H., Auken, M.R. (2017) Volcanic fatalities database: analysis of volcanic threat with distance and victim classification. Journal of Applied Volcanology, 6:15. Version 1.0
- Blott, Simon & Pye, Kenneth. (2001). GRADISTAT: A grain size distribution and statistics package for the analysis of unconsolidated sediments. Earth Surface Processes and Landforms. 26. 1237 - 1248. 10.1002/esp.261.
- Blott, Simon & Pye, Kenneth. (2012). Particle size scales and classification of sediment types based on particle size distributions: Review and recommended procedures. Sedimentology. 59. 2071–2096.
- Bono, L., Amigo, A. 2015 Modelamiento de los lahares ocurridos en el volcán Calbuco 2015 con el software RAMMS. Congreso Geológico Chileno, No. XIV, La Serena, Chile.
- Bower, R. G., Goldstein, M., & Vernon, I. (2010) Galaxy formation: a Bayesian uncertainty analysis, Bayesian Analysis, 5(4), 619-669. doi: 10.1214/10-BA524
- Branney, M. & Gilbert, J. (1995). Ice-melt collapse pits and associated features in the 1991 lahar deposits of Volcán Hudson, Chile: criteria to distinguish eruption-induced glacier melt. Bulletin of Volcanology - BULL VOLCANOL. 57. 293-302. 10.1007/s004450050095.
- Brater, Ernest F.; King, Horace W.; Lindell, James E.; Wei, C. Y. 1996. Handbook of Hydraulics for the solution of Hydraulic Engineering Problems. Seventh Edition. McGraw-Hill Education.

- Brown, Richard J.; Graham D. M. Andrews, (2015). Deposits of Pyroclastic Density Currents, Editor(s): Haraldur Sigurdsson, The Encyclopedia of Volcanoes (Second Edition), Academic Press, 2015, Pages 631-648, ISBN 9780123859389, <https://doi.org/10.1016/B978-0-12-385938-9.00036-5>.
- Brown, S. K., Jenkins, S. F., Sparks, R. S. J., Odbert, H., & Auker, M. R. (2017). Volcanic fatalities database: analysis of volcanic threat with distance and victim classification. *Journal of Applied Volcanology*, 6(1), 1-20.
- Caballero, L. & Capra, L. (2014) The use of FLO2D numerical code in lahar hazard evaluation at Popocatepetl volcano: a 2001 lahar scenario, *Nat. Hazards Earth Syst. Sci.*, 14, 3345–3355, <https://doi.org/10.5194/nhess-14-3345-2014>
- Calder, E. S., Cole, P. D., Dade, W. B., Druitt, T. H., Hoblitt, R. P., Huppert, H. E., et al. (1999). Mobility of pyroclastic flows and surges at the Soufrière Hills Volcano, Montserrat. *Geophys. Res. Lett.* 26, 537–540.
- Calder, Eliza & Sparks, R.S.J. & Gardeweg, M.. (2000). Erosion, transport and segregation of pumice and lithic clasts in pyroclastic flows inferred from ignimbrite at Lascar Volcano, Chile. *Journal of Volcanology and Geothermal Research*. 104. 201-235.
- Calder E, Wagner K, Ogburn SE. Volcanic hazard maps. In: Loughlin SC, Sparks S, Brown SK, Jenkins SF, Vye-Brown C,. (2015). eds. *Global Volcanic Hazards and Risk*. Cambridge: Cambridge University Press; 2015:335-342. doi:10.1017/CBO9781316276273.022
- Carazzo, G., Kaminski, E., & Tait, S. (2015). The timing and intensity of column collapse during explosive volcanic eruptions. *Earth and Planetary Science Letters*, 411, 208–217. doi:10.1016/j.epsl.2014.12.006
- Carey and Bursik (2000). Volcanic Plumes. En: Sigurdsson, H. (Ed.), *Encyclopedia of Volcanoes*. Academic Press, San Diego, pp. 527–544.
- Casertano, L. 1963. Investigaciones vulcanológicas efectuadas en Chile en el período 1959-1962. *Universidad de Chile, Boletín* 38: 67-72
- Cashman, Kathy & Scheu, Betty. (2015). Magmatic Fragmentation. 10.1016/B978-0-12-385938-9.00025-0.
- Castruccio, A., Clavero, J., Rivera, A. (2010). Comparative study of lahars generated by the 1961 and 1971 eruptions of Calbuco and Villarrica volcanoes, Southern Andes of Chile. *J. Volcanology and Geothermal Research*. 190: 297–311.
- Castruccio, Angelo & Clavero, Jorge. (2015). Lahar simulation at active volcanoes of the Southern Andes: implications for hazard assessment. *Natural Hazards*. 77. 10.1007/s11069-015-1617-x.
- Castruccio A, Clavero J, Segura A, Samaniego P, Roche O, Le Pennec J-L, Droguett B. (2016).

- Eruptive parameters and dynamics of the April 2015 sub-Plinian eruptions of Calbuco volcano (southern Chile). *Bulletin of Volcanology*. 78:62.
- Charbonnier, S. J., Connor, C. B., Connor, L. J., Sheridan, M. F., Oliva Hernández, J. P. & Richardson, J. A. (2018) Modeling the October 2005 lahars at Panabaj (Guatemala). *Bull Volcanol* 80, 4. <https://doi.org/10.1007/s00445-017-1169-x>
- Christen, M., Kowalski, J. & Bartelt, P. (2010) RAMMS: Numerical simulation of dense snow avalanches in three-dimensional terrain, *Cold Regions Science and Technology*, 63(1–2), 1-14. <https://doi.org/10.1016/j.coldregions.2010.04.005>.
- Chow, V.T. (1959). *Open-channel hydraulics*. McGraw-Hill.
- CHV Noticias (2015). Exclusivo sobrevuelo a volcán Calbuco reveló cambios en su estructura - CHV Noticias. Available from: <https://www.youtube.com/watch?v=sYAINEK2zXA> (Accessed 15/06/2021).
- Cioni R, Marianelli P, Santacroce R, Sbrana A (2002) Plinian and subPlinian eruptions. In Sigurdsson H et al (eds) *Encyclopedia of Volcanoes*, Academic Press, pp 477-494
- Clive, Mary Anne & Lindsay, Jan & Leonard, Graham. (2017). *More Than Meets the Eye: Volcanic Hazard Map Design and Visual Communication*. 10.1007/11157\_2016\_47.
- Cooperativa.cl (2015). La Erupción del Volcán Calbuco. Available from: <https://www.cooperativa.cl/noticias/pais/desastres-naturales/erupciones-volcanicas/la-erupcion-del-volcan-calbuco/2015-04-22/183646.html>. [Accessed 25 May 2021]
- Costa, J.E., 1988, Rheologic, geomorphic, and sedimentologic differentiation of water floods, hyperconcentrated flows, and debris flows, in Baker, V.R., Kochel, R.C., and Patten, P.C. (eds) *Flood Geomorphology*: Wiley-Intersciences, New York, p. 113-122
- DGA. Información Oficial Hidrometeorológica y de Calidad de Aguas en Línea. Available from: <https://snia.mop.gob.cl/BNAConsultas/reportes> (Accessed 21/06/2021).
- DGA. (2015). Inventario Nacional de Glaciares 2015. Dirección General de Aguas. <http://catalogo.geoportal.cl/geoportal/catalog/search/resource/resumen.page?uuid=%7B9C5CBF38-72D5-4489-A745-30AEAF1CDFC2%7D>. (March 25, 2019).
- Douillet, G.A., B. Taisne, E. Tsang-Hin-Sun, S.K. Müller, U. Kueppers, and D.B. Dingwell (2015). Syn-eruptive, soft-sediment deformation of deposits from dilute pyroclastic density current: triggers from granular shear, dynamic pore pressure, ballistic impacts and shock waves, *Solid Earth*, 6: 553–572.
- Dowling, C. A., & Santi, P. M. (2014). Debris flows and their toll on human life: a global analysis of debris-flow fatalities from 1950 to 2011. *Natural hazards*, 71(1), 203-227.

- Doyle, E. E., Cronin, S. J., Cole, S. E., & Thouret, J. C. (2010). The coalescence and organization of lahars at Semeru volcano, Indonesia. *Bulletin of volcanology*, 72(8), 961-970.
- Doyle, E. E., Cronin, S. J., & Thouret, J. C. (2011). Defining conditions for bulking and debulking in lahars. *Bulletin*, 123(7-8), 1234-1246
- Dufek, J. (2016). The Fluid Mechanics of Pyroclastic Density Currents. *Annu. Rev. Fluid Mech.* 48:459–85
- Endo, E.T., Murray, T. (1991). Real-time Seismic Amplitude Measurement (RSAM): a volcano monitoring and prediction tool. *Bulletin of Volcanology* 53: 533–545. <https://doi.org/10.1007/BF00298154>
- Espinoza, E. 1897. *Jeografía descriptiva de la República de Chile*. Imprenta Barcelona: 493 p. Santiago.
- Fagents, S., Gregg, T., & Lopes, R. (Eds.). (2013). *Modeling Volcanic Processes: The Physics and Mathematics of Volcanism*. Cambridge: Cambridge University Press. doi:10.1017/CBO9781139021562
- Folk RL, Ward WC (1957). A study in the significance of grain-size parameters, *Journal Sediment Petrology* 27:3–26.
- Forterre, Y., & Pouliquen, O. (2008). Flows of dense granular media. *Annual Review of Fluid Mechanics*, 40(1), 1-24.
- Francisco Molina (2018). Erupción volcán Calbuco. Available from: <https://www.youtube.com/watch?v=1rpk4Rr7eIU> (Accessed 21/04/2022)
- Frimberger, T., Andrade, S. D., Weber, S., & Krautblatter, M. (2021) Modelling future lahars controlled by different volcanic eruption scenarios at Cotopaxi (Ecuador) calibrated with the massively destructive 1877 lahar. *Earth Surf. Process. Landforms*, 46, 680– 700. <https://doi.org/10.1002/esp.5056>
- Gaunt, Elizabeth & Bernard, Benjamin & Hidalgo, Silvana & Proaño Altamirano, Antonio & Wright, Heather & Mothes, Patricia & Criollo, Evelyn & Kueppers, Ulrich. (2016). Juvenile magma recognition and eruptive dynamics inferred from the analysis of ash time series: The 2015 reawakening of Cotopaxi volcano. *Journal of Volcanology and Geothermal Research*. 328. 10.1016/j.jvolgeores.2016.10.013.
- George, D. L. & Iverson, R. M. (2014) A depth-averaged debris-flow model that includes the effects of evolving dilatancy. II. Numerical predictions and experimental tests. *Proc. R. Soc. A*. 470(2170). <http://doi.org/10.1098/rspa.2013.0820>
- Gladstone, Charlotte & McClelland, H. & Woodcock, Nigel & Pritchard, David & Hunt, James. (2017). The formation of convolute lamination in mud-rich turbidites. *Sedimentology*. 65. 10.1111/sed.12447.

- Google earth V 7.3.4.8248. (March 19, 2012). Calbuco Volcano, Chile. 41°19'58"S, 72°36'38"W, Eye alt: 3000 m. 2022 Maxar Technologies [Open March 31, 2022].
- Gomez, C., Lavigne, F. 2010. Transverse architecture of lahar terraces, inferred from radargrams: preliminary results from Semeru Volcano, Indonesia. *Earth Surf. Process. Landforms* 35, 1116-1121.
- Guioteca.com (2015), Erupción del volcán Calbuco: Las fotos más impresionantes. Available from: <https://www.guioteca.com/fotografia/erupcion-del-volcan-calbuco-las-fotos-mas-impresionantes/> (accessed 26/04/2022)
- Harpel, Christopher & De Silva, Sureetha & Salas, Grecia. (2011). The 2 ka Eruption of Misti Volcano, Southern Peru—The Most Recent Plinian Eruption of Arequipa's Iconic Volcano. *Special Paper of the Geological Society of America*. 484. 1-72. 10.1130/2011.2484.
- Hawkins, D. M. (2004) *Journal of Chemical Information and Computer Sciences*, 44 (1), 1-12. doi: 10.1021/ci0342472
- Hayes JL, Deligne NI, Bertin L, Calderon R, Wardman JB, Wilson TM, Leonard GS, Stewart C, Wallace KL, Baxter PJ. 2019. Impacts of the 2015 eruption of Calbuco volcano on Chilean infrastructure, utilities, agriculture, and health. Lower Hutt (NZ): GNS Science. 102 p. (GNS Science report; 2019/04). doi:10.21420/02YC-VX66.
- Hersch, R. (1993). The velocity-area method. *Flow Measurement and Instrumentation*, Volume 4, Issue 1. Pages 7-10, ISSN 0955-5986, [https://doi.org/10.1016/0955-5986\(93\)90004-3](https://doi.org/10.1016/0955-5986(93)90004-3).
- Hubbard, B., Sheridan, M., Carrasco, G., Díaz, R., Rodríguez, S., 2007. Comparative lahar hazard mapping at volcan Citlaltepétl, Mexico using SRTM, ASTER and DTED-1 digital topographic data. *Journal of Volcanology and Geothermal Research*. 160 (1-2): 99-124.
- Huggel, C., Kääb, A., Haeberli, W., Krummenacher, B. 2003. Regional- scale GIS-models for assessment of hazards from glacier lake outbursts: evaluation and application in the Swiss Alps. *Natural Hazards and Earth System Sciences* 3(6), p. 647-662
- Hungr, O., Jakob, M., (2005). *Debris flows hazards and related phenomena*. Praxis, Springer, pp. 728.
- Huss, M (2013). Density assumptions for converting geodetic glacier volume change to mass change, *The Cryosphere*, 7, 877–887, <https://doi.org/10.5194/tc-7-877-2013>.
- Iverson, R.M. (1997). The physics of debris flows. *Reviews of Geophysics* 35: 245-296.
- Iverson, R. M., Schilling, S. P., & Vallance, J. W. (1998) Objective delineation of lahar-inundation



- hazard zones. GSA Bulletin 110 (8): 972–984. doi: [https://doi.org/10.1130/0016-7606\(1998\)110<0972:ODOLIH>2.3.CO;2](https://doi.org/10.1130/0016-7606(1998)110<0972:ODOLIH>2.3.CO;2)
- Iverson, R.M., & Denlinger, R.P. 2001. Flow of variably fluidized granular masses across three-dimensional terrain: 1. Coulomb mixture theory. *Journal of Geophysical Research* 106 (B1): 537-552.
- Iverson, R.M. (2003). The debris-flow rheology myth. *International Conference on Debris-Flow Hazards Mitigation: Mechanics, Prediction, and Assessment, Proceedings*. 1.
- Iverson, R. M., Reid, M. E., Logan, M., LaHusen, R. G., Godt, J. W., & Griswold, J. P. (2011). Positive feedback and momentum growth during debris-flow entrainment of wet bed sediment. *Nature Geoscience*, 4(2), 116-121
- Iverson, R. M. & George, D. L. (2014) A depth-averaged debris-flow model that includes the effects of evolving dilatancy. I. Physical basis. *Proc. R. Soc. A*. 470(2170). <http://doi.org/10.1098/rspa.2013.0819>
- Jenkins, S., Phillips, J., Price, R., Feloy, K., Baxter, P., Hadmoko, D. S., Belizal, E. (2015). Developing building-damage scales for lahars: application to Merapi volcano, Indonesia. *Bulletin of Volcanology*. 77 (17p)
- Johnson, J. B., and J. L. Palma (2015). Lahar infrasound associated with Volcán Villarrica's 3 March 2015 eruption. *Geophysical Research Letters*, 42, 6324–6331, doi:10.1002/2015GL065024.
- Juan Francisco Veintimilla (2015). Primeros instantes erupción VOLCAN CALBUCO. Available from: <https://www.youtube.com/shorts/8YoXkLSJHzo> (Accesed 21/04/2022).
- Kavanagh, J. L., Engwell, S. L., & Martin, S. A. (2018) A review of laboratory and numerical modelling in volcanology, *Solid Earth*, 9, 531–571, <https://doi.org/10.5194/se-9-531-2018>
- Kennedy, M.C. & O'Hagan, A. (2001), Bayesian calibration of computer models. *Journal of the Royal Statistical Society: Series B (Statistical Methodology)*, 63: 425-464. <https://doi.org/10.1111/1467-9868.00294>
- Klohn, E., 1963. The February 1961, eruption of Calbuco Volcano. *Seismological Society of America Bulletin* 53, 1435–1436.
- Koyaguchi, T., & Suzuki, Y. J. (2018). The condition of eruption column collapse: Part 1. A reference model based on analytical solutions. *Journal of Geophysical Research: Solid Earth*. doi:10.1029/2017jb015308
- Laenen, A., Hansen R.P. (1988). Simulation Of Three Lahars In The Mount St. Helens Area, Washington Using A One-Dimensional, Unsteady-State Streamflow Model. U.S. Geological Survey Water-Resources Investigations Report 88-4004.

- Langham, J., Woodhouse, M. J., Hogg, A. J., & Phillips, J. C. (2021). Linear stability of shallow morphodynamic flows. *Journal of Fluid Mechanics*, 916.
- Lara, L., Orozco, G., Amigo, A., Silva, C. 2011. "Peligros Volcánicos de Chile" CARTA GEOLÓGICA DE CHILE, Serie Geología Ambiental No. 13. Escala 1:2.000.000, Servicio Nacional de Geología y Minería.
- Lavigne, Franck, Tirel, A., Floch, D., Veyrat-Charvillon, S. (2003). A real-time assessment of lahar dynamics and sediment load based on video-camera recording at Semeru volcano, Indonesia.
- León Cabello, Jorge (2015). Last Night Eruption - Volcan Calbuco (Puerto Varas - Chile). Available from: <https://www.flickr.com/photos/jorgeleoncabello/17252104271/in/album-72157627301995192/> . (Accessed 15/06/2021)
- López-Escobar, L.; Cembrano, J.; Moreno, H. (1995a). Geochemistry and tectonics of the Chilean Southern Andes basaltic Quaternary volcanism (37-46°S). *Revista Geológica de Chile* 22 (2): 219-234.
- López-Escobar, L., Parada, M.A., Hickey-Vargas, R., Frey, F.A., Kempton, P.D., Moreno, H., (1995b). Calbuco Volcano and minor eruptive center distributed along the Liquiñe Ofqui Fault Zone, Chile -41°–42°s-: contrasting origin of andesitic and basaltic magma in the Southern Volcanic Zone of the Andes. *Contrib. Mineral. Petrol.* 119, 345–361.
- Major, J.J. and Newhall, C.G., 1989. Snow and ice perturbation during historical volcanic eruptions and the formation of lahars and floods - a global review. *Bull. Volcanol.* 52: 1-27.
- Major, Jon & Pierson, Thomas & Hoblitt, Richard & Roa, Hugo. (2013). Pyroclastic density currents associated with the 2008-2009 eruption of Chaitén Volcano (Chile): Forest disturbances, deposits, and dynamics. *Andean Geology*. 40. 10.5027/andgeoV40n2-a09.
- Manville, V., K. Németh, K. Kano, (2009). Source to sink: A review of three decades of progress in the understanding of volcanoclastic processes, deposits, and hazards, *Sedimentary Geology*, Volume 220, Issues 3–4. Pages 136-161, ISSN 0037-0738, <https://doi.org/10.1016/j.sedgeo.2009.04.022>.
- Manville, V., Major, J., & Fagents, S. (2013) Modeling lahar behavior and hazards. In S. Fagents, T. Gregg, & R. Lopes (Eds.), *Modeling Volcanic Processes: The Physics and Mathematics of Volcanism* (pp. 300-330). Cambridge: Cambridge University Press. doi:10.1017/CBO9781139021562.014
- Martin, C., (1895). La erupción del volcán Calbuco. *Anales de la Universidad de Chile*, Imprenta Cervantes, Santiago, pp. 161–193.
- Matoza, R. S., Fee, D., Green, D. N., Le Pichon, A., Vergoz, J., Haney, M. M., et al. (2018). Local,

- regional, and remote seismo-acoustic observations of the April 2015 VEI 4 eruption of Calbuco volcano, Chile. *Journal of Geophysical Research: Solid Earth*, 123. <https://doi.org/10.1002/2017JB015182>.
- McClung DM (2001). Superelevation of flowing avalanches around curved channel bends. *J Geophys Res* 106:16,489–16,498
- McKay, M. D., Beckman, R. J., & Conover, W. J. (2000). A comparison of three methods for selecting values of input variables in the analysis of output from a computer code. *Technometrics*, 42(1), 55-61. DOI: 10.1080/00401706.2000.10485979
- Mella, Mauricio & Roa, Hugo & Vergés, Alejandro & Quiroz, David & Bertin, Lizette & Basualto, Daniel & Bertin, Daniel & Garrido, Natalia. (2015). Productos volcánicos e impactos asociados al ciclo eruptivo del 2015 del volcán Calbuco.
- Michaud-Dubuy, Audrey & Carazzo, Guillaume & Kaminski, E. & Girault, Frédéric. (2018). A revisit of the role of gas entrapment on the stability conditions of explosive volcanic columns. *Journal of Volcanology and Geothermal Research*. 357. 10.1016/j.jvolgeores.2018.05.005.
- Miranda, Bastian Ariel. 2019. Aplicación de un método de determinación y validación de altura de isoterma 0°C en el territorio chileno, a partir de datos de radiosonda en el período 1973-2017. Memoria para optar al título profesional de Geógrafo. Carrera Geografía, Facultad de Arquitectura y Urbanismo, Universidad de Chile. Santiago, Chile.
- Moreno, H., Naranjo, J.A., 2004. Calbuco volcano historic block-and-ash and pyroclastic flows: increasing threatening on surrounding communities, Southern Andes 41.5°S. IAVCEI General Assembly, Pucón, Chile, November 2004 vol. 4.
- Moreno, H.; Naranjo, J.A.; Clavero, J. 2006. Generación de lahares calientes en el volcán Calbuco, Andes del sur de Chile (41,3°S). In Congreso Geológico Chileno, No. 11, Actas: 512-513, Antofagasta.
- Morgado, Eduardo & Morgan, Daniel & Castruccio, Angelo & Ebmeier, Susanna & Parada, Miguel A & Brahm, Raimundo & Harvey, Jason & Gutierrez, Francisco & Walshaw, Richard. (2019). Old magma and a new, intrusive trigger: using diffusion chronometry to understand the rapid-onset Calbuco eruption, April 2015 (Southern Chile). *Contributions to Mineralogy and Petrology*. 174. 10.1007/s00410-019-1596-0.
- Muñoz-Salinas, E. & Manea, Vlad constantin & Castillo-Rodriguez, M. (2007). Estimation of lahar flow velocity on Popocatepetl volcano (Mexico). *Geomorphology*. 92. 91-99. 10.1016/j.geomorph.2007.02.011.
- Muñoz-Salinas E., Renschler C.S., Palacios D., 2009. A GIS-based method to determine the volumen of lahars: Popocatepetl volcano, Mexico. *Geomorphology* 111: 61-69

- Muñoz-Salinas, E., Castillo-Rodríguez, M., Manea, V., Manea, M., Palacios, D. (2009b). Lahar flow simulations using LAHARZ program: Application for the Popocatépetl volcano, Mexico. *Journal of Volcanology and Geothermal Research* 182: 13 – 22
- Muleta, M. K., & Nicklow, J. W. (2005). Sensitivity and uncertainty analysis coupled with automatic calibration for a distributed watershed model. *Journal of hydrology*, 306(1-4), 127-145. <https://doi.org/10.1016/j.jhydrol.2004.09.005>
- Navarro, M., Le Maître, O. P., Hoteit, I., George, D. L., Mandli K. T., & Knio, O. M. (2018) Surrogate-based parameter inference in debris flow model. *Comput Geosci* 22, 1447–1463. <https://doi.org/10.1007/s10596-018-9765-1>
- Newhall C, Self S (1982) The volcanic explosivity Index (VEI); An estimate of explosive magnitude for historical volcanism. *J Geophys Res* 87:1231–1238.
- Núñez, Gastón (2015) April 17th. Available at: <https://twitter.com/GastonunezNuez/status/589084793645719552> (Accessed 19/03/2022).
- O'Brien, J. S. (2007). FLO-2D User's Manual, (<https://documentation.flo-2d.com/>)
- Ogburn, S.E., Charlton, D., Norgaard, D. et al. The Volcanic Hazard Maps Database: an initiative of the IAVCEI Commission on Volcanic Hazards and Risk. *J Appl. Volcanol.* 12, 2 (2023). <https://doi.org/10.1186/s13617-022-00128-9>
- Ogie R.I., Clarke R.J., Forehead H., Perez P. (2019), Crowdsourced social media data for disaster management: Lessons from the PetaJakarta.org project. *Computers, Environment and Urban Systems*, v. 73, p. 108-117.
- Pacheco-Hoyos, Jaime & Aguirre-Díaz, Gerardo & Davila-Harris, Pablo. (2020). Elutriation pipes in ignimbrites: An analysis of concepts based on the Huichapan Ignimbrite, Mexico. *Journal of Volcanology and Geothermal Research*. 403. 107026. [10.1016/j.jvolgeores.2020.107026](https://doi.org/10.1016/j.jvolgeores.2020.107026).
- Paislobo Prensa (2015). Erupción volcán Calbuco : Camino a Las Cascadas. Available from: <https://www.youtube.com/watch?v=Ack2KNVrcgM> (Accessed 21/04/2022)
- Paredes, Gervoy (2015) April 24th. Available at: <https://twitter.com/GervoyAlcalde/status/591702832836927489> (Accessed 15/06/2021).
- Petit-Breuilh, M.E. (1999). Cronología eruptiva histórica de los volcanes Osorno y Calbuco, Andes del Sur (41°-41°30'S). *Servicio Nacional de Geología y Minería. Boletín* 53, 46 P. Santiago
- Pierson, T.C., 1980. Debris flows: An important process in high country gully erosion. *J. of the Tussok Grassland and Mountain Lands Institute (N.Z.)* 39, 3-14 Scott, K.M., 1988. Origins, behavior, and sedimentology of lahars and lahar-runout flows in the Toutle-

- Cowlitz river system. U.S. Geol. Surv. Prof. Paper 1447-A, 74 pp.
- Pierson, T.C., 1985, Initiation and flow behavior of the 1980 Pine Creek and Muddy River lahars, Mount St. Helens, Washington: Geological Society of America Bulletin, v.96, p.1056-1069.
- Pierson, T.C., 1986. Flow behavior of channelized debris flows, Mount St. Helens, Washington, pp. 269-296, in: Abrahams, A.D. (Ed.), Hillslope Processes, Allen and Unwin
- Pierson, T.C., and Scott, K.M., 1985, Downstream dilution of a lahar: transition from debris flow to hyperconcentrated streamflow: Water Resources Research, v.21, p.1511-1524.
- Pierson, Thomas & Costa, John. (1987). A rheologic classification of subaerial sediment-water flows. Debris flows/avalanches. 7. 10.1130/REG7-p1.
- Pierson. T.C., Janda. R.J., Thouret. J.C., and Borrero. C.A. 1990. Perturbation and melting of snow and ice by the 13 November 1985 eruption of Nevado del Ruiz, Colombia. and consequent mobilization. flow. and deposition of lahars. J. Volcanol. Geotherm. Res.. 41: 17-66.
- Pierson T.C., Janda R.J. 1994. Volcanic mixed avalanches: a distinct eruption-triggered mass-flow process at snow-clad volcanoes. Geological Society of America Bulletin 106: 1351-1358.
- Pierson, T.C., 1995, Flow characteristics of large eruption-triggered debris flows at snow-clad volcanoes: constraints for debris-flow models: Journal of Volcanology and Geothermal Research, v. 66, p. 283-294.
- Pierson T.C. 1998. An empirical method for estimating travel times for wet volcanic mass flows. Bulletin of Volcanology (60): 98-109.
- Pierson, T.C., 2005. Hyperconcentrated flow – transitional process between water flow and debris flow. Chapt. 8, pp. 159-208, in: Jakob, M., Hungr, O. (Eds.). Debris-flow hazards and related phenomena, Springer.
- Pierson T.C., Scott W.E., Vallance J.W., Pringle P.T. 2009. Eruption-related lahars and sedimentation response downstream of Mount Hood: Field guide to volcanoclastic deposits along the Sandy River, Oregon. The Geological Society of America Field Guide 15. 2009 (221-236).
- Pierson T.C., Pringle P.T., Cameron K.A. 2011. Magnitude and timing of downstream channel aggradation and degradation in response to a dome-building eruption at Mount Hood, Oregon. Geological Society of America Bulletin, January/February 2011 (3-20).
- Pierson, T. C., Major, J. J., Amigo, Á. & Moreno, H. (2013) Acute sedimentation response to rainfall following the explosive phase of the 2008–2009 eruption of Chaitén volcano, Chile. Bull Volcanol 75, 723. <https://doi.org/10.1007/s00445-013-0723-4>

- Pierson, T.C., and Major, J.J., 2014, Hydrogeomorphic effects of explosive volcanic eruption on drainage basins: *Annual Review of Earth and Planetary Sciences*, v. 42, p. 469–507
- Prata, F., Woodhouse, M., Huppert, H. E., Prata, A., Thordarson, T., and Carn, S.: Atmospheric processes affecting the separation of volcanic ash and SO<sub>2</sub> in volcanic eruptions: inferences from the May 2011 Grímsvötn eruption, *Atmos. Chem. Phys.*, 17, 10709–10732, <https://doi.org/10.5194/acp-17-10709-2017>, 2017.
- Prochaska, A.B., Santi, P.M., Higgins, J.D. et al. 2008. A study of methods to estimate debris flow velocity. *Landslides* 5, 431–444.
- Procter, J & Cronin, Shane & Fuller, Ian & Lube, Gert & Manville, V.. (2010). Quantifying the geomorphic impacts of a lake-breakout lahar, Mount Ruapehu, New Zealand. *Geology*. 38. 67-70. 10.1130/G30129.1.
- Riccardi, M.T. (2016), The power of crowdsourcing in disaster response operations. *International Journal of Disaster Risk Reduction*, v. 20, p. 123-128.
- Rahman, Md Aftabur & Konagai, Kazuo. (2017). A hands-on approach to estimate debris flow velocity for rational mitigation of debris hazard. *Canadian Geotechnical Journal*. 55. 10.1139/cgj-2017-0211.
- Raudkivi, A.J. (1998). *Loose Boundary Hydraulics* (1st ed.). CRC Press. <https://doi.org/10.1201/9781003077800>
- Rougier, J., Sparks, R. S. J., Cashman, K. V., & Brown, S. K. (2018) The global magnitude–frequency relationship for large explosive volcanic eruptions, *Earth and Planetary Science Letters*, 482, 621-629, <https://doi.org/10.1016/j.epsl.2017.11.015>.
- Romero JE, Morgavi D, Arzilli F, Daga R, Caselli A, Reckziegel F, Viramonte J, Díaz-Alvarado J, Polacci M, Burton M, Perugini D (2016) Eruption dynamics of the 22–23 April 2015 calbuco volcano (Southern Chile): Analyses of tephra fall deposits. *J Volcanol Geotherm*.
- Romero, Jorge & Alloway, Brent & Gutiérrez, Romina & Bertin, Daniel & Castruccio, Angelo & Villarosa, Gustavo & Schipper, C. & Guevara, Alicia & Bustillos, Jorge & Pisello, Alessandro & Daga, Romina & Montiel, Mauricio & Gleeman, Emma & González, Mauro & Morgavi, Daniele & Ribeiro Guevara, Sergio & Mella, Mauricio. (2021). Centennial-scale eruptive diversity at Volcán Calbuco (41.3°S; Northwest Patagonia) deduced from historic tephra cover-bed and dendrochronologic archives. *Journal of Volcanology and Geothermal Research*. 10.1016/j.jvolgeores.2021.107281.
- Sakamoto, Miki & Gomez, Christopher. (2019). Assessment of UAV-Based Photogrammetry in Lahar Valleys to Estimate Boulder Potential Hazards - Field Experiment at Unzen Volcano (Japan).
- Schuster, R. L., & Highland, L. (2001). Socioeconomic and environmental impacts of landslides



- in the western hemisphere (pp. 1-50). Denver (CO): US Department of the Interior, US Geological Survey.
- Scheidl, C., McArdell, Brian W., Rickenmann, D., 2015. Debris-flow velocities and superelevation in a curved laboratory channel. *Canadian Geotechnical Journal*, 2015, 52:305-317
- Scott, K.M., 1988. Origins, behavior, and sedimentology of lahars and lahar-runout flows in the Toutle-Cowlitz River system. U.S. Geol. Surv. Prof. Pap. 1447-A, 74 pp.
- Scott, K.M, Vallance, J.W., Pringle, P.T., 1995. Sedimentology, behavior, and hazards of debris flows at Mount Rainier, Washington. U.S. Geol. Surv. Prof. Paper 1547, 56 pp
- Shea, T., Gurioli, L., Houghton, B. F., Cioni, R., & Cashman, K. V. (2011). Column collapse and generation of pyroclastic density currents during the A.D. 79 eruption of Vesuvius: The role of pyroclast density. *Geology*, 39(7), 695–698. doi:10.1130/g32092.1
- Sellés, D. & Moreno, H., 2011. Geología del volcán Calbuco, Región de los Lagos. Servicio Nacional de Geología y Minería, Carta Geológica de Chile, Serie Geología Básica, No.XX, 30 p., 1 mapa escala 1:50.000, Santiago.
- SERNAGEOMIN, 2015a. Reporte de Actividad Volcánica (RAV) Región de los Lagos. Año 2015, Marzo – Volumen 3.
- SERNAGEOMIN, 2015b. Reporte Especial de Actividad Volcánica (REAV) Región de los Lagos. Año 2015 Abril 22 (17:30 HL)
- SERNAGEOMIN, 2015c. Reporte Especial de Actividad Volcánica (REAV) Región de los Lagos. Año 2015 Abril 22 (20:45 HL)
- SERNAGEOMIN, 2015d. Reporte de Actividad Volcánica (RAV) Región de los Lagos. 2015\_04\_25, Volumen 6.
- SERNAGEOMIN, 2015e. Reporte de Actividad Volcánica (RAV) Región de los Lagos. 2015\_04\_30, Volumen 11.
- SERNAGEOMIN, 2015f. Reporte de Actividad Volcánica (RAV) Región de los Lagos. 2015\_05\_28, Volumen 40.
- SERNAGEOMIN, 2015g. Reporte de Actividad Volcánica (RAV) Región de los Lagos. Junio 2015, Volumen 42.
- SERNAGEOMIN, 2015h. Reporte de Actividad Volcánica (RAV) Región de los Lagos. Julio 2015, Volumen 44.
- SERNAGEOMIN, 2015i. Reporte de Actividad Volcánica (RAV) Región de los Lagos. Agosto 2015, Volumen 46.
- Soulsby, R. (1997), Dynamics of marine sands, Thomas Telford Publishing, doi:

- 10.1680/doms.25844.
- Soychile.cl (2015). Aludes en el sector sur del Calbuco arrasaron con viviendas, una escuela, puentes y una piscicultura. Available from: <https://www.soychile.cl/Puerto-Montt/Sociedad/2015/04/25/318584/Aludes-en-el-sector-sur-del-Calbuco-arrasaron-con-viviendas-una-escuela-puentes-y-una-piscicultura.aspx> (Accessed 27/04/2022).
- Sparks, R. S. J., and L. Wilson (1976), A model for the formation of ignimbrite by gravitational column collapse, *J. Geol. Soc. London*, 132, 441–451.
- Sparks, R.S.J., Bursik, M.I., Carey, S.N., Gilbert, J.S., Glaze, L.S., Sigurdsson, H., Woods, A.W., 1997. *Volcanic Plumes*. John Wiley and Sons, New York (574 pp.).
- Spearman, J., & Manning, A. J. (2017). On the hindered settling of sand-mud suspensions. *Ocean Dynamics*, 67(3), 465-483.
- Stern CR. 2004. Active Andean volcanism: its geologic and tectonic setting. In: *Revista Geológica de Chile*, Vol. 31, No. 2, p. 161-206.
- Stevens, N., Manville, V., Heron, D. 2002. The sensitivity of a volcanic flow model to digital elevation model accuracy: experiements with digitised map contours and interferometric SAR at Ruapehu and Taranaki volcanoes, New Zealand. *Journal of Volcanology and Geothermal Research* 160 (1-2): 99-124.
- SUBTEL. Subsecretaría de Telecomunicaciones, Ministerio de Transportes y Telecomunicaciones (2016). Sector Telecomunicaciones Primer Trimestre 2016. Santiago, Chile. <https://goo.gl/qOOEbE>.
- Tavra, M., Racetin, I. & Peroš, J. (2021). The role of crowdsourcing and social media in crisis mapping: a case study of a wildfire reaching Croatian City of Split. *Geoenviron Disasters* 8, 10
- Thouret J.C. 1990. Effects of the november 13, 1985 eruption on the snow pack and ice cap of Nevado del Ruiz volcano, Colombia. *Journal of Volcanology and Geothermal Research* 41: 177-201.
- Thouret J.C., Ramirez J., Gibert-Malengreau B., Vargas C.A., Naranjo J.L., Vandemeulebrouck J., Valla F., Funk M. 2007. Volcano–glacier interactions on composite cones and lahar generation: Nevado del Ruiz, Colombia, case study. *Annals of Glaciology* 45: 115-127.
- Thouret, J. C., Antoine, S., Magill, C., & Ollier, C. (2020). Lahars and debris flows: Characteristics and impacts. *Earth-Science Reviews*, 201, 103003
- Tierz, P., Woodhouse, M. J., Phillips, J. C., Sandri, L., Selva, J., Marzocchi, W., & Odbert, H. M. (2017). A framework for probabilistic multi-hazard assessment of rain-triggered lahars using Bayesian belief networks. *Frontiers in Earth Science*, 5, 73.

- Toledo, Luis (2015). Aludes en el sector sur del Calbuco arrasaron con viviendas, una escuela, puentes y una piscicultura. *El Llanquihue* [online]. Available from: <https://www.soychile.cl/Puerto-Montt/Sociedad/2015/04/25/318584/Aludes-en-el-sector-sur-del-Calbuco-arrasaron-con-viviendas-una-escuela-puentes-y-una-piscicultura.aspx> [Accessed 25 May 2021].
- Trinh, T., Boltenhagen, P., Delannay, R., & Valance, A. (2017). Erosion and deposition processes in surface granular flows. *Physical Review E*, 96(4), 042904.
- UNISDR (2015). The human cost of natural disasters: A global perspective.
- Vallance, J., 2000. Lahars. En: Sigurdsson, H. (Ed.), *Encyclopedia of Volcanoes*. Academic Press, San Diego, pp. 601–616.
- Vallance, J. W., & Iverson, R. M. (2015). Lahars and their deposits. In *The encyclopedia of volcanoes* (pp. 649-664). Academic Press
- Valderrama Cayuman, Oscar & Cardona, Carlos & Gil-Cruz, Fernando. (2016). Subplinian eruption of Calbuco volcano (Chile), April 22th, an example of VEI-4 explosive eruption with few precursor signals.
- Van Eaton, A.R., Amigo, A., Bertin, D., Mastin, L.G., Giacosa, R.E., González, J., Valderrama, O., Fontijn, K., Behnke, S.A., (2016). Volcanic lightning and plume behavior reveal evolving hazards during the April 2015 eruption of Calbuco volcano, Chile. *Geophys. Res. Lett.* 43 (7), 3563–3571.
- Vázquez, Rosario & Capra, Lucia & Caballero, Lizeth & Arámbula, Raúl & Reyes-Dávila, G.. (2013). The Anatomy of a lahar: Deciphering the 15th September 2012 lahar at Volcán de Colima, Mexico. *Journal of Volcanology and Geothermal Research*. 272. 10.1016/j.jvolgeores.2013.11.013.
- Vernon I, Goldstein M, Bower RG. Galaxy formation: a bayesian uncertainty analysis. *Bayesian Anal.* 2010; 5(4):619–70.
- Viana, F. A. (2016). A tutorial on Latin hypercube design of experiments. *Quality and reliability engineering international*, 32(5), 1975-1985. <https://doi.org/10.1002/qre.1924>
- Voellmy, A. (1955). Über die Zerstörungskraft von Lawinen. *Schweizerische Bauzeitung*, Jahrg., 73, 159-162.
- Walder J.S. 2000.a. Pyroclast/snow interactions and thermally driven slurry formation. Part 1: Theory for monodisperse grain beds. *Bulletin of Volcanology* 62: 105-118.
- Walder J.S. 2000.b. Pyroclast/snow interactions and thermally driven slurry formation. Part 2: Experiments and theoretical extension to polydisperse tephra. *Bulletin of Volcanology* 62: 119-129.

- Wallace, K., Snedigar, S. & Cameron, C. (2015). 'Is Ash Falling?', an online ashfall reporting tool in support of improved ashfall warnings and investigations of ashfall processes. *J Appl. Volcanol.* 4, 8.
- Watt, S.F.L., Pyle, D.M., Naranjo, J.A., Rosqvist, G., Mella, M., Mather, T.A., Moreno, H., 2011. Holocene tephrochronology of the hualaihue region (Andean southern volcanic zone, ~42° S), Southern Chile. *Quat. Int.* 246, 324–343.
- Waythomas, Chris & Pierson, Thomas & Major, Jon & Scott, William. (2013). Voluminous ice-rich and water-rich lahars generated during the 2009 eruption of Redoubt Volcano, Alaska. *Journal of Volcanology and Geothermal Research.* 259. 10.1016/j.jvolgeores.2012.05.012.
- Williams, R. (2012) DEMs of difference. *Geomorphological Techniques*, 2(3.2),
- Wilson, L., Sparks, R. S. J., & Walker, G. P. L. (1980). Explosive volcanic eruptions -- IV. The control of magma properties and conduit geometry on eruption column behaviour. *Geophysical Journal International*, 63(1), 117–148. doi:10.1111/j.1365-246x.1980.tb02613.x
- Wilson, C.J.N.; Houghton, B.F. 1999. Pyroclastic transport and deposition in Sigurdsson, H.; Houghton, B.F.; McNutt, S.; Rhymer, H.; Stix, J. (eds) *Encyclopaedia of Volcanoes*, 545-554. Academic Press, San Diego.
- Wilson, Grant & Wilson, Tom & Deligne, Natalia & Blake, Daniel & Cole, Jim. (2017). Framework for developing volcanic fragility and vulnerability functions for critical infrastructure. *Journal of Applied Volcanology*. 6. 10.1186/s13617-017-0065-6.
- Woodhouse, M. J., Langham, J., Hogg, A. J., & Phillips, J. C. (In preparation) A shallow-layer model for lahars: formulation and phenomenology. (Non-peer reviewed draft available at [www.laharflow.bris.ac.uk/paper/draft.pdf](http://www.laharflow.bris.ac.uk/paper/draft.pdf))
- Woodhouse, M. J., Hogg, A. J., Phillips, J. C., & Rougier, J. C. (2015) Uncertainty analysis of a model of wind-blown volcanic plumes. *Bull Volcanol* 77, 83. <https://doi.org/10.1007/s00445-015-0959-2>
- Woodhouse, M. J., Johnson, C. G., Hogg, A. J., Phillips, J. C., Espín Bedón, P. A., Almeida, S., & Andrade, D. (2016). LaharFlow: a web-based lahar hazard model. *Cities on Volcanoes*, 9.
- Woods, A.W. The fluid dynamics and thermodynamics of eruption columns. *Bull Volcanol* 50, 169–193 (1988). <https://doi.org/10.1007/BF01079681>
- Worni R, Huggel C, Stoffel M, Pulgarín B (2012) Challenges of modeling current very large lahars at Nevado del Huila Volcano, Colombia. *Bull Volcanol* 74(2):309–324

## 6 Supplementary material

### 6.1 Grain-Size

Table 6. Grain size table. Columns are the dry weight for different size fraction.

Sample	East 18G	North 18G	>32mm	32mm-16mm	16mm-8mm	8mm-4mm	4mm-2mm	2mm-1mm
FV110120-7C	697659	5418930	2630.83	660.16	472.37	322.78	275.50	258.12
FV110120-9A	697085	5418636	42.72	87.64	95.07	114.14	93.66	86.04
FV120120-2A	702754	5415177	554.73	1013.39	696.41	606.65	434.15	319.90
FV120120-2B	702754	5415177	367.86	385.19	405.09	259.12	160.27	110.64
FV120120-3	701690	5418432	409.22	402.01	486.76	528.92	323.22	214.92
FV120120-5	701765	5417041	311.14	217.03	370.49	682.33	692.43	539.30
FV130120-1A	702594	5417036	568.76	92.15	318.28	407.49	318.22	245.27
FV130120-1B	702594	5417036	1139.67	469.31	238.04	119.30	101.74	77.58
FV150120-6	697565	5414156	41.46	57.72	275.68	350.64	268.67	180.14
FF310316-2	702838	5416205	984.58	375.11	252.89	286.73	300.67	343.39
FF010416-2	702749	5415415	920.77	666.40	704.93	477.91	285.06	221.25
FF310316-1A	702656	5416732	1706.34	516.38	500.89	393.01	310.65	225.83
FF010416-1B	702124	5416419	1131.14	908.96	539.82	368.87	260.10	163.02
FF020416-2	696958	5417042	1632.94	819.23	563.85	426.91	331.71	255.05
FF020416-1	696933	5418021	491.97	619.78	523.58	442.87	328.21	235.77
FF030416-1	703111	5413004	1561.22	802.12	619.47	403.84	210.10	137.32
FF040416-1	697004	5416012	1051.35	722.75	608.30	385.43	264.02	206.79
FF040416-3	704587	5411644	0.00	29.16	31.39	87.88	156.86	196.91
FF010416-3A	702584	5414317	0.00	15.24	76.41	120.36	124.38	135.44
FF030416-2B	704421	5413042	0.00	0.00	40.07	69.99	119.23	144.81

FF040416-2	705065	5412301	0.00	43.54	190.90	162.61	124.24	102.60
FF050416-1	697733	5414789	163.94	587.84	600.48	467.35	336.64	263.31
FF050416-2	700815	5411108	0.00	0.00	1.57	21.86	50.15	94.28
FF050416-3	699878	5412185	0.00	0.00	0.00	10.43	47.49	76.47
FV100120-6A	699383	5412685	801.04	215.85	354.42	504.63	449.19	357.43
FV100120-6B	699383	5412685	47.09	153.69	159.33	129.22	114.21	79.33
FV100120-6C	699432	5412772	0.00	32.42	102.41	156.92	165.03	142.68
FV100120-6D	699432	5412772	0.00	13.24	90.04	156.44	157.07	122.69
FV110120-6A	697662	5419022	986.11	538.87	487.99	375.65	311.13	298.86
FV110120-7A	697659	5418930	297.33	210.49	195.24	128.22	94.28	76.84
FV110120-7B	697659	5418930	97.09	106.83	222.53	133.55	81.26	61.63
FV110120-7D	697659	5418930	333.76	158.63	141.47	84.71	62.79	46.56
FV110120-8	697185	5418698	0.00	20.14	110.06	71.98	63.96	61.84
FV120120-1	702601	5415223	0.00	10.94	203.40	508.37	537.10	456.77
FV150120-7A	697578	5414391	39.47	275.06	388.92	279.11	188.45	150.65

Table 7. Continuation of Table 6 (to the right)

Sample	East 18G	North 18G	1mm- 0.5mm	0.5mm- 0.25mm	0.25mm- 0.125mm	0.125mm- 0.063mm	<0.063mm	Valley	Facie
FV110120-7C	697659	5418930	274.79	386.19	346.11	170.08	216.25	Rio Blanco	Source
FV110120-9A	697085	5418636	86.02	109.78	79.84	33.24	28.73	Rio Blanco	Source
FV120120-2A	702754	5415177	250.09	263.96	204.92	88.50	95.74	Río Este	Medial
FV120120-2B	702754	5415177	84.79	94.00	89.66	54.90	71.57	Río Este	Medial
FV120120-3	701690	5418432	166.16	206.58	189.85	87.68	109.11	Río Este	Proximal
FV120120-5	701765	5417041	436.41	534.35	349.04	141.31	115.45	Río Este	Proximal
FV130120-1A	702594	5417036	193.39	226.22	121.67	40.61	41.70	Río Este	Proximal
FV130120-1B	702594	5417036	71.25	92.35	90.40	56.97	94.22	Río Este	Proximal



FV150120-6	697565	5414156	134.76	142.51	114.45	71.80	86.33	Río Blanco	Overflow
FF310316-2	702838	5416205	434.38	457.77	213.65	49.06	32.42	Río Este	Proximal
FF010416-2	702749	5415415	159.53	246.28	222.81	111.00	151.29	Río Este	Medial
FF310316-1A	702656	5416732	167.52	171.67	141.84	65.18	69.18	Río Este	Proximal
FF010416-1B	702124	5416419	114.64	139.29	130.42	66.53	72.79	Río Este	Proximal
FF020416-2	696958	5417042	212.14	245.68	215.08	129.18	200.94	Río Blanco	Proximal
FF020416-1	696933	5418021	194.96	217.21	170.19	82.42	128.08	Río Blanco	Source
FF030416-1	703111	5413004	163.33	250.70	159.51	34.39	14.78	Río Este	Distal
FF040416-1	697004	5416012	186.29	226.51	191.24	105.26	150.66	Río Blanco	Proximal
FF040416-3	704587	5411644	207.19	177.91	69.49	9.78	0.96	Río Este	Distal
FF010416-3A	702584	5414317	134.75	159.22	125.26	68.84	87.40	Río Este	Lateral
FF030416-2B	704421	5413042	135.84	134.72	107.32	63.49	79.82	Río Este	Distal
FF040416-2	705065	5412301	99.49	124.04	119.17	69.33	83.19	Río Este	Distal
FF050416-1	697733	5414789	235.61	326.45	279.01	156.91	255.36	Río Blanco	Medial
FF050416-2	700815	5411108	76.25	62.38	44.43	25.06	35.05	Río Blanco	Distal
FF050416-3	699878	5412185	62.24	55.69	39.05	21.94	30.5	Río Blanco	Distal
FV100120-6A	699383	5412685	303.58	340.21	304.06	167.87	242.84	Río Blanco	Distal
FV100120-6B	699383	5412685	59.45	65.58	58.01	35.01	55.35	Río Blanco	Distal
FV100120-6C	699432	5412772	128.59	152.65	124.44	82.02	122.74	Río Blanco	Distal
FV100120-6D	699432	5412772	80.14	75.01	65.27	37.01	63.00	Río Blanco	Distal
FV110120-6A	697662	5419022	350.00	514.02	462.40	274.61	307.94	Río Blanco	PDC
FV110120-7A	697659	5418930	72.92	96.69	93.39	67.56	74.66	Río Blanco	Source
FV110120-7B	697659	5418930	57.21	64.30	69.54	34.34	74.24	Río Blanco	Source
FV110120-7D	697659	5418930	43.71	61.02	66.23	44.04	63.60	Río Blanco	Source
FV110120-8	697185	5418698	72.43	108.63	111.59	58.41	59.37	Río Blanco	PDC
FV120120-1	702601	5415223	380.76	445.81	364.94	184.97	249.90	Río Este	Lateral
FV150120-7A	697578	5414391	131.30	154.47	145.66	86.61	130.58	Río Blanco	Medial